NUMERICALLY EFFICIENT ANALYSIS AND DESIGN OF CONFORMAL PRINTED STRUCTURES IN CYLINDRICALLY LAYERED MEDIA

A THESIS SUBMITTED TO
THE GRADUATE SCHOOL OF NATURAL AND APPLIED SCIENCES
OF
MIDDLE EAST TECHNICAL UNIVERSITY

BY

R. CÜNEYT ACAR

IN PARTIAL FULFILLMENT OF THE REQUIREMENTS
FOR
THE DEGREE OF DOCTOR OF PHILOSOPHY
IN
ELECTRICAL AND ELECTRONICS ENGINEERING

SEPTEMBER 2007

Approval of Thesis

NUMERICALLY EFFICIENT ANALYSIS AND DESIGN OF CONFORMAL PRINTED STRUCTURES IN CYLINDRICALLY LAYERED MEDIA

submitted by **R. CÜNEYT ACAR** in partial fulfillment of the requirements for the degree of **Doctor of Philosophy in Electrical and Electronics Engineering Department, Middle East Technical University** by,

Prof. Dr. Canan Özgen
Dean, **Graduate School of Natural and Applied Sciences** _____

Prof. Dr. İsmet Erkmen
Head of Department, **Elec. and Electronics Eng. Dept., METU** _____

Prof. Dr. Gülbin Dural
Supervisor, **Elec. and Electronics Eng. Dept., METU** _____

Examining Committee Members:

Prof. Dr. Mustafa Kuzuoğlu _____
Electrical and Electronics Eng. Dept.,METU

Prof. Dr. Gülbin Dural _____
Electrical and Electronics Eng. Dept.,METU

Prof. Dr. Adnan Köksal _____
Electrical and Electronics Eng. Dept.,HU

Assoc. Prof. Dr. Özlem Aydın Çivi _____
Electrical and Electronics Eng. Dept.,METU

Prof. Dr. Gönül Turhan Sayan _____
Electrical and Electronics Eng. Dept.,METU

Date: _____

I hereby declare that all information in this document has been obtained and presented in accordance with academic rules and ethical conduct. I also declare that, as required by these rules and conduct, I have fully cited and referenced all materials and results that are not original to this work.

Name, Last Name:

Signature:

ABSTRACT

NUMERICALLY EFFICIENT ANALYSIS AND DESIGN OF CONFORMAL PRINTED STRUCTURES IN CYLINDRICALLY LAYERED MEDIA

Acar, Remzi Cüneyt
Ph.D., Department of Electrical and Electronics Engineering
Supervisor: Prof. Dr. Gülbin Dural

September 2007, 105 pages

The complete set of Green's functions for cylindrically layered media is presented. The formulations reported in the previously published work by Tokgöz (M.S.Thesis, 1997) are recalculated, the missing components are added and a solution to the problem when $\rho = \rho'$ is proposed.

A hybrid method to calculate mutual coupling of electric or magnetic current elements on a cylindrically layered structure using MoM is proposed. For the calculation of MoM matrix entries, when $\rho = \rho'$, and ϕ is not close to ϕ', the closed-form Green's functions are employed. When ϕ is close to ϕ', since the spectral-domain Green's functions do not converge, MoM matrix elements are calculated in the spectral domain. The technique is applied to both printed dipoles and slots placed on a layered cylindrical structure. The computational efficiency of the anaysis of mutual coupling of printed elements on a

cylindrically layered structure is increased with the use of proposed hybrid method due to use of closed-form Green's functions.

Keywords: Green's function, closed-form Green's function, cylindrically layered medium, conformal antennas, MoM, mutual coupling.

ÖZ

SİLİNDİRİK KATMANLI ORTAMDA YERLEŞTİRİLMİŞ DÜZ OLMAYAN BASKI DEVRE ELEMANLARININ ETKİN NUMERİK ANALİZİ VE TASARIMI

Acar, Remzi Cüneyt
Doktora, Elektrik ve Elektronik Mühendisliği Bölümü
Tez Yöneticisi: Prof. Dr. Gülbin Dural

Eylül 2007, 105 sayfa

Silindirik katmanlı ortamdaki Green fonksiyonları tamamlanmıştır. Tokgöz tarafından verilmiş olan Green fonksiyonları (Yüksek Lisans Tezi, 1997) tekrar hesaplanmış, eksik olan Green fonksiyonları eklenmiş ve $\rho = \rho'$ problemi çözülmüştür.

Moment Metod kullanılarak silindirik katmanlı ortamdaki elektrik ve manyetik akım elemanlarının karşılıklı etkileşimin hesaplanması için hibrid metod sunulmuştur. Moment Metod matris elemanlarının hesaplanması için $\rho = \rho'$ koşulunda, ϕ ile ϕ' birbirlerinden uzak iken, kapalı-formdaki Green fonksiyonları kullanılmış, ϕ ile ϕ' birbirlerine yakın iken, spektral uzaydaki Green fonksiyonları yakınsamadığından Moment Metod matris elemanları spektral uzayda hesaplanmıştır. Bu teknik, çok katmanlı silindirik yapıların üzerine yerleştirilmiş dipol ve yarıklara uygulanabilir. Çok katmanlı silindirik yapılardaki baskı devre elemanlarının karşılıklı iletişim analizi hesaplama

verimliliği, kapalı- form Green fonksiyonları yardımıyla önerilen hibrid metod kullanımı sayesinde artırılmıştır.

Anahtar kelimeler: Green fonksiyonu, kapalı-form Green fonksiyonu, silindirik katmanlı ortam, düz olmayan antenler, Moment Metod, karşılıklı etkileşim.

To my parents

ACKNOWLEDGMENTS

I would like to express my sincere gratitude to my thesis advisor Prof. Dr. Gülbin Dural for her guidance, support and encouragement throughout the study of this thesis. It was a privilege for me to have an outstanding research experience under her supervision.

It is a distinction for me to acknowledge Prof. Dr. Adnan Köksal and Assoc. Prof. Dr. Özlem Aydın for sharing their experience and technical facilities with me, lighting the way for the concept of this research and their invaluable suggestions and contributions. Many thanks are owed to Vakur B. Ertürk for his help for eigenfunction solution code.

I am grateful to ASELSAN Electronics Industries for not only giving me the opportunity to improve my engineering capabilities but also providing me every kind of software, hardware and financial support throughout the progress of this work. It is also my pleasure to express my appreciation to my colleagues who always supported me spiritually and provided me a nice, friendly office atmosphere.

Finally, I would like to deeply appreciate my parents and my brother for their endless love, support, encouragement and patience. This thesis would have been impossible without their guidance.

TABLE OF CONTENTS

PLAGIARISM.....iii

ABSTRACT.....iv

ÖZ.....vi

ACKNOWLEDGMENTS.....ix

TABLE OF CONTENTS.....x

LIST OF FIGURES.....xiii

CHAPTER

I INTRODUCTION.....1

II SPECTRAL DOMAIN GREEN'S FUNCTIONS IN CYLINDRICALLY LAYERED MEDIA.....6

II.1 Introduction.....6

II.2 Field Expressions for Cylindrically Multilayered Media.....6

II.3 Spectral domain Green's Functions.....11

III CLOSED-FORM GREEN'S FUNCTIONS IN CYLINDRICALLY LAYERED MEDIA.....17

III.1 Introduction.....17

III.2 Spatial domain Green's Functions in Closed-form.....17

III.3 Closed-form Green's Functions when $\rho = \rho'$.....22

III.4 Numerical Results 25

III.4.1 Closed-form Green's Function Results for $\bar{\rho} \neq \bar{\rho}'$ 25

III.4.2 Closed-form Green's Function Results for $\rho = \rho'$.....36

IV SURFACE WAVE CONTRIBUTION.....45

IV.1 Introduction 45

IV.2 Surface Wave Poles 47

IV.3 Finding the Location of Surface Wave Poles 47

IV.4 Numerical Results.....50

V MUTUAL COUPLING BETWEEN ELECTRIC/MAGNETIC CURRENTELEMENTS.....59

V.1 The Method of Moments (MoM) 59

V.2 Mutual Coupling Between Two Narrow Strips.....60

V.3 Mutual Coupling Between Two Narrow Slots.....65

V.4 Mutual Impedance and Coupling Coefficient of Two Current Elements.....69

V.5 Numerical Results.....71

V.5.1 Mutual Coupling Between Two Narrow Strips.....71

V.5.2 Mutual Coupling Between Two Narrow Slots.....76

VI CONCLUSION.....81

BIBLIOGRAPHY.....84

APPENDIX

A GENERALIZED PENCIL OF FUNCTION METHOD.....90

B SPECTRAL-DOMAIN GREEN'S FUNCTION

COMPONENTS.....92

C ROOFTOP CURRENT MODES.....96

D NEWTON-RAPHSON METHOD.....103

CURRICULUM VITAE.....105

LIST OF FIGURES

Figure **Page**

II.1 General cylindrically multilayered medium.....7

II.2 Dispersion of waves through general multiple interface geometry.....8

III.1 Deformed Path.....18

III.2 Region 0: PEC, Region 1: $\varepsilon_{r_1} = 2.3$, $\mu_{r_1} = 1$, Region 2: free space, a_0=20mm, a_1= 21mm, ρ' = 21mm, ϕ'=0°, ρ = 40mm, ϕ =30°, f = 4.7 GHz.....25

III.3 $\log_{10}\left|G_{zz}^{E}\right|$ for an electric dipole pointing in z direction, for the geometry shown in Figure III.2 (N_1=4, N_2=5, N_3=1, T_1=0.1, T_2=4.5, T_3=5)......27

III.4 $\log_{10}\left|\int G_{\phi z}^{E} dz\right|$ for an electric dipole pointing in z direction, for the geometry shown in Figure III.2 (N_1=5, N_2=5, N_3=1, T_1=0.1, T_2=3.5, T_3=4).....28

III.5 $\log_{10}\left|G_{z\phi}^{H}\right|$ for an electric dipole pointing in ϕ direction, for the geometry shown in Figure III.2 (N_1=5, N_2=5, N_3=1, T_1=0.1, T_2=3.5, T_3=4).....28

III.6 $\log_{10}\left|\int G_{\phi\phi}^{H} dz\right|$ for an electric dipole pointing in ϕ direction, for the geometry shown in Figure III.2 (N_1=4, N_2=4, N_3=1, T_1=0.1, T_2=3, T_3=3.5).....29

III.7 $\log_{10}\left|G_{\rho z}^{E}\right|$ for an electric dipole pointing in z direction, for the geometry shown in Figure III.2 (N_1=4, N_2=4, N_3=1, T_1=0.1, T_2=3, T_3=3.5).....29

III.8 $\log_{10}\left|G_{\rho z}^{E}\right|$ for a magnetic dipole pointing in z direction, for the geometry shown in Figure III.2 (N_1=4, N_2=4, N_3=1, T_1=0.1, T_2=3, T_3=3.5).....30

III.9 $\log_{10}\left|\int G^{H}_{\rho\phi}dz\right|$ for an electric dipole pointing in ϕ direction, for the geometry shown in Figure III.2 (N_1=4, N_2=4, N_3=1, T_1=0.1, T_2=3, T_3=3.5).....30

III.10 $\log_{10}\left|\int G^{E}_{\rho\phi}dz\right|$ for a magnetic dipole pointing in ϕ direction, for the geometry shown in Figure III.2 (N_1=4, N_2=4, N_3=1, T_1=0.1, T_2=3, T_3=3.5).....31

III.11 $\log_{10}\left|\int G^{E}_{z\rho}dz\right|$ for an electric dipole pointing in ρ direction, for the geometry shown in Figure III.2 (N_1=5, N_2=4, N_3=1, T_1=0.1, T_2=3, T_3=3.5).....31

III.12 $\log_{10}\left|\int G^{H}_{\phi\rho}dz\right|$ for an electric dipole pointing in ρ direction, for the geometry shown in Figure III.2 (N_1=5, N_2=4, N_3=1, T_1=0.1, T_2=3, T_3=3.5).....32

III.13 $\log_{10}\left|G^{E}_{\rho\rho}\right|$ for an electric dipole pointing in ρ direction, for the geometry shown in Figure III.2 (N_1=5, N_2=4, N_3=1, T_1=0.1, T_2=3, T_3=3.5).....32

III.14 $\log_{10}\left|G^{E}_{z\rho}\right|$ for a magnetic dipole pointing in ρ direction, for the geometry shown in Figure III.2 (N_1=5, N_2=4, N_3=1, T_1=0.1, T_2=3, T_3=3.5).....33

III.15 $\log_{10}\left|G^{H}_{\phi\rho}\right|$ for a magnetic dipole pointing in ρ direction, for the geometry shown in Figure III.2 (N_1=5, N_2=4, N_3=1, T_1=0.1, T_2=3, T_3=3.5).....33

III.16 $\log_{10}\left|\int G^{E}_{\rho\rho}dz\right|$ for a magnetic dipole pointing in ρ direction, for the geometry shown in Figure III.2 (N_1=5, N_2=4, N_3=1, T_1=0.1, T_2=3, T_3=3.5).....34

III.17 $\log_{10}\left|G^{E}_{zz}\right|$ for an electric dipole pointing in z direction, for the geometry shown in Figure III.2 (N_1=4, N_2=5, N_3=1, T_1=0.1, T_2=4.5, T_3=5) when the dielectric is lossy $\varepsilon_{r_1} = 2.3 - j\,0.1$.....34

III.18 $\log_{10}\left|\int G^{E}_{\phi z}dz\right|$ for an electric dipole pointing in z direction, for the geometry shown in Figure III.2 (N_1=5, N_2=5, N_3=1, T_1=0.1, T_2=3.5, T_3=4) when the dielectric is lossy $\varepsilon_{r_1} = 2.3 - j\,0.1$.....35

III.19 $\log_{10}\left|G_{z\phi}^{H}\right|$ for an electric dipole pointing in ϕ direction, for the geometry shown in Figure III.2 (N_1=5, N_2=5, N_3=1, T_1=0.1, T_2=3.5, T_3=4) when the dielectric is lossy $\varepsilon_{r_1} = 2.3 - j\,0.1$ 35

III.20 $\log_{10}\left|\int G_{\phi\phi}^{H} dz\right|$ for an electric dipole pointing in ϕ direction, for the geometry shown in Figure III.2 (N_1=4, N_2=4, N_3=1, T_1=0.1, T_2=3, T_3=3.5) when the dielectric is lossy $\varepsilon_{r_1} = 2.3 - j\,0.1$ 36

III.21 $\log_{10}\left|G_{zz}^{E}\right|$ for an electric dipole pointing in z direction, for the geometry shown in Figure III.2, ρ = ρ'=21mm, $\phi - \phi' = 60°$ 37

III.22 $\log_{10}\left|G_{zz}^{E}\right|$ for an electric dipole pointing in z direction, for the geometry shown in Figure III.2, ρ = ρ'=21mm, $\phi - \phi' = 50°$ 37

III.23 $\log_{10}\left|G_{zz}^{E}\right|$ for an electric dipole pointing in z direction, for the geometry shown in Figure III.2, ρ = ρ'=21mm, $\phi - \phi' = 40°$ 38

III.24 $\log_{10}\left|G_{zz}^{E}\right|$ for an electric dipole pointing in z direction, for the geometry shown in Figure III.2, ρ = ρ'=21mm, $\phi - \phi' = 30°$ 39

III.25 $\log_{10}\left|G_{zz}^{E}\right|$ for an electric dipole pointing in z direction, for the geometry shown in Figure III.2, ρ = ρ'=21mm, $\phi - \phi' = 20°$ 39

III.26 $\log_{10}\left|G_{zz}^{E}\right|$ for an electric dipole pointing in z direction, for the geometry shown in Figure III.2, ρ = ρ'=21mm, $\phi - \phi' = 15°$ 40

III.27 $\log_{10}\left|G_{zz}^{E}\right|$ for an electric dipole pointing in z direction, for the geometry shown in Figure III.2, ρ = ρ'=21mm, $\phi - \phi' = 10°$ 40

III.28 $\log_{10}\left|\int G_{z\rho}^{E} dz\right|$ for an electric dipole pointing in ρ direction, for the geometry shown in Figure III.2, ρ = ρ'=21mm, $\phi - \phi' = 15°$, ε_{r_1}=2.3, f=10GHz 41

III.29 $\log_{10}\left|\int G_{z\rho}^{H} dz\right|$ for a magnetic dipole pointing in ρ direction, for the geometry shown in Figure III.2, ρ = ρ'=21mm, $\phi - \phi' = 15°$, ε_{r_1}=2.3, f=10GHz 42

III.30 $\log_{10}\left|G_{z\rho}^{E}\right|$ for a magnetic dipole pointing in ρ direction, for the geometry shown in Figure III.2, ρ = ρ'=21mm, $\phi-\phi'=10°$, $\varepsilon_{r_1}=5$, f=10GHz.....42

III.31 $\log_{10}\left|G_{z\phi}^{E}\right|$ for a magnetic dipole pointing in ϕ direction, for the geometry shown in Figure III.2, ρ = ρ'=21mm, $\phi-\phi'=10°$, $\varepsilon_{r_1}=2.3$, f=10GHz....43

III.32 $\log_{10}\left|G_{zz}^{H}\right|$ for a magnetic dipole pointing in z direction, for the geometry shown in Figure III.2, ρ = ρ'=21mm, $\phi-\phi'=15°$, $\varepsilon_{r_1}=2.3$, f=10GHz....43

III.33 $\log_{10}\left|\int G_{z\phi}^{H}dz\right|$ for a magnetic dipole pointing in ϕ direction, for the geometry shown in Figure III.2, ρ=ρ'=21mm, $\phi-\phi'=15°$, $\varepsilon_{r_1}=5$, f=10GHz.....44

IV.1 Location of the surface wave poles.....47

IV.2 Region 0: PEC, Region 1: ε_{r_1}, $\mu_{r_1}=1$, Region 2: free space, $\rho'=\rho$, $\phi'=0°$, $\phi=30°$.....50

IV.3 The exact and the spatial-domain Green's function G_{zz} with and without extraction of surface wave poles for source and observation point difference $\log_{10}\left|k_0(z-z')\right|$ up to 1 when the deformed path parameters are changed (T_1=0.1, T_2=0.3, T_3=5), f =6.8GHz, $\varepsilon_{r_1}=10$, $\rho'=\rho$ = 0.47λ$_0$, a_1=0.47λ$_0$, t_h = 0.02λ$_0$.....51

IV.4 The exact and the spatial-domain Green's function G_{zz} with and without extraction of surface wave poles for source and observation point difference $\log_{10}\left|k_0(z-z')\right|$ up to 21 when the deformed path parameters are changed (T_1=0.1, T_2=0.3, T_3=5), f =6.8GHz, $\varepsilon_{r_1}=10$, $\rho'=\rho$ = 0.47λ$_0$, a_1= 0.47λ$_0$, t_h = 0.02λ$_0$.....52

IV.5 The spatial-domain Green's function G_{zz} with and without extraction of surface wave poles for source and observation point difference $\log_{10}\left|k_0(z-z')\right|$ up to 1 when the deformed path parameters are changed (T_1=0.1, T_2=0.3, T_3=5), f =4.7GHz, $\varepsilon_{r_1}=2.3$, $\rho'=\rho$ = 0.42λ$_0$, a_1= 0.42λ$_0$, t_h = 0.02λ$_0$.....53

IV.6 The spatial-domain Green's function G_{zz} with and without extraction of surface wave poles for source and observation point difference $\log_{10}\left|k_0(z-z')\right|$ up to 2 when the deformed path parameters are changed (T_1=0.1, T_2=0.3, T_3=5), f =4.7GHz, $\varepsilon_{r_1}=2.3$, $\rho'=\rho$ = 0.42λ$_0$, a_1= 0.42λ$_0$, t_h = 0.02λ$_0$.....53

IV.7 The spatial-domain Green's function G_{zz} with and without extraction of surface wave poles for source and observation point difference $\log_{10}|k_0(z-z')|$ up to 1 when the deformed path parameters are changed (T_1=0.1, T_2=0.3, T_3=5), f =4.7GHz, $\varepsilon_{r_1}=10$, $\rho'=\rho$ = 0.24λ_0, a_1= 0.24λ_0, t_h =0.04λ_0.....54

IV.8 The spatial-domain Green's function G_{zz} with and without extraction of surface wave poles for source and observation point difference $\log_{10}|k_0(z-z')|$ up to 2 when the deformed path parameters are changed (T_1=0.1, T_2=0.3, T_3=5), f =4.7GHz, $\varepsilon_{r_1}=10$, $\rho'=\rho$ = 0.24λ_0, a_1= 0.24λ_0, t_h =0.04λ_0.....55

IV.9 The exact and the spatial-domain Green's function G_{zz} without extraction of surface wave poles, f =6.8GHz, $\varepsilon_{r_1}=10$, $\rho'=\rho$ = 0.47λ_0, a_1= 0.47λ_0, t_h = 0.02λ_0.....56

IV.10 The exact and the spatial-domain Green's function G_{zz} without extraction of surface wave poles, f =4.7GHz, $\varepsilon_{r_1}=2.3$, $\rho'=\rho$ = 0.42λ_0, a_1= 0.42λ_0, t_h = 0.02λ_0.....57

IV.11 The exact and the spatial-domain Green's function G_{zz} without extraction of surface wave poles, f =4.7GHz, $\varepsilon_{r_1}=2.3$, $\rho'=\rho$ = 0.34λ_0, a_1= 0.34λ_0, t_h = 0.04λ_0.....57

V.1 A 3-layer structure with Region 0: PEC, Region 1: ε_{r_1} =2.3, μ_{r_1} =1, Region 2: free space, the first and second strips on ρ =a_1 are placed at ϕ_1 and ϕ_2, respectively……..61

V.2 Rooftop Functions.....62

V.3 A 3-layer structure with Region 0: ε_{r_0} =2, μ_{r_0} =1, Region 1: ε_{r_1} =5, μ_{r_1} =1, Region 2: free space…….65

V.4 Equivalence Principle.....66

V.5 Equivalent magnetic current distributions on each slot.....67

V.6 Definitions of two-port parameters.....69

V.7 A 3-layer structure with Region 0: PEC, Region 1: ε_{r_1} =2.3, μ_{r_1} =1, Region 2: free space, a_0= 20mm, a_1= 21mm, f =4.7 GHz, the first and second strip on ρ=a_1 are placed at ϕ=ϕ_1 and ϕ=ϕ_2, respectively……...72

V.8 The magnitude of the electric current distribution on the first strip, L=$\lambda_0/2$, w=0.025 λ_0, (ϕ_1-ϕ_2)=$\pi/24$ radians, for different feed positions, where zfi is the i'th feed location of the first strip.……...72

V.9 The magnitude of the electric current distribution on the second strip, L= $\lambda_0/2$, w=0.025 λ_0, (ϕ_1 - ϕ_2)=$\pi/24$ radians, for different feed positions, where zfi is the i'th feed location of the first strip..……73

V.10 Real and Imaginary parts of the mutual impedance Z_{21} between two identical z-directed strips versus separation when f =4.7 GHz, a_1=0.5 λ_0...……74

V.11 Real and Imaginary parts of the mutual impedance Z_{21} between two identical z-directed strips versus separation, when f =4.7 GHz, a_1=0.3 λ_0...……74

V.12 Real and Imaginary parts of the mutual impedance Z_{12} between two identical z-directed strips versus separation when f =2 GHz, a_1=0.5 λ_0...……75

V.13 Mutual impedance Z_{21} for H-plane coupling case of two z-directed strips at f =4.7 GHz, a_0=20mm, a_1=21mm, ε_{r_1} =2.3, L=$\lambda_0/2$...……..75

V.14 Mutual coupling coefficient S_{21} for H-plane coupling case of two z-directed strips at f=4.7 GHz, a_0=20mm, a_1=21mm, ε_{r_1} =2.3, L=$\lambda_0/2$...…..76

V.15 A 3-layer structure with Region 0: ε_{r_1} =5, μ_{r_1} =1 Region 1: ε_{r_1} =2, μ_{r_1} =1, Region 2: free space, a_0= 20mm, a_1= 21mm, f =4.7GHz...……..76

V.16 The magnetic current distribution on the first slot for different feed locations when (ϕ_1 - ϕ_2)=$\pi/48$, where zfi is the i'th feed location...……77

V.17 The magnetic current distribution on the second slot for different feed locations when (ϕ_1 - ϕ_2)=$\pi/48$, where zfi is the i'th feed location...……77

V.18 Geometry used for mutual coupling between two z-directed narrow slots..……78

V.19 Mutual impedance Z_{21} for H-plane coupling case of two z-directed narrow slots at f =2 GHz, a_0=20mm, a_1=21mm, $\Delta z = 0$, ε_{r_0} =2, ε_{r_1} =5, L=$\lambda_0/2$.....79

V.20 Mutual impedance Z_{21} for H-plane coupling case of two z-directed narrow slots at f =2 GHz, a_0=20mm, a_1=21mm, $\Delta z = \lambda_0/4$, ε_{r_0} =2, ε_{r_1} =5, L=$\lambda_0/2$.....79

V.21 Mutual coupling coefficient S_{21} for H-plane coupling case of two z-directed narrow slots at f =2 GHz, a_0=20mm, a_1=21mm, $\Delta z = 0$, ε_{r_0} =2, ε_{r_1} =5, L=λ_0/2.....80

V.22 Mutual coupling coefficient S_{21} for H-plane coupling case of two z-directed narrow slots at f =2 GHz, a_0=20mm, a_1=21mm, $\Delta z = \lambda_0/4$, ε_{r_0} =2, ε_{r_1} =5, L=λ_0/2.....80

C.1 Rooftop Functions.....96

C.2 Evaluation of C_{11}.....97

C.3 Evaluation of C_{12}.....97

C.4 Evaluation of C_{13}.....98

C.5 Evaluation of C_{14}.....98

D.1 Geometrical illustration of the Newton-Raphson method.....104

CHAPTER I

INTRODUCTION

Due to the advantages of microstrip antennas such as their low weight, low cost and flexibility, microstrip geometries mounted on multilayer structures have become very popular in various applications ranging from satellite and vehicular communications and remote sensing to radiators in biomedical applications [1], [2].

The importance of cylindrically layered structures have led to the investigation of the scattering from infinite conducting, dielectric or dielectric-coated conducting cylinders and the radiation from patches, microstrip lines on cylindrical structures and cylindrical-rectangular, wraparound microstrip antennas [3]-[19].

The Method of Moments (MoM) is the most frequently used numerical technique to solve the problems of microstrip geometries mounted on multilayer structures. In this method, the integral equation is transformed into a matrix equation by approximating the unknown function interms of known basis functions, then using testing functions the boundary conditions are applied to minimize the weighted error due to this approximation. The MoM procedure can be applied either in the spatial domain or in the spectral domain. In the spectral domain, the MoM matrix elements involve multi-dimensional integrals of complex, oscillatory and slow-converging functions over an infinite domain. The numerical evaluation of these elements is quite time-consuming that makes the technique computationally inefficient. In contrast with the spectral domain MoM, the spatial domain MoM can be considered to be a more general and promising way for solving large and complex problem, as it can easily be applied to objects of arbitrary shape and particularly when the Fourier transform can not be applied to formulate and simplify the Green's functions of the problem. The

spatial domain MoM has also more potential to enhance its capability to solve real and large problem by computing with fast algorithms.

When MoM is applied in the spatial domain, matrix filling is very time-consuming. The reason for that is the spatial domain Green's functions have to be calculated point by point by evaluating the Sommerfeld integral and the numerical evaluation of the integral is neither easy nor fast. Hence, the closed-form solution to the Green's functions becomes necessary.

Several forms of Green's functions for multilayer cylindrical structures are present in the literature [20], [21]. The idea of closed-form spatial domain Green's functions was proposed by [22] and then extended to planarly layered structures to avoid such an integration [23]-[25]. The derivation of the closed form spatial domain Green's function is a robust technique which is obtained by approximating the spectral domain Green's function in terms of complex exponential functions in three consecutive steps on a deformed integration path and then transforming these exponential functions into the spatial domain, analytically [26] for a general cylindrically multilayered medium.

This technique eliminates the requirement of the tedious and time consuming transformation by the numerical integration of the inverse Fourier integral along the real axis on the complex k_z plane where branch-point singularities are encountered. Therefore, the spatial domain Green's functions are obtained in closed forms rather than integral representations. This increases the numerical efficiency in the computation of the spatial domain Green's functions. Therefore, analysis of many problems such as the radiation from microstrips, patches and slots mounted on cylindrical surfaces, and scattering from dielectric shells and cylinders can be improved, considerably. Furthermore, analysis of conformal structures that are extensively used in satellite and vehicular communications become easier by the closed form spatial domain Green's functions.

Under the scope of this thesis, the spectral domain Green's functions were derived from the beginning. Then the code is reproduced in MATLAB® to obtain the spatial domain Green's functions of the electric and magnetic fields due to ϕ and z oriented electric and magnetic sources as [26]. The generated code computes the spatial domain closed-forms of $\tilde{G}^E_{zz}, \tilde{G}^H_{zz}, \tilde{G}^E_{\phi z}, \tilde{G}^H_{\phi z}$ for an electric

and a magnetic dipole pointing in *z* direction, the spatial domain closed-forms of $\tilde{G}^{E}_{z\phi}, \tilde{G}^{H}_{z\phi}, \tilde{G}^{E}_{\phi\phi}, \tilde{G}^{H}_{\phi\phi}$ for an electric and a magnetic dipole pointing in ϕ direction where $\tilde{G}^{E,H}_{\alpha\beta}$ is the electric or magnetic spectral domain Green's function in α direction due to β–oriented source. They were found to be in good agreement with those given in [26]. The spatial domain closed-forms of $\tilde{G}^{E}_{\rho z}, \tilde{G}^{H}_{\rho z}$ for an electric and a magnetic dipole pointing in *z* direction, $\tilde{G}^{E}_{\rho\phi}, \tilde{G}^{H}_{\rho\phi}$ for an electric and a magnetic dipole pointing in ϕ direction that are not provided in [26] were also derived and evaluated by the generated code. Therefore for ϕ and *z* oriented electric and magnetic sources the complete set is obtained.

In addition to these, $\tilde{G}^{E}_{z\rho}, \tilde{G}^{H}_{z\rho}, \tilde{G}^{E}_{\phi\rho}, \tilde{G}^{H}_{\phi\rho}, \tilde{G}^{E}_{\rho\rho}, \tilde{G}^{H}_{\rho\rho}$ for both electric and magnetic dipole sources pointing in ρ direction were derived analytically and the spatial domain closed-forms of these were evaluated by the generated code. Therefore, the complete set of spatial domain dyadic Green's function components has been completed and is evaluated by that code. A new code is generated to evaluate Sommerfeld integral numerically to compare the approximate closed-form Green's functions with the exact ones. The closed-form Green's function components can also be obtained for lossy dielectric media. The application examples of the closed-form Green's function components for lossy dielectric media are shown in Chapter III.

In a previously reported work [27], an approach to overcome the problem for $\bar{\rho} = \bar{\rho}'$, i.e., $\rho = \rho'$ and $\phi = \phi'$ is proposed. Using a similar procedure reported in this work, Green's functions when $\rho = \rho'$ are calculated and some closed-form Green's function results are presented. For small (ϕ -ϕ') values, the exact and our closed-form Green's functions are plotted together and it is observed that they are in good agreement.

While using MoM to calculate mutual coupling of electric or magnetic current elements on a cylindrically layered structure a hybrid method is used. For the calculation of MoM matrix entries, when $\rho = \rho'$, and ϕ is not close to ϕ', closed-form Green's functions are employed. When ϕ is close to ϕ', the problem

is handled by calculating MoM matrix elements in the spectral domain. The technique is applied to both printed dipoles and slots placed on layered cylindrical structures. The computational efficiency of the anaysis of mutual coupling between printed elements on cylindrically layered structures is increased with the use of proposed hybrid method due to use of closed-form Green's functions.

Additionally, the surface wave contribution in cylindrically stratified media is investigated. In that study, the effect of the surface wave poles and the selection of the deformed path parameters are studied. The observations include different frequencies f, the cylinder radius a_1, the dielectric constant ε_{r_1}. When the deformed path parameters are selected in such a way that the deformed path passes close to the surface wave poles, it is observed that the spectral domain Green's functions hence the spatial domain Green's functions deteriorate. This deterioration is overcome by removing the surface wave poles from the spectral domain Green's functions and adding their contributions in the spatial domain. When a proper deformed path is used in evaluation of spatial-domain Green's functions, it is observed from the given plots that removing the surface wave contributions from spectral-domain Green's functions does not give an extra benefit. Hence regarding our research, unlike planar layered medium, it is not a critical issue to remove the surface wave contributions from the spectral-domain Green's functions if a proper deformed path is used.

Chapter II deals with the spectral-domain Green's functions of a cylindrical multilayered media. In Chapter III, the spatial-domain Green's functions and the numerical results are presented. In Chapter IV, the work related with the surface wave contribution is provided and some results are presented.

In Chapter V, the mutual coupling between electric and magnetic current elements on a dielectric coated cylinder with different parameters and some calculated results are compared with available results found in the literature. Finally, concluding remarks are presented in Chapter VI. At last, four Appendices are provided. In Appendix A, the Generalized Pencil of Function (GPOF) method which was used in approximating Green's functions with complex exponentials, is given. The complete set of spectral domain dyadic

Green's function components is given in Appendix B. In Appendix C, rooftop current modes and their analytical evaluation of convolutional integral are provided. In Appendix D, Newton-Raphson method is presented. Throughout the analysis presented in this thesis, $e^{j\omega t}$ time dependence is assumed.

CHAPTER II

SPECTRAL DOMAIN GREEN'S FUNCTIONS IN CYLINDRICALLY LAYERED MEDIA

II.1. Introduction

In this chapter, the spectral domain Green's functions reported in [26] are evaluated using a generated code in MATLAB®. The remaining spectral domain Green's function components which are not given in [26] are also derived and given. Hence, the complete set of dyadic Green's function components for cylindrically stratified media have been obtained. These spectral domain expressions are transformed into spatial domain analytically in closed-forms to be used in mutual coupling analysis of printed elements as will be mentioned in Chapter III.

II.2. Field Expressions for Cylindrically Multilayered Media

A general cylindrically multilayered geometry is shown in Figure II.1. An electric or magnetic source of ρ, z or ϕ orientation is embeded in region j and the observation point may be located in any layer, denoted by region i. Layers may vary in their electric or magnetic properties (ε,μ) as well as the thickness, the layers may also be lossy. Moreover, a perfect electric conductor (PEC) or perfect magnetic conductor (PMC) can be considered as a layer. Unlike in planarly and spherically layered media, TE and TM waves are coupled together at an interface in cylindrically layered media. This requires simultaneous solution of the fields corresponding to TE and TM cases, the only exceptions are the rotationally symmetric (n=0) and z-invariant (k_z=0) cases for which separate analyses of TE and TM modes are possible. Hence, the coupled-mode analysis

for cylindrically layered structures results in 2x2 reflection and transmission matrices rather than reflection and transmission coefficients.

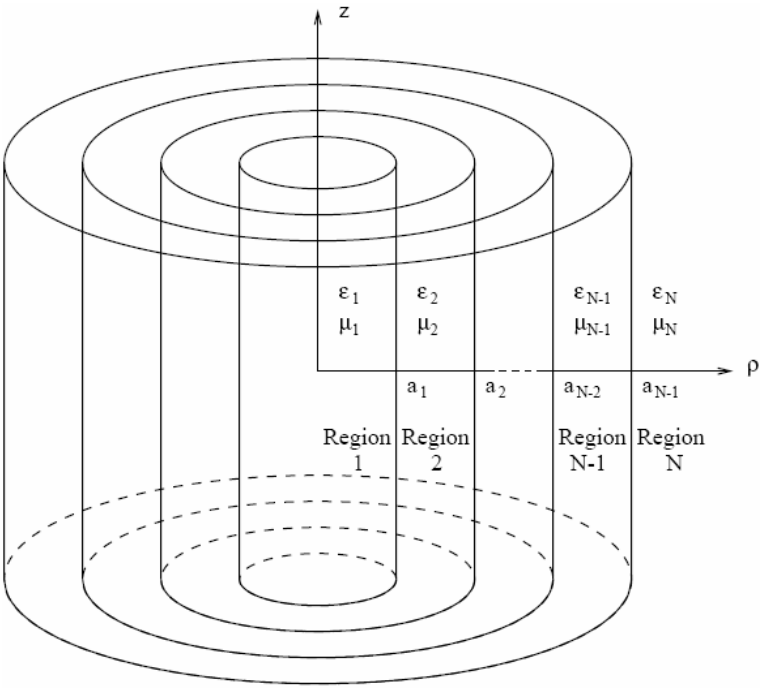

Figure II.1 General cylindrically multilayered medium

In general, a $\hat{\beta}$ oriented point electric or magnetic source is represented by a current element

$$\vec{J}(r) = Il\,\hat{\beta}\,\delta(\vec{r} - \vec{r}') \tag{II.1}$$

where $\hat{\beta}$ may be z, ϕ or ρ, Il is the current moment, $\vec{r}$ and $\vec{r}'$ are the radial vectors showing the locations of source and observation points, respectively.

A general multiple interface geometry of N layers which contains a source in the j^{th} layer at $\rho = \rho'$, is shown in Figure II.2, where the dispersion of waves through the layers is demonstrated [28]-[35].

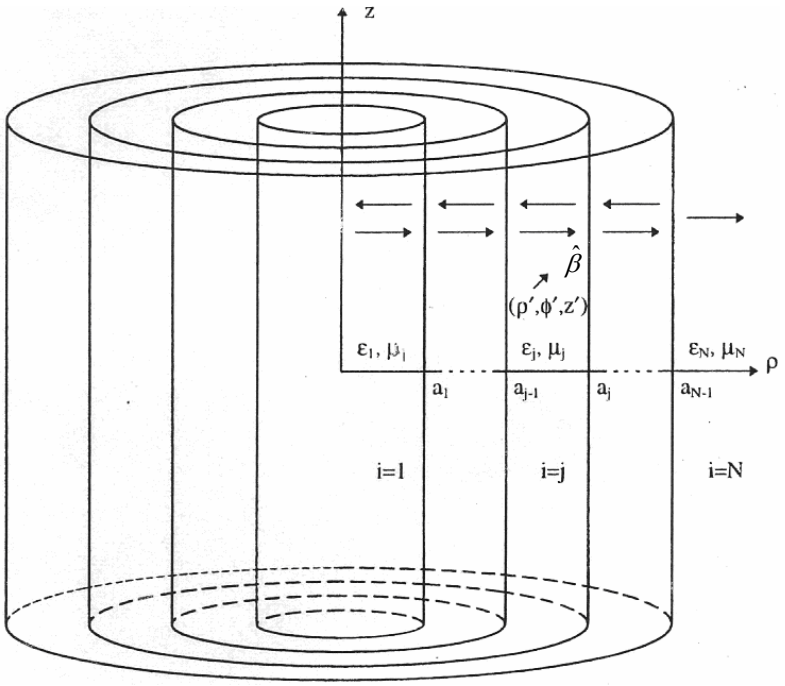

Figure II.2 Dispersion of waves through general multiple interface geometry

First, the axial components (i.e. *z* components) of the spectral-domain electric and magnetic fields are derived for the coupled TE and TM modes in the source layer, then these field components are transferred into the observation layer using a recursive algorithm [26]. The axial components of the electric and magnetic fields in the source layer j can be written as a sum of the direct term due to the source, the standing and outgoing waves formed by the multiple reflections from outer and inner boundaries of the source layer, respectively, represented by first-kind Bessel and second-kind Hankel functions [26]

$$\begin{bmatrix} E_{z_j} \\ H_{z_j} \end{bmatrix} = -\frac{Il}{8\pi\omega}\sum_{n=-\infty}^{\infty} e^{jn(\phi-\phi')}\int_{-\infty}^{\infty} dk_z e^{-jk_z(z-z')} \left\{ J_n(k_{\rho_j}\rho_<)H_n^{(2)}(k_{\rho_j}\rho_>)\bar{\mathrm{I}} + J_n(k_{\rho_j}\rho)\overline{\mathrm{A}}_{n_s} + H_n^{(2)}(k_{\rho_j}\rho)\overline{\mathrm{A}}_{n_o} \right\}.\overleftarrow{S}_n \tag{II.2}$$

where $\bar{\mathrm{I}}$ is the unit matrix, $\rho_<$ is the smaller of ρ and ρ', $\rho_>$ is the larger of ρ and ρ' and k_z and k_{ρ_i} are, respectively, the axial wave number and radial wave number of the i^{th} layer such that $k_i = \sqrt{k_z^2 + k_{\rho_i}^2}$.

$\overleftarrow{S}_n$ is a 2 x 1 matrix operator of the form

$$\overleftarrow{S}_n = \begin{bmatrix} \frac{1}{\varepsilon_j}(k_j^2 \hat{a}_z + jk_z \vec{\nabla}') \cdot \hat{\beta} \\ -jw\hat{\beta} \cdot (\hat{a}_z \times \vec{\nabla}') \end{bmatrix} \tag{II.3}$$

for the fields due to an electric source,

$$\overleftarrow{S}_n = \begin{bmatrix} jw\hat{\beta} \cdot (\hat{a}_z \times \vec{\nabla}') \\ \frac{1}{\mu_j}(k_j^2 \hat{a}_z + jk_z \vec{\nabla}') \cdot \hat{\beta} \end{bmatrix} \tag{II.4}$$

for the fields due to a magnetic source and $\vec{\nabla}'$ is defined as

$$\vec{\nabla}' = \hat{a}_\rho \frac{\partial}{\partial \rho'} + \hat{a}_\phi \frac{\partial}{\rho' \partial \phi'} + \hat{a}_z \frac{\partial}{\partial z'} \tag{II.5}$$

$\overline{\mathrm{A}}_{n_s}$ and $\overline{\mathrm{A}}_{n_o}$ are the amplitude matrices, respectively, for the n[th] harmonic of the standing and outgoing waves that are reflected from the lower and upper boundaries. The fields at the interfaces which satisfies the boundary conditions gives the amplitude matrices as [26]

$$\begin{aligned} \overline{\mathrm{A}}_{n_s} &= \overline{\tilde{M}}_{j-} . \overline{\tilde{R}}_{j,j+1} \left(J_n(k_{\rho_j} \rho') \bar{\mathrm{I}} + H_n^{(2)}(k_{\rho_j} \rho') \overline{\tilde{R}}_{j,j-1} \right) \\ \overline{\mathrm{A}}_{n_o} &= \overline{\tilde{M}}_{j+} . \overline{\tilde{R}}_{j,j-1} \left(H_n^{(2)}(k_{\rho_j} \rho') \bar{\mathrm{I}} + J_n(k_{\rho_j} \rho') \overline{\tilde{R}}_{j,j+1} \right) \end{aligned} \tag{II.6}$$

where $\overline{\tilde{R}}_{j,j\mp1}$ is the generalized reflection matrix and $\overline{\tilde{M}}_{j\mp} = (\bar{I} - \overline{\tilde{R}}_{j,j\pm1} . \overline{\tilde{R}}_{j,j\mp1})^{-1}$ is a factor accounting for multiple reflections in the source region *j*. The generalized reflection matrix $\overline{\tilde{R}}_{j,j-1}$ contains multiple reflections from the inner layers with respect to layer *j*, while $\overline{\tilde{R}}_{j,j+1}$ contains multiple reflections from the outer layers. The generalized reflection matrix can be defined as

$$\overline{\tilde{R}}_{i,i\pm1} = \overline{R}_{i,i\pm1} + \overline{T}_{i\pm1,i} \overline{\tilde{R}}_{i\pm1,i\pm2} \overline{\tilde{T}}_{i,i\pm1} \tag{II.7}$$

where *i* denotes an arbitrary layer between 1 and N.

$\overline{\overline{T}}_{i,i\pm1}$ is the generalized transmission matrix that transfers the amplitudes from the source region to the observation region and is defined as

$$\overline{\overline{T}}_{i,i\pm1} = (\bar{I} - \overline{R}_{i\pm1,i}\overline{\overline{R}}_{i\pm1,i\pm2})^{-1}\overline{T}_{i,i\pm1} \tag{II.8}$$

$\overline{R}$ and $\overline{T}$ in (II.7) and (II.8) are the local reflection and local transmission matrices, respectively. These matrices contain interactions between the two layers given in their subscripts.

The local reflection matrix $\overline{R}$ is defined as

$$\begin{aligned}\overline{R}_{i,i+1} &= \overline{D}_i^{-1}.\left[H_n^{(2)}(k_{\rho_i}a_i)\overline{H}_n^{(2)}(k_{\rho_{i+1}}a_i) - H_n^{(2)}(k_{\rho_{i+1}}a_i)\overline{H}_n^{(2)}(k_{\rho_i}a_i)\right]\\ \overline{R}_{i+1,i} &= \overline{D}_i^{-1}.\left[J_n(k_{\rho_i}a_i)\bar{J}_n(k_{\rho_{i+1}}a_i) - J_n(k_{\rho_{i+1}}a_i)\bar{J}_n(k_{\rho_i}a_i)\right]\end{aligned} \tag{II.9}$$

The local transmission matrix $\overline{T}$ is defined as

$$\begin{aligned}\overline{T}_{i,i+1} &= \frac{2\omega}{\pi k_{\rho_i}^2 a_i}\overline{D}_i^{-1}.\begin{bmatrix}\varepsilon_i & 0\\ 0 & -\mu_i\end{bmatrix}\\ \overline{T}_{i+1,i} &= \frac{2\omega}{\pi k_{\rho_{i+1}}^2 a_i}\overline{D}_i^{-1}.\begin{bmatrix}\varepsilon_{i+1} & 0\\ 0 & -\mu_{i+1}\end{bmatrix}\end{aligned} \tag{II.10}$$

where

$$\overline{D}_i = \left[H_n^{(2)}(k_{\rho_{i+1}}a_i)\bar{J}_n(k_{\rho_i}a_i) - J_n(k_{\rho_i}a_i)\overline{H}_n^{(2)}(k_{\rho_{i+1}}a_i)\right] \tag{II.11}$$

$H_n^{(2)}(x), \overline{H}_n^{(2)}(x), J_n(x)$ and $\bar{J}_n(x)$, used in equations (II.9)-(II.11), are given as

$$\overline{B}_n(k_{\rho_i}a_i) = \frac{1}{k_{\rho_i}^2 a_i}\begin{bmatrix}-j\omega\varepsilon_i k_{\rho_i}a_i B_n^{'}(k_{\rho_i}a_i) & nk_z B_n(k_{\rho_i}a_i)\\ nk_z B_n(k_{\rho_i}a_i) & j\omega\mu_i k_{\rho_i}a_i B_n^{'}(k_{\rho_i}a_i)\end{bmatrix} \tag{II.12}$$

where $'$ in (II.12) is used for the derivative with respect to $k_{\rho_i}a_i$ such that $\frac{\partial}{\partial(k_{\rho_i}a_i)}$.

II.3. Spectral-domain Green's Functions

Putting (II.6) into (II.2) gives the z-component fields in the source layer j as

$$\begin{bmatrix} E_{z_j} \\ H_{z_j} \end{bmatrix} = -\frac{Il}{8\pi\omega} \sum_{n=-\infty}^{\infty} e^{jn(\phi-\phi')} \int_{-\infty}^{\infty} dk_z e^{-jk_z(z-z')} \overline{F}_n(\rho,\rho').\overleftarrow{S}_{n_j} \tag{II.13}$$

where

$$\overline{F}_n(\rho,\rho') = \begin{cases} \left[J_n(k_{\rho_j}\rho)\bar{I} + H_n^2(k_{\rho_j}\rho)\tilde{\tilde{R}}_{j,j-1} \right] \\ .\tilde{\tilde{M}}_{j-}.\left[H_n^2(k_{\rho_j}\rho')\bar{I} + J_n(k_{\rho_j}\rho')\tilde{\tilde{R}}_{j,j+1} \right], \quad \rho < \rho' \\ \left[H_n^2(k_{\rho_j}\rho)\bar{I} + J_n(k_{\rho_j}\rho)\tilde{\tilde{R}}_{j,j+1} \right] \\ .\tilde{\tilde{M}}_{j+}.\left[J_n(k_{\rho_j}\rho')\bar{I} + H_n^2(k_{\rho_j}\rho')\tilde{\tilde{R}}_{j,j-1} \right], \quad \rho > \rho' \end{cases} \tag{II.14}$$

when source and observation points are in the same region, i.e. $i = j$,

$$\overline{F}_n(\rho,\rho') = \begin{cases} \left[J_n(k_{\rho_i}\rho)\bar{I} + H_n^2(k_{\rho_i}\rho)\tilde{\tilde{R}}_{i,i-1} \right] \\ .\tilde{\tilde{T}}_{j,i}.\tilde{\tilde{M}}_{j-}.\left[H_n^2(k_{\rho_j}\rho')\bar{I} + J_n(k_{\rho_j}\rho')\tilde{\tilde{R}}_{j,j+1} \right], \quad i < j \\ \left[H_n^2(k_{\rho_i}\rho)\bar{I} + J_n(k_{\rho_i}\rho)\tilde{\tilde{R}}_{i,i+1} \right] \\ .\tilde{\tilde{T}}_{j,i}.\tilde{\tilde{M}}_{j+}.\left[J_n(k_{\rho_j}\rho')\bar{I} + H_n^2(k_{\rho_j}\rho')\tilde{\tilde{R}}_{j,j-1} \right], \quad i > j \end{cases} \tag{II.15}$$

when source and observation points are located in regions j and i, respectively.

The Fourier transformation of (II.13) gives the z-components of the fields in spectral domain as [26]

$$\begin{bmatrix} \tilde{E}_{z_j} \\ \tilde{H}_{z_j} \end{bmatrix} = -\frac{Il\, e^{jk_z z'}}{4\omega} \sum_{n=-\infty}^{\infty} e^{jn(\phi-\phi')} \overline{F}_n(\rho,\rho').\overleftarrow{S}_{n_j} \tag{II.16}$$

where $\overline{F}_n(\rho,\rho')$ can also be defined as

$$\overline{F}_n(\rho,\rho') = \begin{bmatrix} f_{11} & f_{12} \\ f_{21} & f_{22} \end{bmatrix} \tag{II.17}$$

The spectral domain fields can be defined as the multiplication of Green's function matrix $\tilde{\tilde{G}}$ and the source matrix $\tilde{\tilde{J}}$ such as $\tilde{\tilde{E}} = \tilde{\tilde{G}}^E . \tilde{\tilde{J}}$ and $\tilde{\tilde{H}} = \tilde{\tilde{G}}^H . \tilde{\tilde{J}}$. Hence, using (II.16) and knowing that Fourier transform of the current source given in (II.1) is $Il\, e^{jk_z z'}$, electric or magnetic spectral domain Green's function in α direction due to β–oriented source, $\tilde{G}_{\alpha\beta}^{E,H}$, can be defined as [26]

$$\tilde{G}_{\alpha\beta}^{E,H} = -\frac{1}{4\omega} \sum_{n=-\infty}^{\infty} e^{jn(\phi-\phi')} \overline{F}_n(\rho,\rho') \overleftarrow{S}_{n_j} \tag{II.18}$$

(II.18) can also be written interms of nth harmonic Green's function $\tilde{G}_{\alpha\beta}^{E_n,H_n}$ as

$$\tilde{G}_{\alpha\beta}^{E,H} = -\frac{1}{4\omega} \sum_{n=-\infty}^{\infty} e^{jn(\phi-\phi')} \tilde{G}_{\alpha\beta}^{E_n,H_n} \tag{II.19}$$

Then, nth harmonic Green's function in z direction due to β–oriented source is

$$\begin{bmatrix} \tilde{G}_{z\beta}^{E_n} \\ \tilde{G}_{z\beta}^{H_n} \end{bmatrix} = \overline{F}_n(\rho,\rho') \overleftarrow{S}_{n_j} = \begin{bmatrix} f_{11} & f_{12} \\ f_{21} & f_{22} \end{bmatrix} \overleftarrow{S}_{n_j} \tag{II.20}$$

The ρ component and ϕ component of the fields can be obtained, respectively, from the z component of the fields as [26]

$$\begin{bmatrix} \tilde{H}_\rho \\ \tilde{E}_\rho \end{bmatrix} = \frac{1}{k_{\rho_i}^2} \begin{bmatrix} -\dfrac{\omega\varepsilon_i n}{\rho} & -jk_z \dfrac{\partial}{\partial\rho} \\ -jk_z \dfrac{\partial}{\partial\rho} & \dfrac{\omega\mu_i n}{\rho} \end{bmatrix} \begin{bmatrix} \tilde{E}_z \\ \tilde{H}_z \end{bmatrix} \tag{II.21}$$

$$\begin{bmatrix} \tilde{H}_\phi \\ \tilde{E}_\phi \end{bmatrix} = \begin{bmatrix} -\dfrac{j\omega\varepsilon_i}{k_{\rho_i}^2} \dfrac{\partial}{\partial\rho} & \dfrac{nk_z}{k_{\rho_i}^2 \rho} \\ \dfrac{nk_z}{k_{\rho_i}^2 \rho} & \dfrac{j\omega\mu_i}{k_{\rho_i}^2} \dfrac{\partial}{\partial\rho} \end{bmatrix} \begin{bmatrix} \tilde{E}_z \\ \tilde{H}_z \end{bmatrix} \tag{II.22}$$

Therefore, using (II.21) and (II.22), ρ and ϕ directed n[th] harmonic Green's functions, respectively, due to β –oriented source are given as

$$\begin{bmatrix} \widetilde{G}^{H_n}_{\rho\beta} \\ \widetilde{G}^{E_n}_{\rho\beta} \end{bmatrix} = \frac{1}{k^2_{\rho_i}} \begin{bmatrix} -\dfrac{\omega\varepsilon_i n}{\rho} & -jk_z \dfrac{\partial}{\partial\rho} \\ -jk_z \dfrac{\partial}{\partial\rho} & \dfrac{\omega\mu_i n}{\rho} \end{bmatrix} \begin{bmatrix} \widetilde{G}^{E_n}_{z\beta} \\ \widetilde{G}^{H_n}_{z\beta} \end{bmatrix} \tag{II.23}$$

$$\begin{bmatrix} \widetilde{G}^{H_n}_{\phi\beta} \\ \widetilde{G}^{E_n}_{\phi\beta} \end{bmatrix} = \begin{bmatrix} -\dfrac{j\omega\varepsilon_i}{k^2_{\rho_i}} \dfrac{\partial}{\partial\rho} & \dfrac{nk_z}{k^2_{\rho_i}\rho} \\ \dfrac{nk_z}{k^2_{\rho_i}\rho} & \dfrac{j\omega\mu_i}{k^2_{\rho_i}} \dfrac{\partial}{\partial\rho} \end{bmatrix} \begin{bmatrix} \widetilde{G}^{E_n}_{z\beta} \\ \widetilde{G}^{H_n}_{z\beta} \end{bmatrix} \tag{II.24}$$

In [26], z and ϕ directed spectral domain Green's functions of electric and magnetic fields, $\widetilde{G}^{E}_{zz}, \widetilde{G}^{H}_{zz}, \widetilde{G}^{E}_{\phi z}, \widetilde{G}^{H}_{\phi z}$, due to z-oriented electric and magnetic sources, z and ϕ directed spectral domain Green's functions of electric and magnetic fields, $\widetilde{G}^{E}_{z\phi}, \widetilde{G}^{H}_{z\phi}, \widetilde{G}^{E}_{\phi\phi}, \widetilde{G}^{H}_{\phi\phi}$, due to ϕ-oriented electric and magnetic sources embedded in an arbitrary layer are given for an arbitrary observation layer. The remaining spatial domain Green's function components which are not given in [26], ρ directed spectral domain Green's functions of electric and magnetic fields, $\widetilde{G}^{E}_{\rho z}, \widetilde{G}^{H}_{\rho z}$ and $\widetilde{G}^{E}_{\rho\phi}, \widetilde{G}^{H}_{\rho\phi}$, due to z and ϕ-oriented electric and magnetic sources, respectively, are also derived analytically and evaluated.

The other remaining spatial domain Green's function components which are not given in [26], z, ϕ and ρ directed spectral domain Green's functions of electric and magnetic fields, $\widetilde{G}^{E}_{z\rho}, \widetilde{G}^{H}_{z\rho}, \widetilde{G}^{E}_{\phi\rho}, \widetilde{G}^{H}_{\phi\rho}, \widetilde{G}^{E}_{\rho\rho}, \widetilde{G}^{H}_{\rho\rho}$, due to ρ-oriented electric and magnetic sources are derived analytically. Therefore, the complete set of spectral domain dyadic Green's function components have been completed. The remaining spatial domain Green's function components that are not given in [26] are also given in this chapter and the complete set of spectral domain dyadic Green's function components are presented in Appendix B for the sake of completeness.

For a z-oriented electric source, ρ directed n[th] harmonic Green's functions of electric and magnetic fields are obtained as

$$\widetilde{G}_{\rho z}^{E_n} = \frac{k_{\rho_j}^2}{\varepsilon_j}\left(-\frac{j}{k_{\rho_i}}\frac{\partial f_{11}}{\partial \rho} + \frac{\omega \mu_0 n}{k_{\rho_i}^2 \rho} f_{21}\right) \tag{II.25}$$

$$\widetilde{G}_{\rho z}^{H_n} = \frac{k_{\rho_j}^2}{\varepsilon_j}\left(-\frac{\omega \varepsilon_0 n}{k_{\rho_i}^2}\frac{f_{11}}{\rho} - j\frac{k_z}{k_{\rho_i}}\frac{\partial f_{21}}{\partial \rho}\right) \tag{II.26}$$

For a z–oriented magnetic source, ρ directed n[th] harmonic Green's functions of electric and magnetic fields are obtained as

$$\widetilde{G}_{\rho z}^{E_n} = \frac{k_{\rho_j}^2}{\mu_j}\left(-\frac{jk_z}{k_{\rho_i}}\frac{\partial f_{12}}{\partial \rho} + \frac{\omega \mu_0 n}{\rho k_{\rho_i}^2} f_{22}\right) \tag{II.27}$$

$$\widetilde{G}_{\rho z}^{H_n} = \frac{k_{\rho_j}^2}{\mu_j}\left(\frac{-\omega \varepsilon_0 n}{k_{\rho_i}^2 \rho} f_{12} - \frac{j}{k_{\rho_i}}\frac{\partial f_{22}}{\partial \rho}\right) \tag{II.28}$$

For a ϕ–oriented electric source, ρ directed n[th] harmonic Green's functions of electric and magnetic fields are obtained as

$$\widetilde{G}_{\rho\phi}^{E_n} = \frac{-jk_z^2 n}{\varepsilon_j \rho' k_{\rho_i}}\frac{\partial f_{11}}{\partial \rho} - \frac{\omega k_z k_{\rho_j}}{k_{\rho_i}}\frac{\partial}{\partial \rho'}\left(\frac{\partial f_{12}}{\partial \rho}\right) + \frac{\omega \mu_0 n^2 k_z}{\rho' k_{\rho_i}^2 \rho \varepsilon_j} f_{21} - \frac{j\omega^2 \mu_0 n k_{\rho_j}}{\rho k_{\rho_i}^2}\frac{\partial f_{22}}{\partial \rho'} \tag{II.29}$$

$$\widetilde{G}_{\rho\phi}^{H_n} = \frac{-\omega \varepsilon_0 n^2}{\rho \varepsilon_j \rho' k_{\rho_i}^2} f_{11} + \frac{j\omega^2 \varepsilon_0 n k_{\rho_j}}{k_{\rho_i}^2 \rho}\frac{\partial f_{12}}{\partial \rho'} - \frac{jnk_z}{\rho' k_{\rho_i} \varepsilon_j}\frac{\partial f_{21}}{\partial \rho} - \frac{\omega k_{\rho_j}}{k_{\rho_i}}\frac{\partial}{\partial \rho'}\left(\frac{\partial f_{22}}{\partial \rho}\right) \tag{II.30}$$

For a ϕ–oriented magnetic source, ρ directed n[th] harmonic Green's functions of electric and magnetic fields are obtained as

$$\widetilde{G}_{\rho\phi}^{E_n} = \frac{\omega k_{\rho_j}}{k_{\rho_i}}\frac{\partial}{\partial \rho'}\left(\frac{\partial f_{11}}{\partial \rho}\right) - \frac{jnk_z}{\mu_j \rho' k_{\rho_i}}\frac{\partial f_{12}}{\partial \rho} + \frac{j\omega^2 \mu_0 n k_{\rho_j}}{k_{\rho_i}^2 \rho}\frac{\partial f_{21}}{\partial \rho'} + \frac{\omega \mu_0 n^2}{\mu_j \rho k_{\rho_i}^2 \rho'} f_{22} \tag{II.31}$$

$$\widetilde{G}_{\rho\phi}^{H_n} = -\frac{jn\omega^2 \varepsilon_0 k_{\rho_j}}{k_{\rho_i}^2 \rho}\frac{\partial f_{11}}{\partial \rho'} - \frac{\omega \varepsilon_0 n^2 k_z}{\rho' k_{\rho_i}^2 \rho \mu_j} f_{12} + \frac{k_z \omega k_{\rho_j}}{k_{\rho_i}}\frac{\partial}{\partial \rho'}\left(\frac{\partial f_{21}}{\partial \rho}\right) - \frac{jk_z^2 n}{\rho' k_{\rho_i} \mu_j}\frac{\partial f_{22}}{\partial \rho} \tag{II.32}$$

For a ρ–oriented electric dipole source, z, ϕ and ρ directed n[th] harmonic Green's functions of electric and magnetic fields are obtained as

$$\widetilde{G}_{z\rho}^{E_n} = (\frac{jk_z}{\varepsilon_j}\frac{\partial f_{11}}{\partial \rho'} + \frac{n\omega}{\rho'} f_{12}) \tag{II.33}$$

$$\widetilde{G}_{\phi\rho}^{E_n} = \frac{1}{k_{\rho_i}^2}\left[\frac{k_z n}{\rho}(\frac{jk_z}{\varepsilon_j}\frac{\partial f_{11}}{\partial \rho'} + \frac{n\omega}{\rho'} f_{12}) + j\omega\mu_i \frac{\partial}{\partial \rho}(\frac{jk_z}{\varepsilon_j}\frac{\partial f_{21}}{\partial \rho'} + \frac{n\omega}{\rho'} f_{22})\right] \tag{II.34}$$

$$\widetilde{G}_{\rho\rho}^{E_n} = \frac{1}{k_{\rho_i}^2}\left[-jk_z \frac{\partial}{\partial \rho}(\frac{jk_z}{\varepsilon_j}\frac{\partial f_{11}}{\partial \rho'} + \frac{n\omega}{\rho'} f_{12}) + \frac{\omega n\mu_i}{\rho}(\frac{jk_z}{\varepsilon_j}\frac{\partial f_{21}}{\partial \rho'} + \frac{n\omega}{\rho'} f_{22})\right] \tag{II.35}$$

$$\widetilde{G}_{z\rho}^{H_n} = \frac{jk_z}{\varepsilon_j}\frac{\partial f_{21}}{\partial \rho'} + \frac{n\omega}{\rho'} f_{22} \tag{II.36}$$

$$\widetilde{G}_{\phi\rho}^{H_n} = \frac{1}{k_{\rho_i}^2}\left[-j\omega\varepsilon_i \frac{\partial}{\partial \rho}(\frac{jk_z}{\varepsilon_j}\frac{\partial f_{11}}{\partial \rho'} + \frac{n\omega}{\rho'} f_{12}) + \frac{k_z n}{\rho}(\frac{jk_z}{\varepsilon_j}\frac{\partial f_{21}}{\partial \rho'} + \frac{n\omega}{\rho'} f_{22})\right] \tag{II.37}$$

$$\widetilde{G}_{\rho\rho}^{H_n} = \frac{1}{k_{\rho_i}^2}\left[-\frac{n\omega\varepsilon_i}{\rho}(\frac{jk_z}{\varepsilon_j}\frac{\partial f_{11}}{\partial \rho'} + \frac{n\omega}{\rho'} f_{12}) - jk_z \frac{\partial}{\partial \rho}(\frac{jk_z}{\varepsilon_j}\frac{\partial f_{21}}{\partial \rho'} + \frac{n\omega}{\rho'} f_{22})\right] \tag{II.38}$$

For a ρ–oriented magnetic dipole source, z, ϕ and ρ directed n[th] harmonic Green's functions of electric and magnetic fields are obtained as

$$\widetilde{G}_{z\rho}^{E_n} = (-\frac{n\omega}{\rho'} f_{11} + \frac{jk_z}{\mu_j}\frac{\partial f_{12}}{\partial \rho'}) \tag{II.39}$$

$$\widetilde{G}_{\phi\rho}^{E_n} = \frac{1}{k_{\rho_i}^2}\left[\frac{k_z n}{\rho}(-\frac{n\omega}{\rho'} f_{11} + \frac{jk_z}{\mu_j}\frac{\partial f_{12}}{\partial \rho'}) + j\omega\mu_i \frac{\partial}{\partial \rho}(-\frac{n\omega}{\rho'} f_{21} + \frac{jk_z}{\mu_j}\frac{\partial f_{22}}{\partial \rho'})\right] \tag{II.40}$$

$$\widetilde{G}_{\rho\rho}^{E_n} = \frac{1}{k_{\rho_i}^2}\left[-jk_z \frac{\partial}{\partial \rho}(-\frac{n\omega}{\rho'} f_{11} + \frac{jk_z}{\mu_j}\frac{\partial f_{12}}{\partial \rho'}) + \frac{\omega\mu_i n}{\rho}(-\frac{n\omega}{\rho'} f_{21} + \frac{jk_z}{\mu_j}\frac{\partial f_{22}}{\partial \rho'})\right] \tag{II.41}$$

$$\widetilde{G}_{z\rho}^{H_n} = (-\frac{n\omega}{\rho'} f_{21} + \frac{jk_z}{\mu_j}\frac{\partial f_{22}}{\partial \rho'}) \tag{II.42}$$

$$\widetilde{G}_{\phi\rho}^{H_n} = \frac{1}{k_{\rho_i}^2}\left[- j\omega\varepsilon_i \frac{\partial}{\partial\rho}(-\frac{n\omega}{\rho'} f_{11} + \frac{jk_z}{\mu_j}\frac{\partial f_{12}}{\partial\rho'}) + \frac{k_z n}{\rho}(-\frac{n\omega}{\rho'} f_{21} + \frac{jk_z}{\mu_j}\frac{\partial f_{22}}{\partial\rho'})\right] \quad \text{(II.43)}$$

$$\widetilde{G}_{\rho\rho}^{H_n} = \frac{1}{k_{\rho_i}^2}\left[- \frac{n\omega\varepsilon_i}{\rho}(-\frac{n\omega}{\rho'} f_{11} + \frac{jk_z}{\mu_j}\frac{\partial f_{12}}{\partial\rho'}) - jk_z \frac{\partial}{\partial\rho}(-\frac{n\omega}{\rho'} f_{21} + \frac{jk_z}{\mu_j}\frac{\partial f_{22}}{\partial\rho'})\right] \quad \text{(II.44)}$$

where f_{ij}'s are given in (II.14), (II.15) and (II.17).

CHAPTER III

CLOSED-FORM GREEN'S FUNCTIONS IN CYLINDRICALLY LAYERED MEDIA

III.1 Introduction

In this chapter, the closed-form Green's functions are presented. The spectral-domain Green's functions which are given in Chapter II are transformed into spatial domain analytically in closed-forms as will be mentioned in this chapter to be used in mutual coupling analysis of printed elements.

III.2 Spatial Domain Green's Functions in Closed-form

Spectral domain Green's functions can be transformed into spatial domain by evaluating the Sommerfeld integral,

$$G^{E,H}(z-z') = \frac{1}{2\pi}\int_{-\infty}^{\infty} e^{-jk_z(z-z')}\widetilde{G}^{E,H}(k_z)dk_z \qquad \text{(III.1)}$$

where $G^{E,H}$ denotes spatial domain Green's function. Since the numerical evaluation of (III.1) has difficulties and is very time consuming, to improve computational efficiency the deformed path [26] given in Figure III.1 is used as the path of integration in (III.1). To obtain the spatial domain Green's functions in closed forms for a cylindrically layered medium, a three-step technique is developed as shown in Figure III.1. The spectral domain Green's functions are approximated in terms of complex exponential functions in three consecutive steps and then these exponential functions are transformed into the spatial domain, analytically.

These spectral domain Green's functions are sampled and approximated in two regions in terms of complex exponentials by using Generalized Pencil of Function (GPOF) method. In the first region, corresponding to the path Γ_3 the

large argument behaviour of the zero-order Hankel functions enables complex exponentials of k_ρ to be represented in terms of Hankel functions. The Sommerfeld identity is used to transform Green's functions into the spatial domain. Green's functions represented by Hankel functions in this region are subtracted from the original Green's functions in the full domain, resulting in Green's functions vanishing outside a limited region. These Green's functions are then approximated in terms of complex exponentials along the two contours Γ_1 and Γ_2 shown in Figure III.1. The path of integration is obtained by deforming the original Sommerfeld integration path [26] to avoid the branch-point singularity associated with a branch-cut and the surface wave pole singularities encountered along the real axis on the complex k_z plane. In this second region, transformation into the spatial domain turns out to be analytical evaluation of two simple contour integrals of exponential functions. Finally, addition of the contributions of each step gives the spatial domain Green's functions in closed forms.

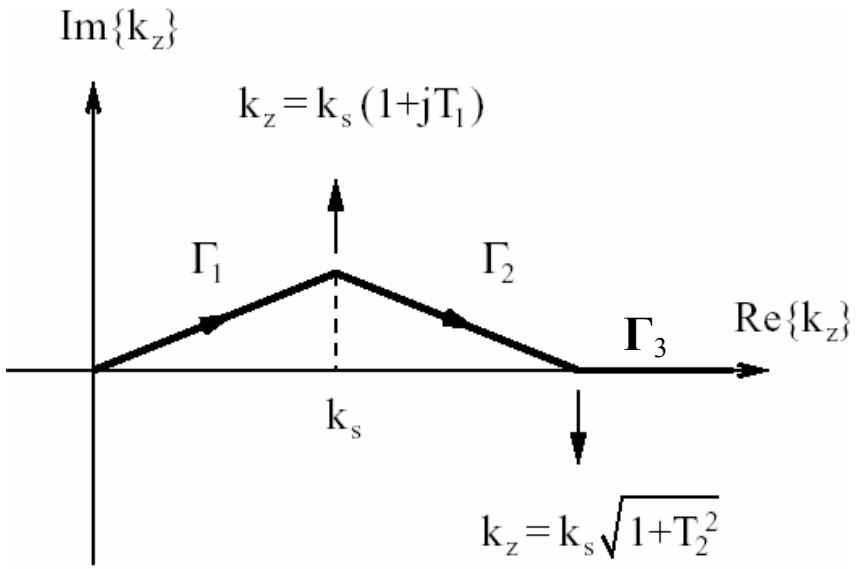

Figure III.1 Deformed path.

In (III.1) since $\widetilde{G}^{E,H}$ is chosen to be an even function of k_z, $\widetilde{G}^{E,H}$ is either $\widetilde{G}^{E,H}$ or $\widetilde{G}^{E,H}/k_z$ depending on whether $\widetilde{G}^{E,H}$ is an even or odd function of k_z, respectively. Hence the inverse Fourier integral (III.1) can be folded as

$$G^{E,H}(z-z') = \frac{1}{\pi}\int_0^{\infty} \cos(k_z(z-z')\widetilde{G}^{E,H}(k_z)dk_z \tag{III.2}$$

The spectral domain Green's functions are sampled and approximated interms of complex exponentials on this deformed path using the GPOF method and then transformed into the spatial domain by applying a three-step approximation technique outlined as follows [26].

1) The spectral domain Green's functions are sampled uniformly along the path

$$\left.\begin{aligned} k_{\rho_s} &= -jk_s(t_3+T_2) \\ k_z &= k_s\sqrt{1+(t_3+T_2)^2} \end{aligned}\right\} 0 \le t_3 < T_3 - T_2 \tag{III.3}$$

where k_s and k_{ρ_s} are the wave numbers of the sampling region that is chosen as the source layer.

The value of T_2 should be large enough to avoid the pole and branch-point singularities and in order for the large argument approximation of the zeroth-order Hankel functions to be valid. Hence, a choice of T_2 such that $k_s\sqrt{1+T_2^2}$ is greater than the wavenumbers of all layers should be appropriate. Once T_2 is chosen, the value of $T_3 \cong 1.1T_2$ is sufficient to capture the behaviour of the Green's functions in the sampling interval.

The sampled Green's functions are multiplied by $\sqrt{k_{\rho_s}}$ and approximated in terms of N_3 complex exponentials of k_{ρ_s} by the GPOF method [36] as

$$\sqrt{k_{\rho_s}}\widetilde{G}_{k_\rho} \cong \sum_{l=1}^{N_3} b_{l_t} e^{s_{l_t}t_3} = \sum_{l=1}^{N_3} b_{l_k} e^{k_{\rho_s}s_{l_k}} \tag{III.4}$$

where $\widetilde{G}_{k_\rho}$ represents the spectral domain Green's functions approximated in this region.

a) The resulting exponential functions are represented by the zeroth-order Hankel functions using the large argument approximation as

$$\widetilde{G}_{k_\rho} \cong \sum_{l=1}^{N_3} b_{l_k} \frac{e^{k_{\rho_s} s_{l_k}}}{\sqrt{k_{\rho_s}}} = \sum_{l=1}^{N_3} b_{l_h} H_0^{(2)}(k_{\rho_s} s_{l_h}) \tag{III.5}$$

b) Then, by using the Sommerfeld identity

$$\frac{e^{-jk_s|\bar{r}-\bar{r}'|}}{|\bar{r}-\bar{r}'|} = -j\int_0^\infty \cos(k_z(z-z')H_0^{(2)}(k_{\rho_s}|\bar{\rho}-\bar{\rho}'|)dk_z \tag{III.6}$$

where $|\bar{r}-\bar{r}'| = \sqrt{(z-z')^2+|\bar{\rho}-\bar{\rho}'|^2}$, the spatial domain Green's functions G_{k_ρ} are obtained as

$$G_{k_\rho} \cong \frac{j}{\pi} \sum_{l=1}^{N_3} b_{l_h} \frac{e^{-jk_s|\bar{r}_l|}}{|\bar{r}_l|} \tag{III.7}$$

where $|\bar{r}_l| = \sqrt{(z-z')^2+s_{l_h}^2}$.

2) The spectral domain Green's functions $\widetilde{G}_{k_\rho}$ approximated in the first step are subtracted from the original Green's functions $\widetilde{G}$ to yield the Green's functions $\widetilde{G}_{k_z}$ vanishing for $k_z \geq k_s\sqrt{1+T_2^2}$.

a) The resulting Green's functions $\widetilde{G}_{k_z}$ are sampled uniformly along the two contours Γ_1 and Γ_2 , which are shown in Figure III.1 and given respectively as

$$k_z = k_s(1+jT_1)\frac{t_1}{T_1}, \qquad 0 \leq t_1 \leq T_1 \tag{III.8}$$

$$k_z = k_s\left[1+jT_1+(\sqrt{1+T_2^2}-1-jT_1)\frac{t_2}{T_2-T_1}\right], \qquad 0 \leq t_2 \leq T_2-T_1 \tag{III.9}$$

b) Along the paths (III.8) and (III.9), the maximum deviation from the original path occurs at $t_1 = T_1$ or $t_2 = 0$. Therefore the deformation of the path can be controlled by choosing T_1 properly. This parameter should be sufficiently large to

overcome the effects of the pole and branch-point singularities and small enough to avoid numerical difficulties. For a robust and safe approximation, T_1 should be chosen that $k_s T_1 \cong 0.1 k_0$, where k_0 is the wavenumber of free space.

c) The sampled Green's functions are approximated in terms of N_1 and N_2 complex exponentials of k_z by GPOF method, respectively, on paths (III.8) and (III.9) as

$$\begin{aligned} \widetilde{G}_{k_z} &\cong \sum_{m=1}^{N_1} b_{m_t} e^{s_{m_t} t_1} + \sum_{n=1}^{N_2} b_{n_t} e^{s_{n_t} t_2} \\ &\cong \sum_{m=1}^{N_1} b_{m_k} e^{k_z s_{m_k}} + \sum_{n=1}^{N_2} b_{n_k} e^{k_z s_{n_k}} \end{aligned} \tag{III.10}$$

d) Transformation of the approximated Green's functions into the spatial domain turns out to be a simple contour integral of exponential functions as

$$G_{k_z} = \frac{1}{\pi} \int_{\Gamma_1 + \Gamma_2} \cos(k_z (z - z')) \widetilde{G}_{k_z} dk_z \tag{III.11}$$

Addition of the contributions given in (III.7) and (III.11) of the three steps yields the spatial domain Green's functions in closed forms as follows:

$$\begin{aligned} G^{E,H}(z - z') = & \frac{1}{2\pi} \sum_{m=1}^{N_1} b_{m_k} \left(\frac{e^{k_s (1 + jT_1)\left[s_{m_k} + j(z - z') \right]} - 1}{s_{m_k} + j(z - z')} + \frac{e^{k_s (1 + jT_1)\left[s_{m_k} - j(z - z') \right]} - 1}{s_{m_k} - j(z - z')} \right) \\ & + \frac{1}{2\pi} \sum_{n=1}^{N_2} b_{n_k} \left(\frac{e^{k_s \sqrt{1 + T_2^2}\left[s_{n_k} + j(z - z') \right]} - e^{k_s (1 + jT_1)\left[s_{n_k} + j(z - z') \right]}}{s_{n_k} + j(z - z')} \right. \\ & \left. + \frac{e^{k_s \sqrt{1 + T_2^2}\left[s_{n_k} - j(z - z') \right]} - e^{k_s (1 + jT_1)\left[s_{n_k} - j(z - z') \right]}}{s_{n_k} - j(z - z')} \right) \\ & + \frac{j}{\pi} \sum_{l=1}^{N_3} b_{l_h} \frac{e^{-jk_s \sqrt{(z - z')^2 + s_{l_h}^2}}}{\sqrt{(z - z')^2 + s_{l_h}^2}} \end{aligned} \tag{III.12}$$

In [26], z and ϕ directed spatial domain Green's functions of electric and magnetic fields, $G_{zz}^E, G_{zz}^H, G_{\phi z}^E, G_{\phi z}^H$, due to z-oriented electric and magnetic sources,

z and ϕ directed spatial domain Green's functions of electric and magnetic fields, $G^E_{z\phi}, G^H_{z\phi}, G^E_{\phi\phi}, G^H_{\phi\phi}$, due to ϕ-oriented electric and magnetic sources embedded in an arbitrary layer are given for an arbitrary observation layer. The remaining spatial domain Green's function components which are not given in [26], ρ directed spatial domain Green's functions of electric and magnetic fields, $G^E_{\rho z}, G^H_{\rho z}$ and $G^E_{\rho\phi}, G^H_{\rho\phi}$, due to z and ϕ-oriented electric and magnetic sources, respectively, are also evaluated.

The other remaining spatial domain Green's function components which are not given in [26], z, ϕ and ρ directed spatial domain Green's functions of electric and magnetic fields, $G^E_{z\rho}, G^H_{z\rho}, G^E_{\phi\rho}, G^H_{\phi\rho}, G^E_{\rho\rho}, G^H_{\rho\rho}$, due to ρ-oriented electric and magnetic sources are evaluated. Therefore, the complete set of spatial domain dyadic Green's function components have been completed. The plots of remaining spatial domain Green's function components which are not given in [26] are shown in Section III.4.

III.3 Closed-form Green's Functions when $\rho = \rho'$

The spatial domain Green's functions in [26] can only be evaluated when ρ is not equal to ρ'. However, when MoM is applied in the spatial domain, the spatial domain Green's functions at $\rho = \rho'$ is needed.

If ρ is far away from ρ', the cylindrical eigenmodes in the summation in (II.19) form a fast convergent series. However, it is not the case when ρ and ρ' are close to each other. When ρ and ρ' are close to each other, the convergence behaviour of the series is very poor and a large amount of eigenmodes are needed to achieve a convergent result. To make the series representations of these Green's functions convergent in spectral domain when $\rho = \rho'$ a similar procedure reported in [27] is employed.

To demonstrate the procedure, the spectral domain Green's function $\widetilde{G}^E_{zz}$ can be considered, where $\widetilde{G}^E_{zz}$ has a summation term $S_1 = \sum_{-\infty}^{\infty} f_{11} e^{jn(\phi-\phi')}$ that has a

convergence problem when $\rho = \rho'$, therefore infinite number of terms are needed to obtain a convergent result. It is realized that the quasistatic components of f_{11} are slowly convergent, on the other hand the inverse Fourier transform of the quasistatic components has a closed form. After the quasistatic components are completely extracted from the Green's functions in spectral domain, the remaining parts have good convergence behaviours which can be used to speed up the calculation of the inverse Fourier transform. Then the quasistatic components are transformed into spatial domain analytically and their contributions are added in closed form [27].

The summation term, S_1 can be expressed as

$$S_1 = \sum_{-\infty}^{\infty} \frac{f_{11}}{(H_n^{(2)}(k_{\rho_i}\rho)J_n(k_{\rho_i}\rho'))}(H_n^{(2)}(k_{\rho_i}\rho)J_n(k_{\rho_i}\rho'))e^{jn(\phi-\phi')} = \sum_{-\infty}^{\infty} C_1(H_n^{(2)}(k_{\rho_i}\rho)J_n(k_{\rho_i}\rho'))e^{jn(\phi-\phi')} \quad \text{(III.13)}$$

The coefficient C_1 depends on n and k_z; if k_z is fixed then C_1 only depends on n. With increasing n, C_1 has an asymptotic value denoted as C_1^*. C_1^* is independent of n, but depends on k_z.

$$\lim_{n\to\infty} C_1(n,k_z) \cong C_1^*(k_z) \quad \text{(III.14)}$$

While moving along the Sommerfeld integration path on Γ_3 path, C_1^* is found to be almost a constant that is denoted as C_1^{**}; hence C_1^{**} is independent of n and k_z.

$$\lim_{k_z\to\infty} C_1^*(k_z) \cong C_1^{**} \quad \text{(III.15)}$$

$$\begin{aligned} S_1 &= \sum_{-\infty}^{\infty}(C_1 - C_1^*)\left[H_n^{(2)}(k_{\rho_i}\rho)J_n(k_{\rho_i}\rho')e^{jn(\phi-\phi')}\right] + \sum_{-\infty}^{\infty} C_1^*\left[H_n^{(2)}(k_{\rho_i}\rho)J_n(k_{\rho_i}\rho')e^{jn(\phi-\phi')}\right] \\ &= \sum_{-\infty}^{\infty}(C_1 - C_1^*)\left[H_n^{(2)}(k_{\rho_i}\rho)J_n(k_{\rho_i}\rho')e^{jn(\phi-\phi')}\right] + C_1^* H_0^{(2)}(k_{\rho_i}\left|\overline{\rho} - \overline{\rho}'\right|) \end{aligned} \quad \text{(III.16)}$$

where Addition theorem, given in (3.17), is used to obtain the last term of (III.16)

$$H_0^{(2)}(k_{\rho_j}\left|\overline{\rho}-\overline{\rho}'\right|)=\sum_{n=-\infty}^{\infty}e^{jn(\phi-\phi')}H_n^{(2)}(k_{\rho_j}\rho)J_n(k_{\rho_j}\rho') \tag{III.17}$$

The series in (III.16) is fast decaying, since the asymptotic term C_1^* is subtracted. In (III.18), C_1^{**} is subtracted from C_1^* for a better convergence.

In order to obtain G_{zz} the integral I should be evaluated.

$$I=\int_{-\infty}^{\infty}S_1e^{-jk_z(z-z')}dk_z=\int_{-\infty}^{\infty}\sum_{-\infty}^{\infty}C_1\left[H_n^{(2)}(k_{\rho_j}\rho)J_n(k_{\rho_j}\rho')e^{jn(\phi-\phi')}\right]e^{-jk_z(z-z')}dk_z$$

$$=\int_{-\infty}^{\infty}\sum_{-\infty}^{\infty}(C_1-C_1^*)\left[H_n^{(2)}(k_{\rho_i}\rho)J_n(k_{\rho_i}\rho')\right]e^{jn(\phi-\phi')}e^{-jk_z(z-z')}dk_z$$

$$+\int_{-\infty}^{\infty}(C_1^*-C_1^{**})H_0^{(2)}(k_{\rho_i}\left|\overline{\rho}-\overline{\rho}'\right|)e^{-jk_z(z-z')}dk_z+\int_{-\infty}^{\infty}C_1^{**}H_0^{(2)}(k_{\rho_i}\left|\overline{\rho}-\overline{\rho}'\right|)e^{-jk_z(z-z')}dk_z \tag{III.18}$$

The last integral in (III.18) has a closed form solution as (III.19) using the Sommerfeld identity given in (III.6) and this term is called as the direct term.

$$\int_{-\infty}^{\infty}C_1^{**}H_0^{(2)}(k_{\rho_i}\left|\overline{\rho}-\overline{\rho}'\right|)e^{-jk_z(z-z')}dk_z=2jC_1^{**}\frac{e^{-jk_s\left|\overline{r}-\overline{r}'\right|}}{\left|\overline{r}-\overline{r}'\right|} \tag{III.19}$$

As a summary, the complete procedure can be outlined as follows:

I. The spectral domain Green's functions are evaluated uniformly along the deformed path given in (III.8), (III.9) and (III.3), corresponding to paths Γ_1, Γ_2, Γ_3, respectively.

II. The asymptotic terms C_1^* and C_1^{**} are subtracted to make the remains of the Green's function vanishing on path Γ_3 and are transformed into those in spatial domain in closed form.

III. The resultant Green's functions are sampled uniformly along two deformed paths Γ_1 and Γ_2 and approximated in terms of N_1 and N_2 and the complex exponentials of k_z by the GPOF method given by (III.10).

IV. Transforming the approximated Green's functions $\widetilde{G}_{k_z}$ in the form of (III.10) into the spatial domain turns out to be a simple contour integral of exponentials which have closed form.

III.4 Numerical Results

III.4.1 Closed-form Green's Function Results for $\overline{\rho} \neq \overline{\rho}'$

The first set of numerical results belongs to a case for $\rho \neq \rho'$ which was presented in [26]. The same results are given to verify the accuracy of our code.

Figure III.2 is a dielectric-coated cylinder which is represented by a 3-layer structure in our model. The point electric source is located at the air-dielectric interface $\rho' = a_1$=21mm and the observation point is at ρ = 40mm.

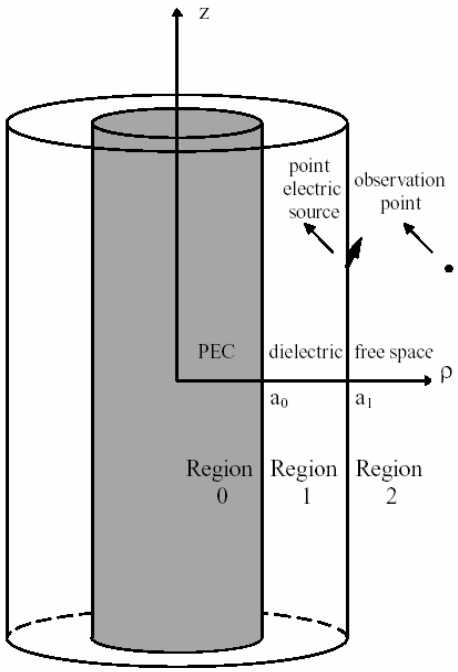

Figure III.2 Region 0: PEC, Region 1: $\varepsilon_{r_1} = 2.3$, $\mu_{r_1} = 1$, Region 2: free space, a_0= 20mm, a_1= 21mm, ρ' = 21mm, ϕ'=0°, ρ = 40mm, ϕ =30°, f= 4.7 GHz.

Our generated code computes the spatial domain closed-forms of spectral domain Green's functions $\widetilde{G}_{zz}^{E}, \widetilde{G}_{zz}^{H}, \widetilde{G}_{\phi z}^{E}, \widetilde{G}_{\phi z}^{H}$ for an electric and a magnetic dipole pointing in *z* direction, the spatial domain closed-forms of $\widetilde{G}_{z\phi}^{E}, \widetilde{G}_{z\phi}^{H}, \widetilde{G}_{\phi\phi}^{E}, \widetilde{G}_{\phi\phi}^{H}$ for an electric and a magnetic dipole pointing in ϕ direction. They are found to be in good agreement with the ones given in [26] as seen in Figure III.3-Figure III.6. Besides, the remaining spatial domain Green's function components that are not given in [26], which are derived analytically and given in Chapter II as (II.25)-(II.32), the spatial domain closed-forms of ρ directed spectral domain Green's functions of electric and magnetic fields, $\widetilde{G}_{\rho z}^{E}, \widetilde{G}_{\rho z}^{H}$ and $\widetilde{G}_{\rho\phi}^{E}, \widetilde{G}_{\rho\phi}^{H}$, due to *z* and ϕ-oriented electric and magnetic sources, respectively, are also given in Figure III.7-Figure III.10. These are compared with the exact Green's functions obtained by the numerical evaluation of the Sommerfeld integral.

To assess the accuracy of the method developed in this thesis, the obtained (approximate) closed-form spatial domain Green's function results are compared with the exact Green's function results. Exact Green's function is calculated using the direct numerical integration of Sommerfeld integral in (III.1) which is also given here for the sake of completeness

$$G^{E,H}(z-z') = \frac{1}{2\pi}\int_{-\infty}^{\infty} e^{-jk_z(z-z')}\widetilde{G}^{E,H}(k_z)dk_z$$

Direct numerical integration is a tedious and time consuming numerical integration of the inverse Fourier integral along the real axis on the complex k_z plane (Sommerfeld integration path) where branch-point singularities and the surface wave poles are encountered. A code is generated which evaluates the spatial-domain Green's function using the direct numerical integration that compares the exact and the approximate closed-form Green's functions.

The other remaining spatial domain Green's function components that are not given in [26], which are derived analytically and given in Chapter II as (II.33)-(II.44), the spatial domain closed-forms of *z*, ϕ and ρ directed spectral domain Green's functions of electric and magnetic fields, $\widetilde{G}_{z\rho}^{E}, \widetilde{G}_{z\rho}^{H}, \widetilde{G}_{\phi\rho}^{E}, \widetilde{G}_{\phi\rho}^{H}, \widetilde{G}_{\rho\rho}^{E}, \widetilde{G}_{\rho\rho}^{H}$, due to ρ-oriented electric and magnetic sources are given in Figure III.11–Figure

III.16. Therefore, the complete set of the spatial domain dyadic Green's function components have been completed. They are again compared and found to be in good agreement with the exact ones.

The closed-form Green's function components can also be obtained for lossy dielectric media where different spatial domain Green's functions are given in Figure III.17–Figure III.20 for the geometry of Figure III.2 for the dielectric constant $\varepsilon_{r_1} = 2.3 - j\,0.1$.

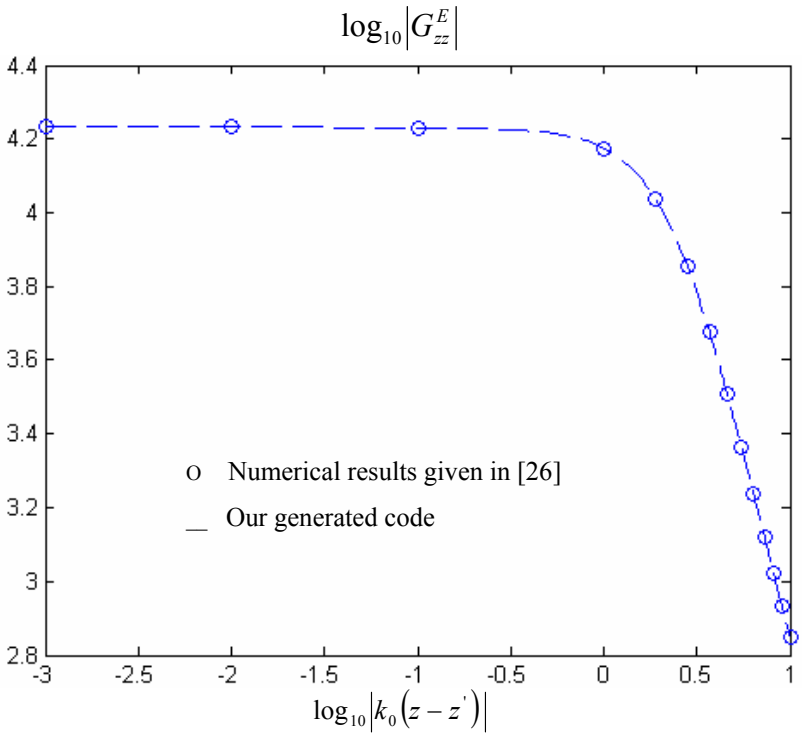

Figure III.3 $\log_{10}\left|G_{zz}^{E}\right|$ for an electric dipole pointing in *z* direction, for the geometry shown in Figure III.2 (N_1=4, N_2=5, N_3=1, T_1=0.1, T_2=4.5, T_3=5).

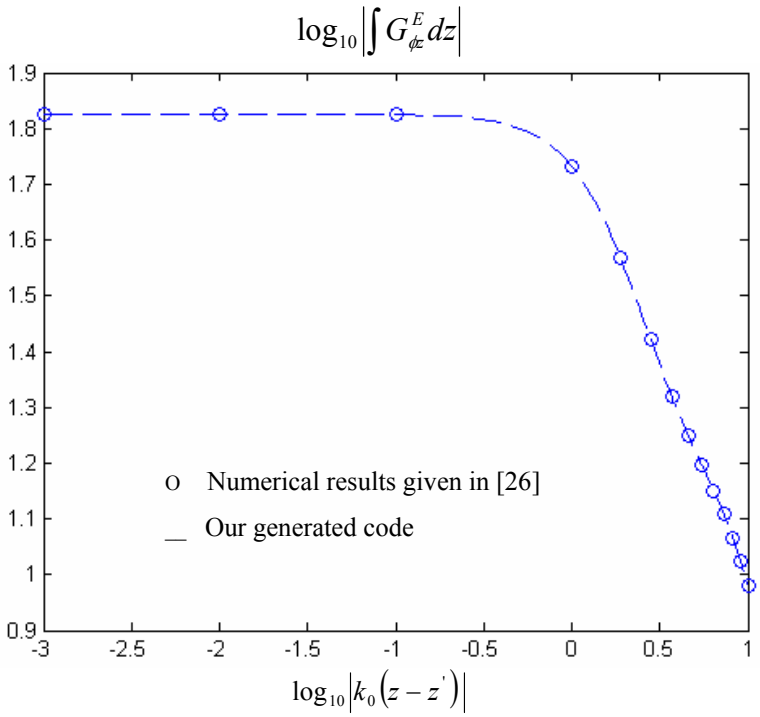

Figure III.4 $\log_{10}\left|\int G_{\phi z}^{E} dz\right|$ for an electric dipole pointing in z direction, for the geometry shown in Figure III.2 (N_1=5, N_2=5, N_3=1, T_1=0.1, T_2=3.5, T_3=4).

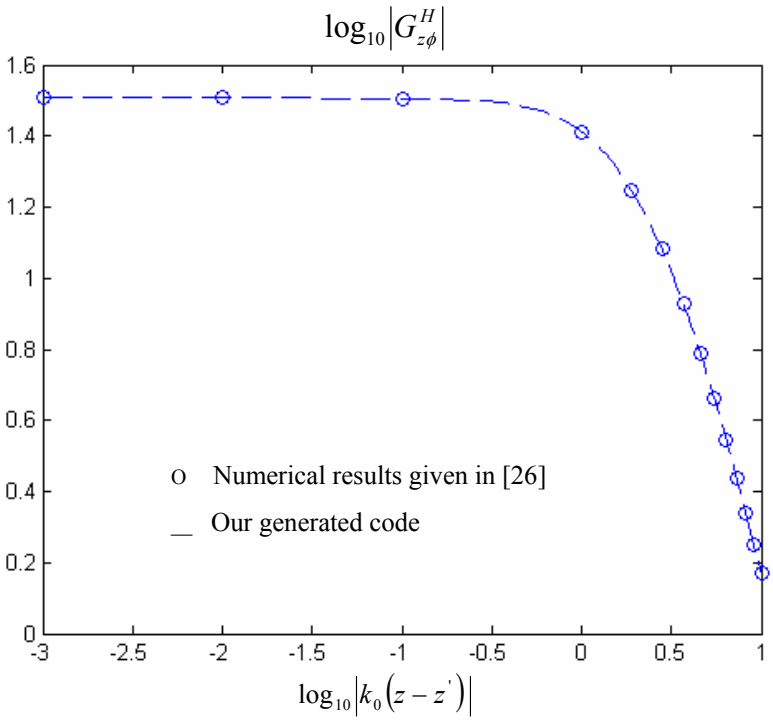

Figure III.5 $\log_{10}\left|G_{z\phi}^{H}\right|$ for an electric dipole pointing in ϕ direction, for the geometry shown in Figure III.2 (N_1=5, N_2=5, N_3=1, T_1=0.1, T_2=3.5, T_3=4).

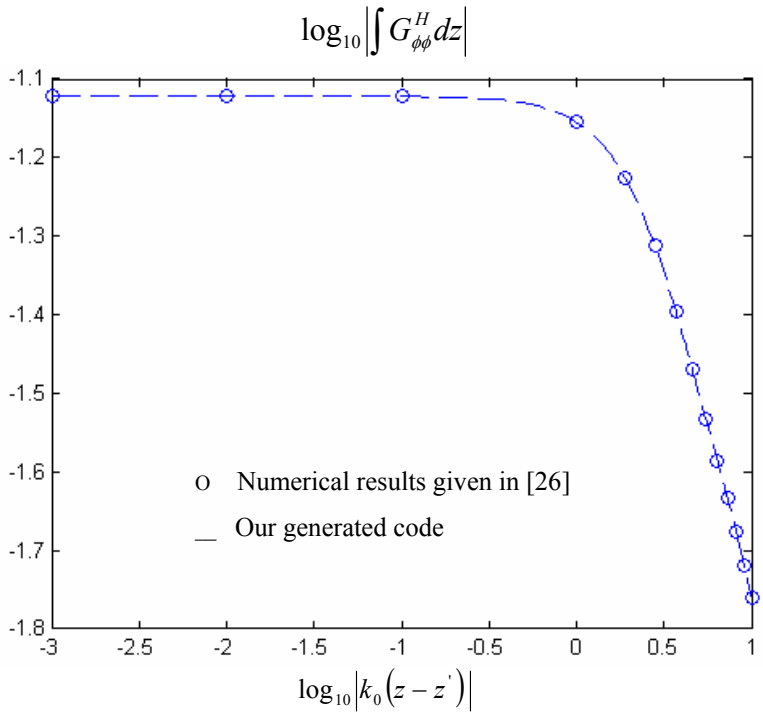

Figure III.6 $\log_{10}\left|\int G^H_{\phi\phi} dz\right|$ for an electric dipole pointing in ϕ direction, for the geometry shown in Figure III.2 (N_1=4, N_2=4, N_3=1, T_1=0.1, T_2=3, T_3=3.5).

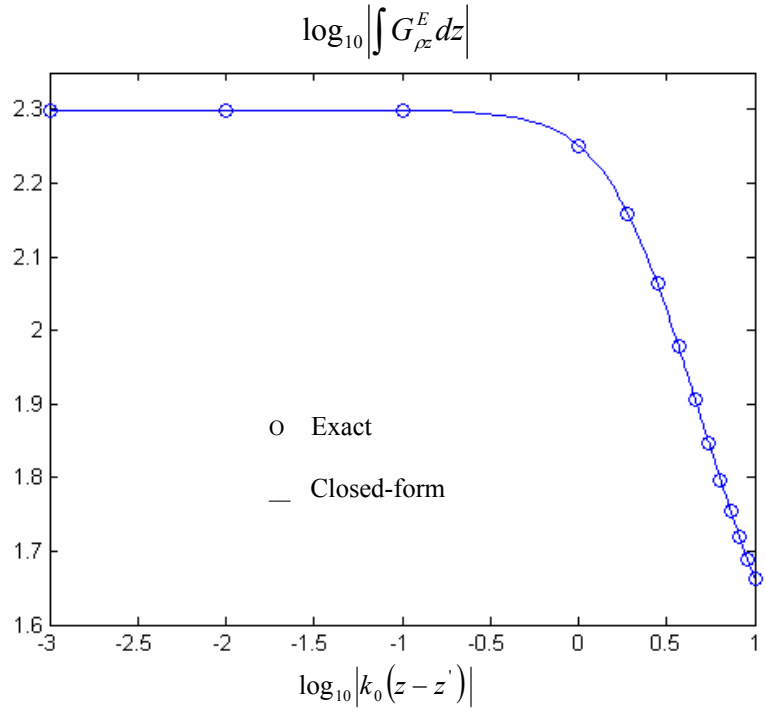

Figure III.7 $\log_{10}\left|\int G^E_{\rho z} dz\right|$ for an electric dipole pointing in *z* direction, for the geometry shown in Figure III.2 (N_1=4, N_2=4, N_3=1, T_1=0.1, T_2=3, T_3=3.5).

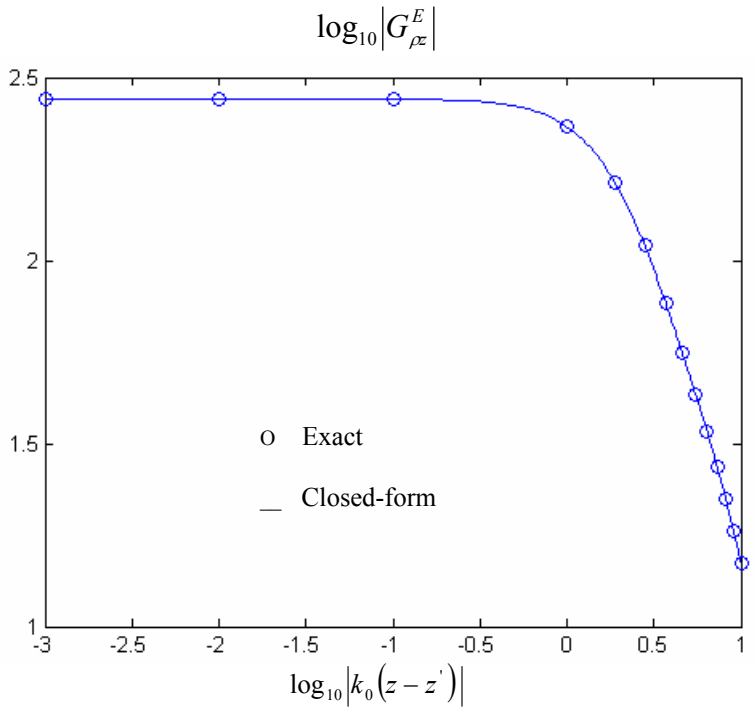

Figure III.8 $\log_{10}\left|G^E_{\rho z}\right|$ for a magnetic dipole pointing in *z* direction, for the geometry shown in Figure III.2 (N_1=4, N_2=4, N_3=1, T_1=0.1, T_2=3, T_3=3.5).

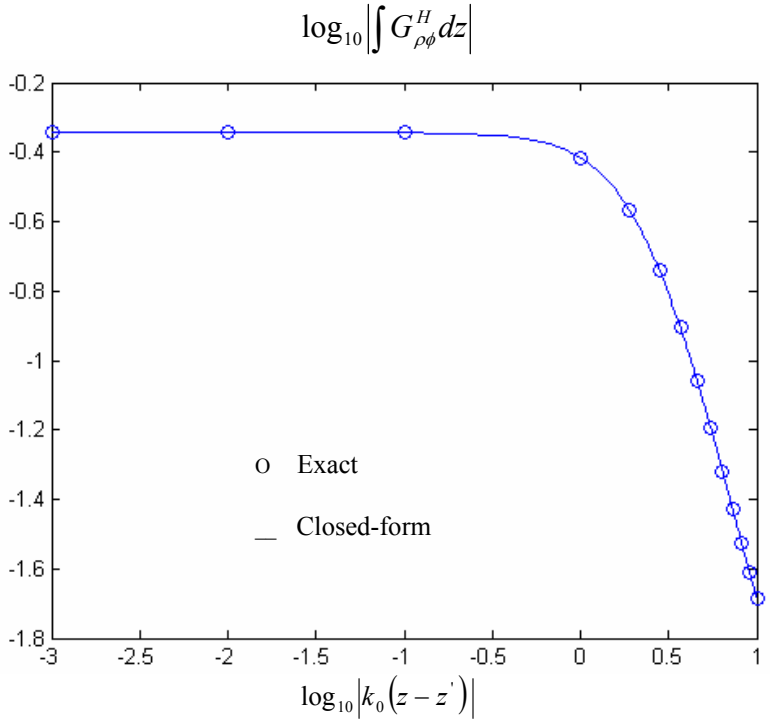

Figure III.9 $\log_{10}\left|\int G^H_{\rho\phi}dz\right|$ for an electric dipole pointing in ϕ direction, for the geometry shown in Figure III.2 (N_1=4, N_2=4, N_3=1, T_1=0.1, T_2=3, T_3=3.5).

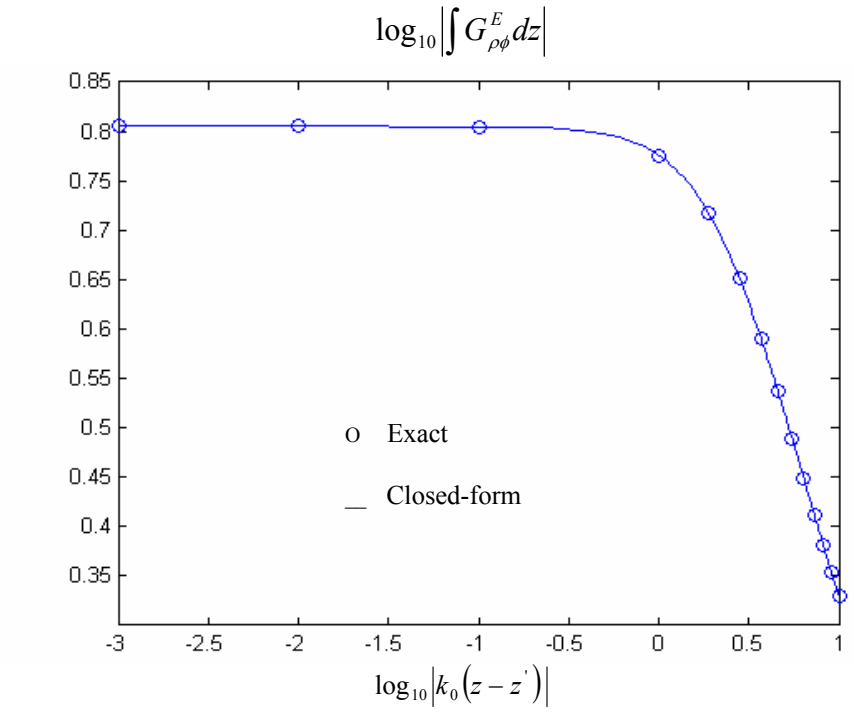

Figure III.10 $\log_{10}\left|\int G^E_{\rho\phi}dz\right|$ for a magnetic dipole pointing in ϕ direction, for the geometry shown in Figure III.2 (N_1=4, N_2=4, N_3=1, T_1=0.1, T_2=3, T_3=3.5).

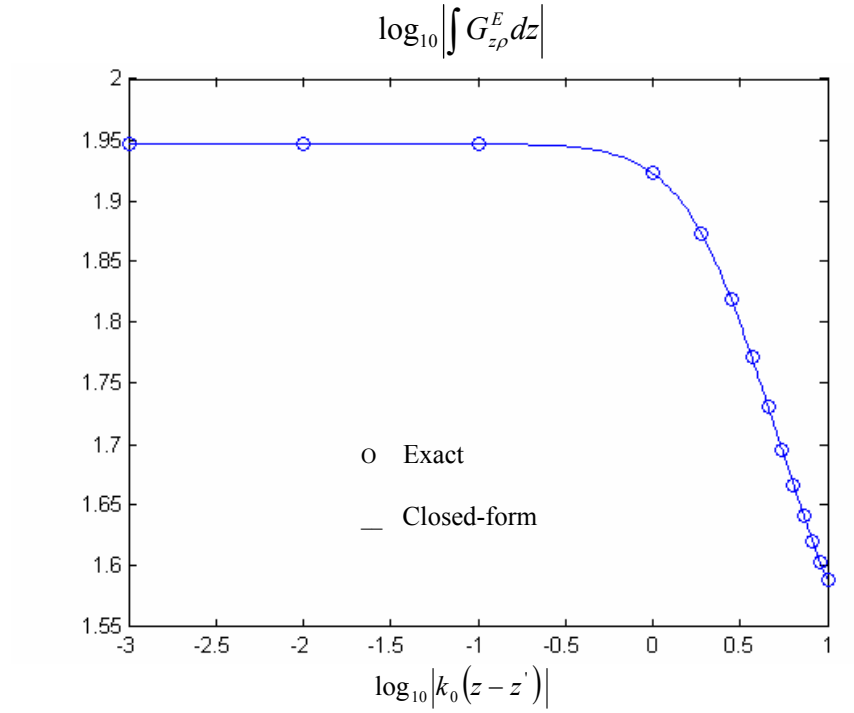

Figure III.11 $\log_{10}\left|\int G^E_{z\rho}dz\right|$ for an electric dipole pointing in ρ direction, for the geometry shown in Figure III.2 (N_1=5, N_2=4, N_3=1, T_1=0.1, T_2=3, T_3=3.5).

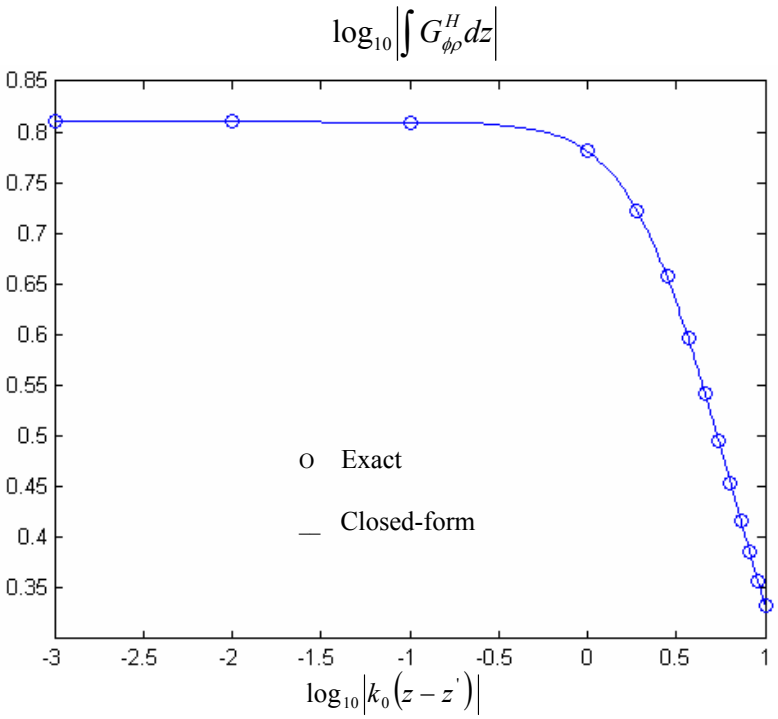

Figure III.12 $\log_{10}\left|\int G^H_{\phi\rho}dz\right|$ for an electric dipole pointing in ρ direction, for the geometry shown in Figure III.2 (N_1=5, N_2=4, N_3=1, T_1=0.1, T_2=3, T_3=3.5).

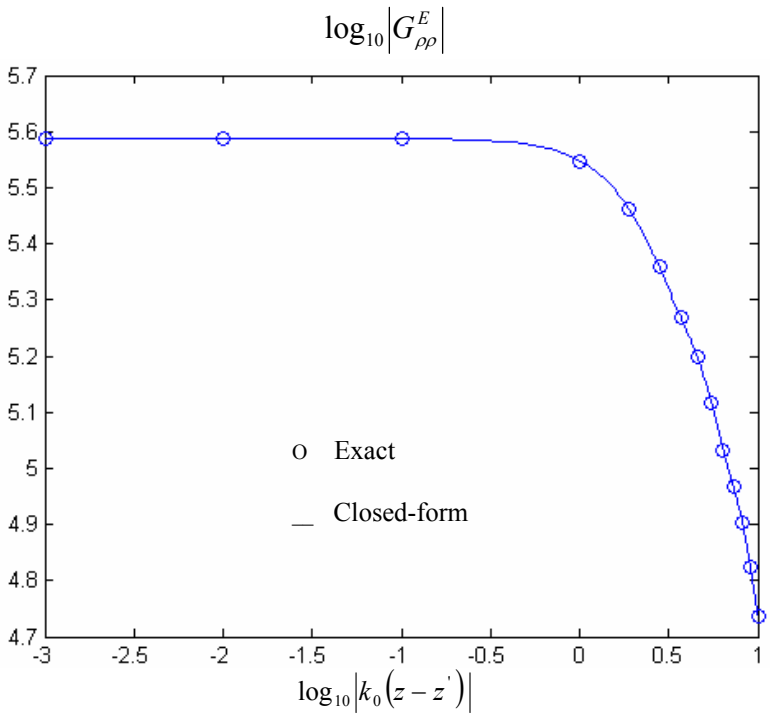

Figure III.13 $\log_{10}\left|G^E_{\rho\rho}\right|$ for an electric dipole pointing in ρ direction, for the geometry shown in Figure III.2 (N_1=5, N_2=4, N_3=1, T_1=0.1, T_2=3, T_3=3.5).

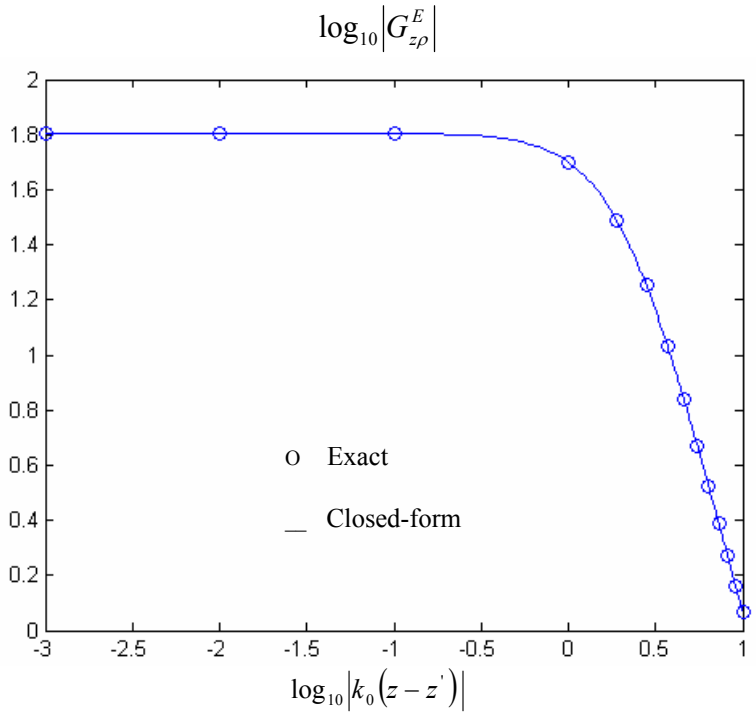

Figure III.14 $\log_{10}\left|G^E_{z\rho}\right|$ for a magnetic dipole pointing in ρ direction, for the geometry shown in Figure III.2 (N_1=5, N_2=4, N_3=1, T_1=0.1, T_2=3, T_3=3.5).

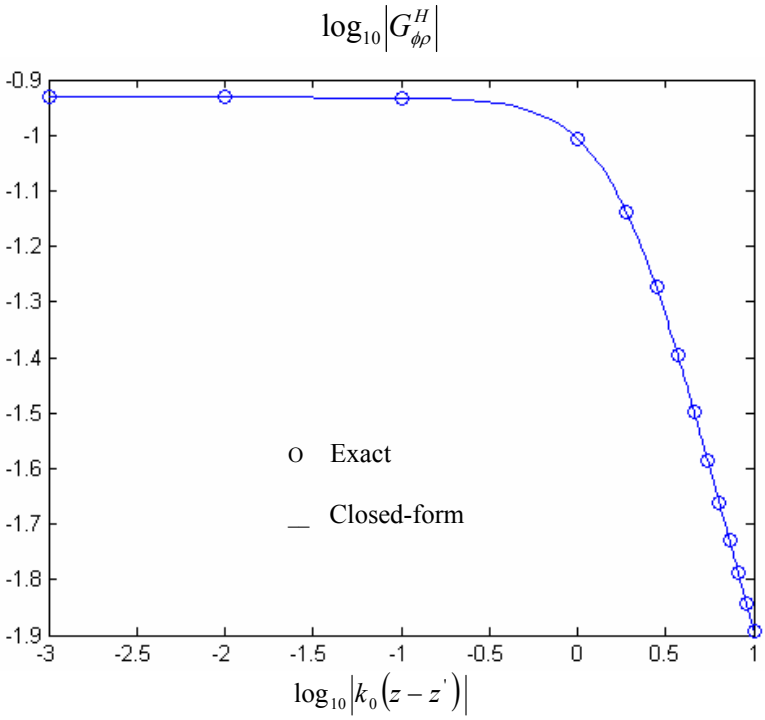

Figure III.15 $\log_{10}\left|G^H_{\phi\rho}\right|$ for a magnetic dipole pointing in ρ direction, for the geometry shown in Figure III.2 (N_1=5, N_2=4, N_3=1, T_1=0.1, T_2=3, T_3=3.5).

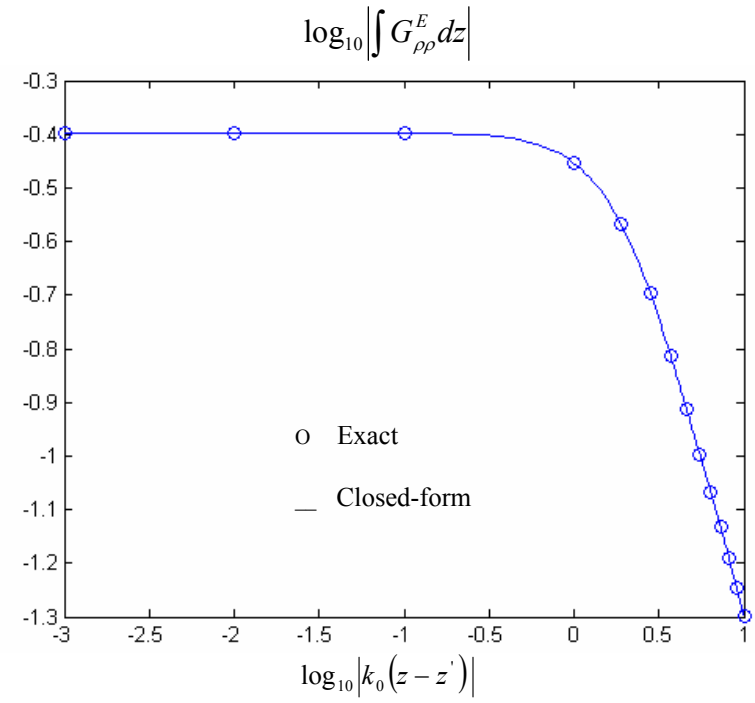

Figure III.16 $\log_{10}\left|\int G^E_{\rho\rho} dz\right|$ for a magnetic dipole pointing in ρ direction, for the geometry shown in Figure III.2 (N_1=5, N_2=4, N_3=1, T_1=0.1, T_2=3, T_3=3.5).

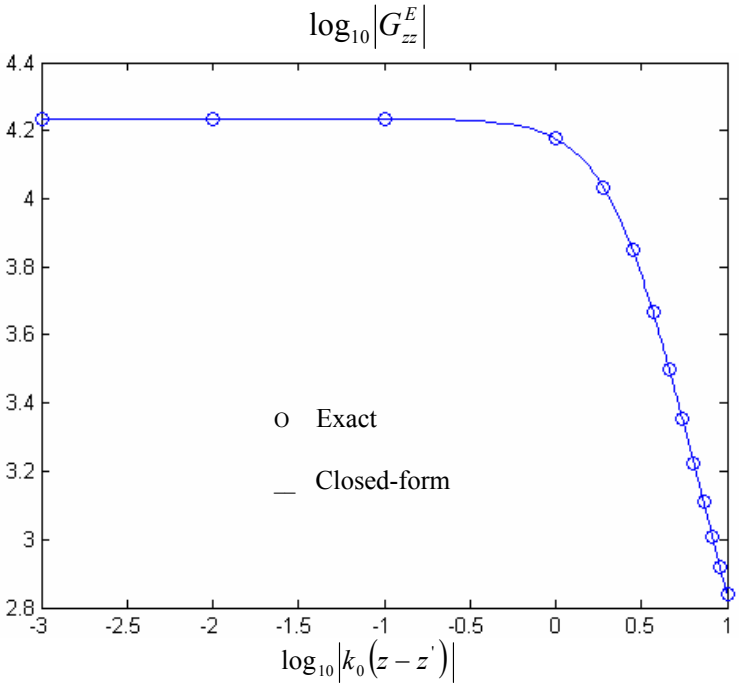

Figure III.17 $\log_{10}\left|G^E_{zz}\right|$ for an electric dipole pointing in z direction, for the geometry shown in Figure III.2 (N_1=4, N_2=5, N_3=1, T_1=0.1, T_2=4.5, T_3=5) when the dielectric is lossy $\varepsilon_{r_1} = 2.3 - j\,0.1$.

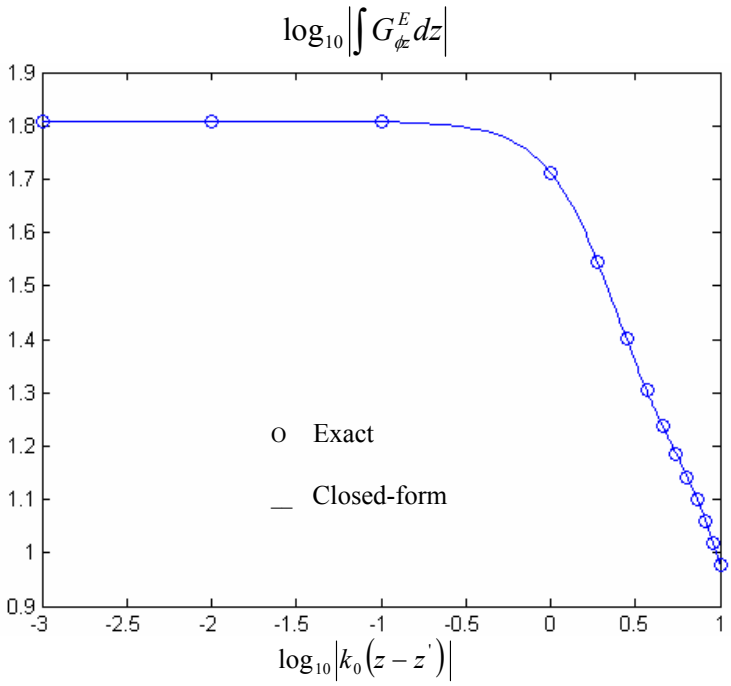

Figure III.18 $\log_{10}\left|\int G_{\phi z}^{E} dz\right|$ for an electric dipole pointing in z direction, for the geometry shown in Figure III.2 (N_1=5, N_2=5, N_3=1, T_1=0.1, T_2=3.5, T_3=4) when the dielectric is lossy $\varepsilon_{r_1} = 2.3 - j\,0.1$.

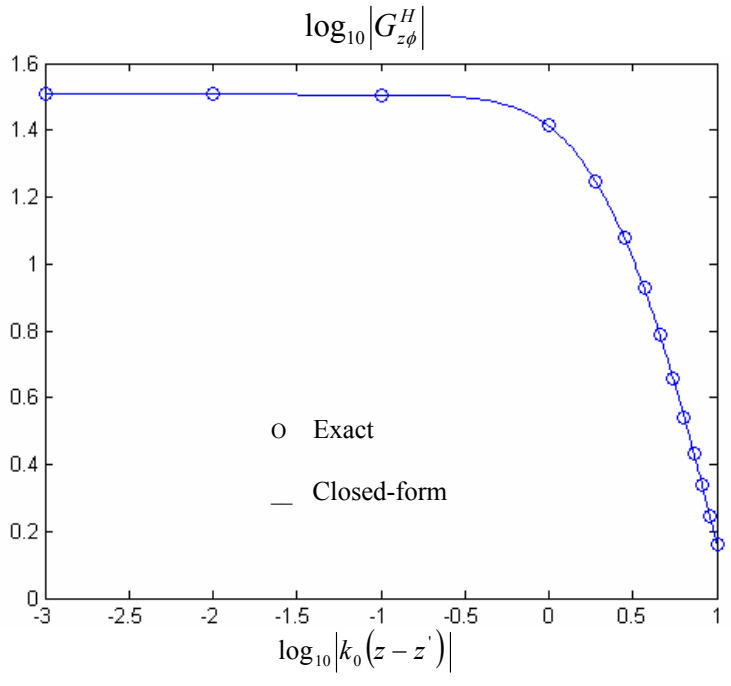

Figure III.19 $\log_{10}\left|G_{z\phi}^{H}\right|$ for an electric dipole pointing in ϕ direction, for the geometry shown in Figure III.2 (N_1=5, N_2=5, N_3=1, T_1=0.1, T_2=3.5, T_3=4) when the dielectric is lossy $\varepsilon_{r_1} = 2.3 - j\,0.1$.

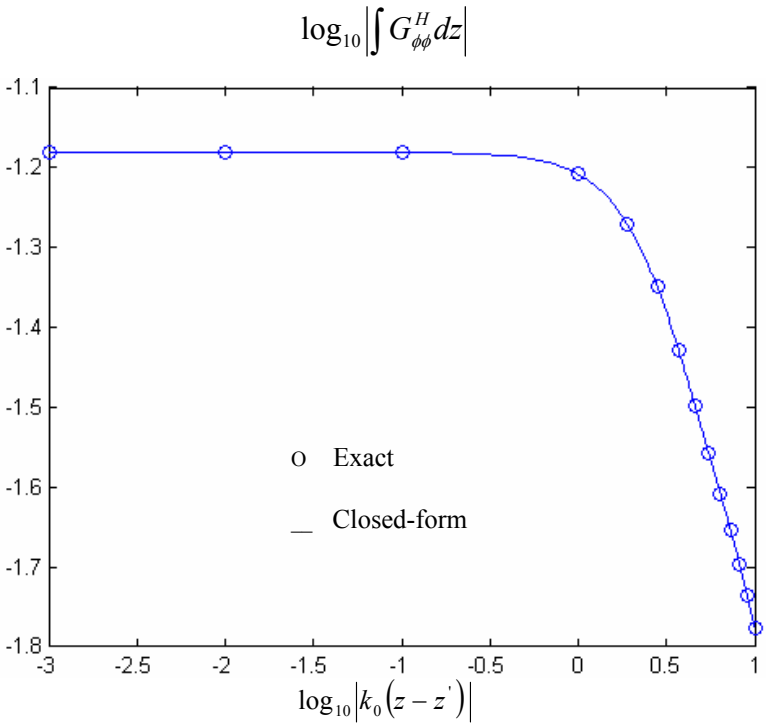

Figure III.20 $\log_{10}\left|\int G_{\phi\phi}^{H} dz\right|$ for an electric dipole pointing in ϕ direction, for the geometry shown in Figure III.2 (N_1=4, N_2=4, N_3=1, T_1=0.1, T_2=3, T_3=3.5) when the dielectric is lossy $\varepsilon_{r_1} = 2.3 - j\,0.1$.

III.4.2 Closed-form Green's Function Results for $\rho = \rho'$

The closed-form Green's functions when $\rho = \rho'$ are evaluated using the procedure given in Section III.3.

The closed-form Green's functions are calculated for the geometry shown in Figure III.2. Both the electric point source and the observation point are located at the air-dielectric interface such that $\rho = \rho' = a_1$=21mm. The results are given for different $(\phi - \phi')$ values and compared with the exact ones in Figure III.21-Figure III.23. In our simulations, at most 110-120 eigenmodes are needed.

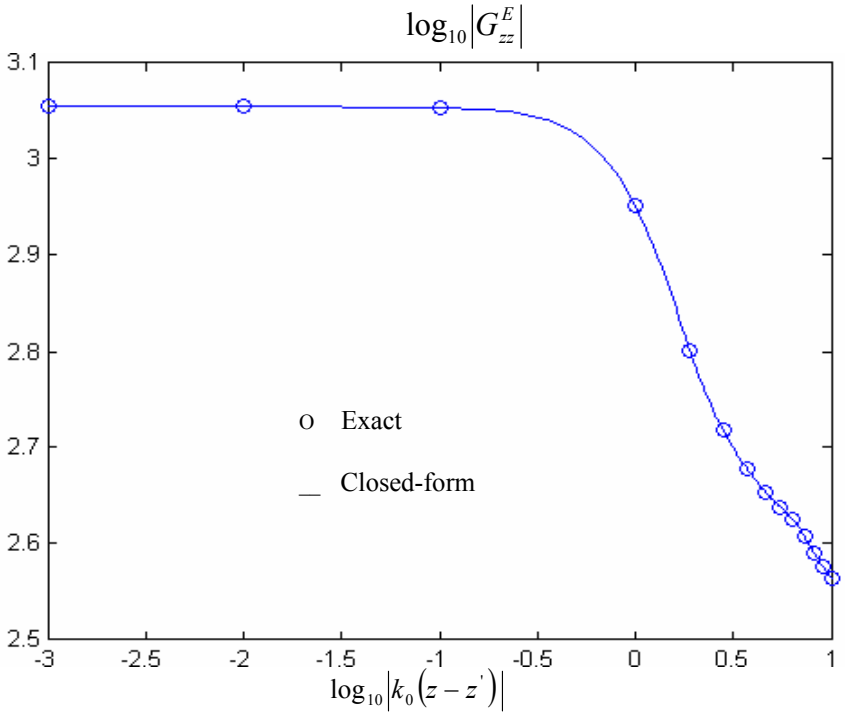

Figure III.21. $\log_{10}\left|G_{zz}^{E}\right|$ for an electric dipole pointing in *z* direction, for the geometry shown in Figure III.2, ρ = ρ'=21mm, $\phi-\phi'=60°$.

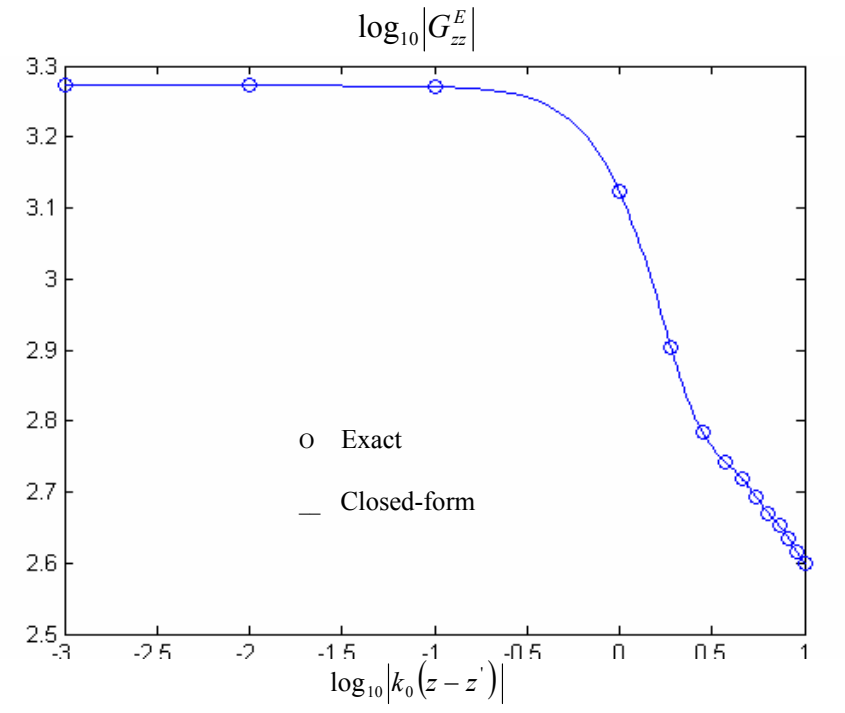

Figure III.22 $\log_{10}\left|G_{zz}^{E}\right|$ for an electric dipole pointing in *z* direction, for the geometry shown in Figure III.2, ρ = ρ'=21mm, $\phi-\phi'=50°$.

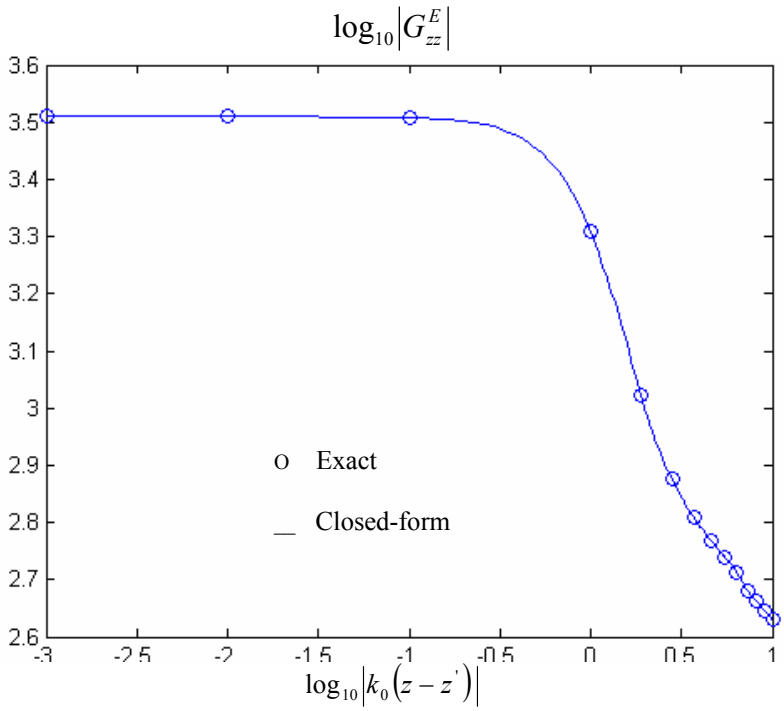

Figure III.23 $\log_{10}|G_{zz}^{E}|$ for an electric dipole pointing in *z* direction, for the geometry shown in Figure III.2, ρ = ρ'=21mm, $\phi-\phi'=40°$.

The exact and the closed-form Green's function of G_{zz}^{E} for an electric point source are plotted together when f =6.8 GHz and $\varepsilon_{r_1}=10$ for various $(\phi-\phi')$ values and they are found to be in good agreement as seen in Figure III.24-Figure III.27.

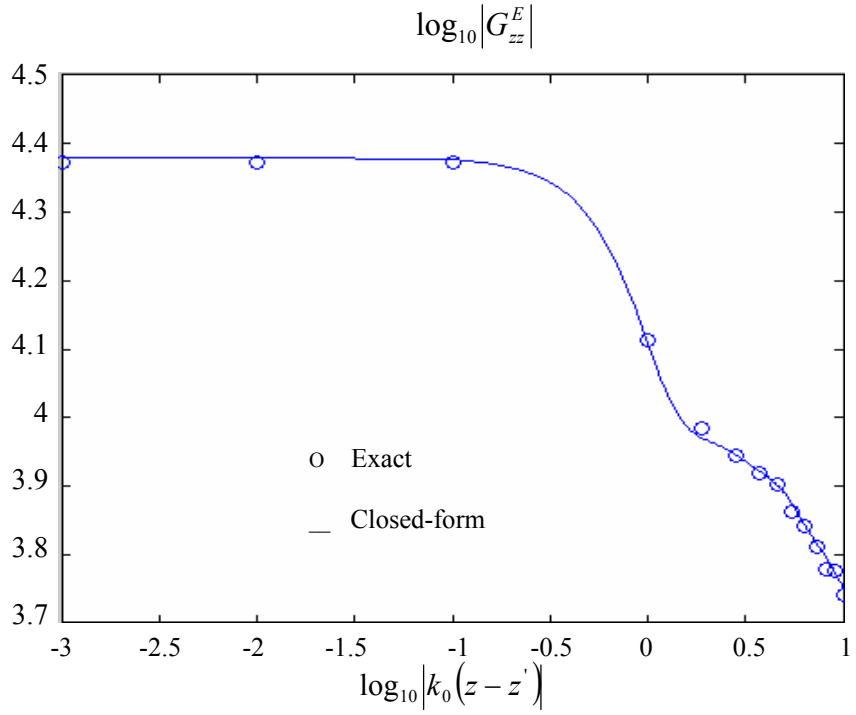

Figure III.24 $\log_{10}|G_{zz}^{E}|$ for an electric dipole pointing in *z* direction, for the geometry shown in Figure III.2, ρ = ρ'=21mm, $\phi - \phi' = 30°$.

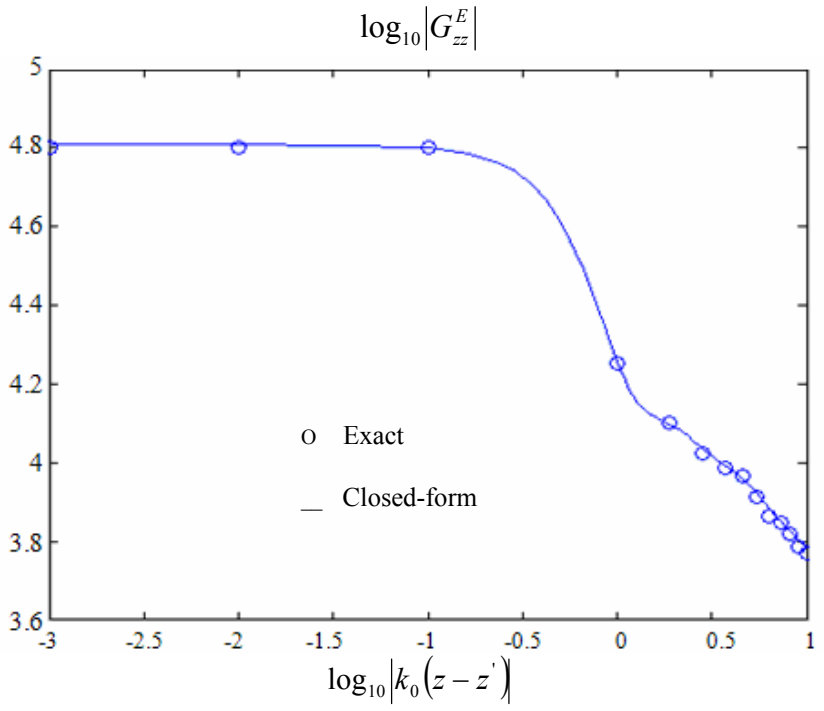

Figure III.25 $\log_{10}|G_{zz}^{E}|$ for an electric dipole pointing in *z* direction, for the geometry shown in Figure III.2, ρ = ρ'=21mm, $\phi - \phi' = 20°$.

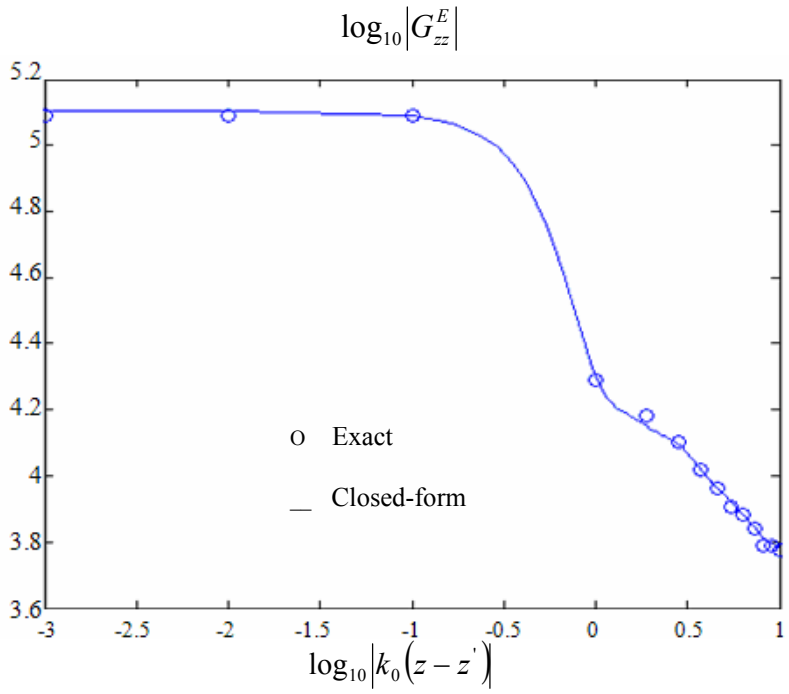

Figure III.26 $\log_{10}|G_{zz}^{E}|$ for an electric dipole pointing in *z* direction, for the geometry shown in Figure III.2, ρ = ρ'=21mm, $\phi - \phi' = 15°$.

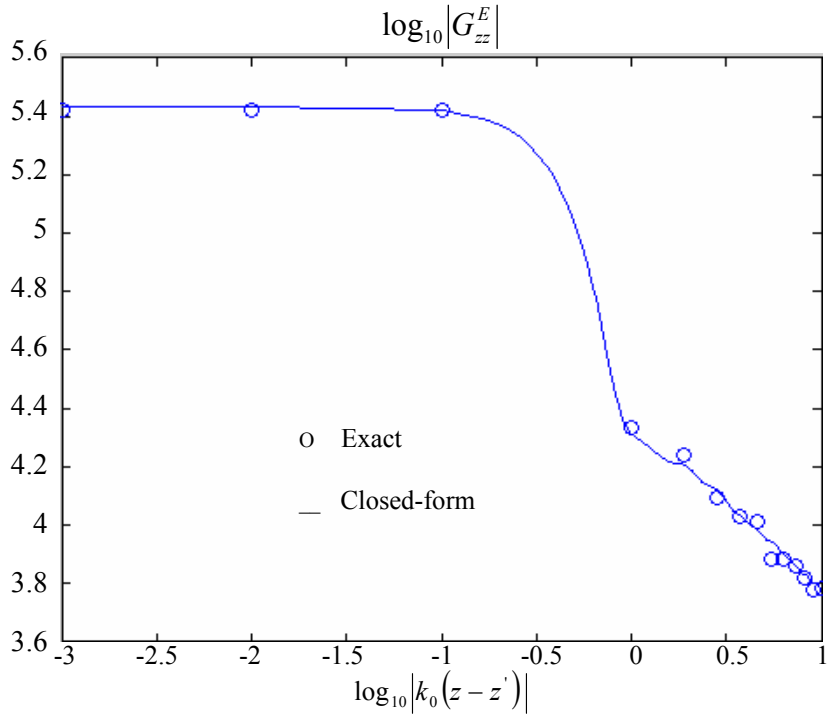

Figure III.27 $\log_{10}|G_{zz}^{E}|$ for an electric dipole pointing in *z* direction, for the geometry shown in Figure III.2, ρ = ρ'=21mm, $\phi - \phi' = 10°$.

For the geometry shown in Figure III.2, the spatial-domain Green's function of different components due to different source types are given when $\rho = \rho^{'}$ for various dielectric constants ε_{r_1}, frequency f and $(\phi - \phi')$ values as seen in Figure III.28-Figure III.33. For lower $(\phi - \phi')$ values, numerical difficulties start to appear.

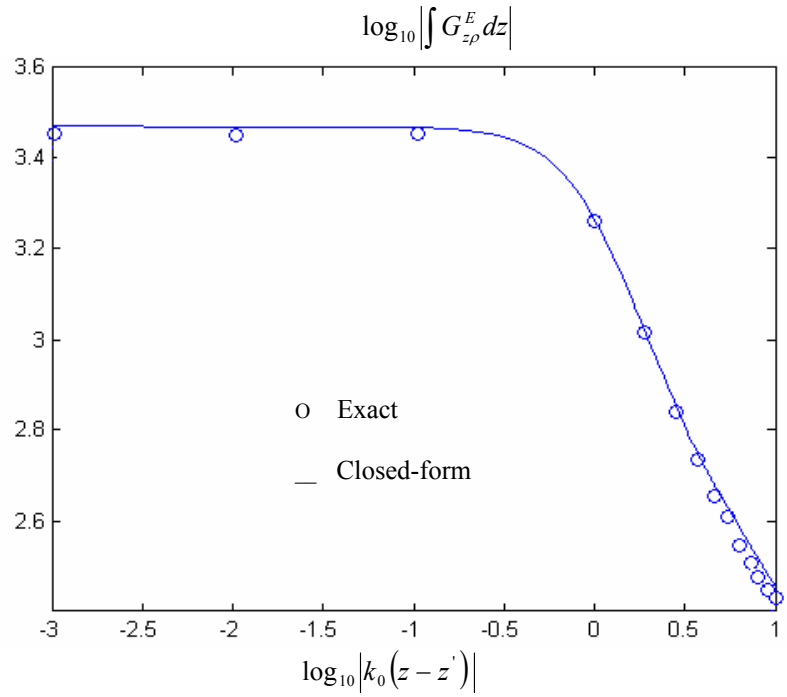

Figure III.28. $\log_{10}\left|\int G_{z\rho}^{E} dz\right|$ for an electric dipole pointing in ρ direction, for the geometry shown in Figure III.2, ρ = ρ'=21mm, $\phi - \phi'$ = 15°, ε_{r_1} =2.3, f =10GHz.

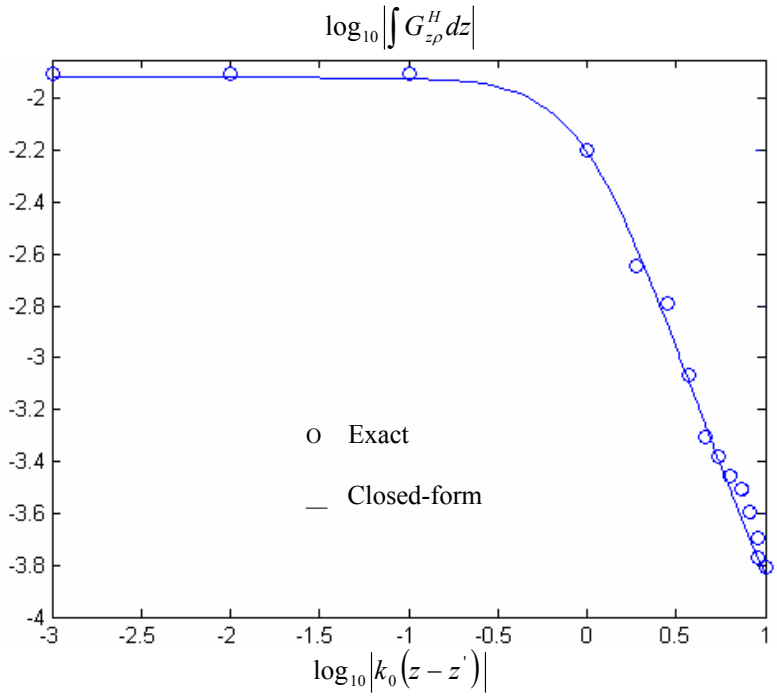

Figure III.29. $\log_{10}\left|\int G_{z\rho}^{H} dz\right|$ for a magnetic dipole pointing in ρ direction, for the geometry shown in Figure III.2, ρ = ρ'=21mm, $\phi - \phi' = 15°$, ε_{r_1} =2.3, f =10GHz.

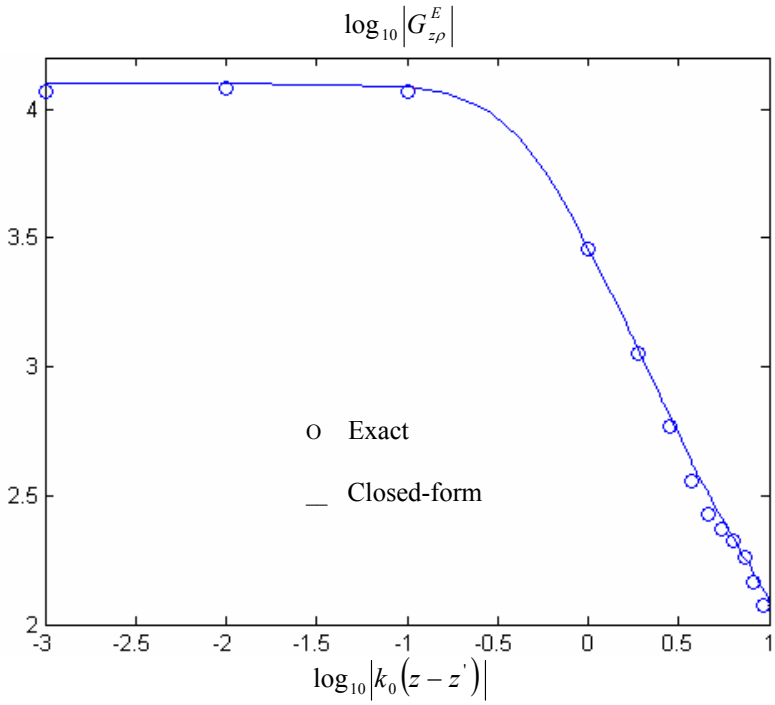

Figure III.30 $\log_{10}\left|G_{z\rho}^{E}\right|$ for a magnetic dipole pointing in ρ direction, for the geometry shown in Figure III.2, ρ = ρ'=21mm, $\phi - \phi' = 10°$, ε_{r_1} =5, f =10GHz.

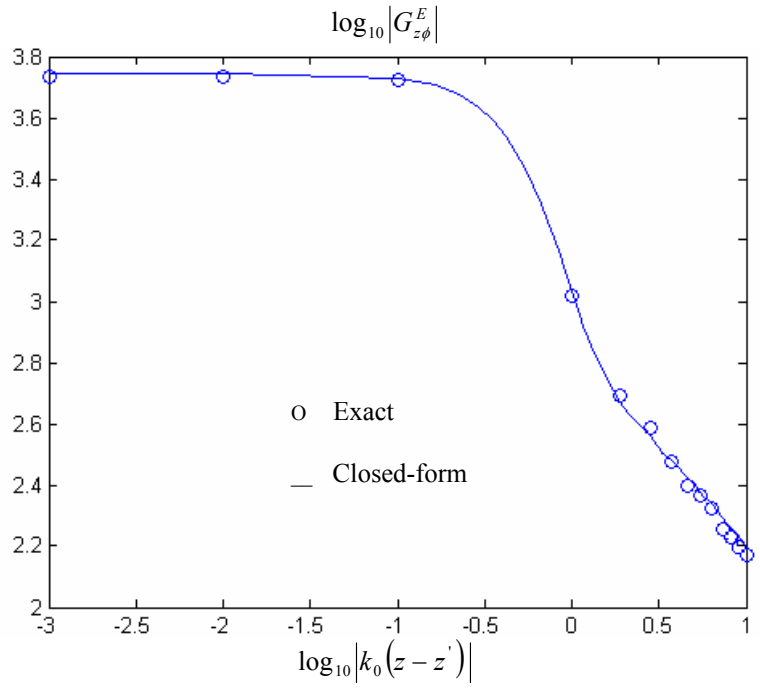

Figure III.31 $\log_{10}\left|G^E_{z\phi}\right|$ for a magnetic dipole pointing in ϕ direction, for the geometry shown in Figure III.2, ρ = ρ'=21mm, $\phi-\phi'$ = 10°, ε_{r_1} =2.3, f=10GHz.

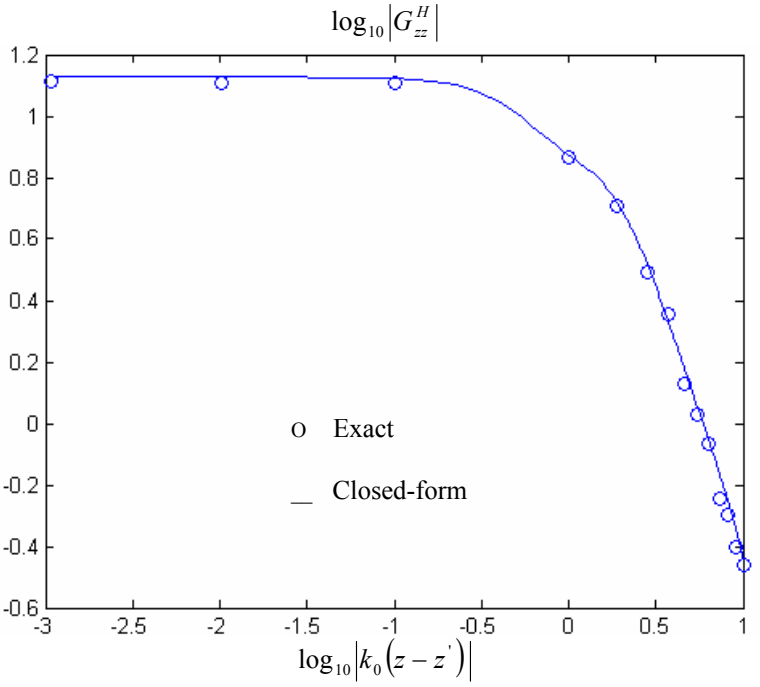

Figure III.32. $\log_{10}\left|G^H_{zz}\right|$ for a magnetic dipole pointing in z direction, for the geometry shown in Figure III.2, ρ = ρ'=21mm, $\phi-\phi'$ = 15°, ε_{r_1} =2.3, f=10GHz.

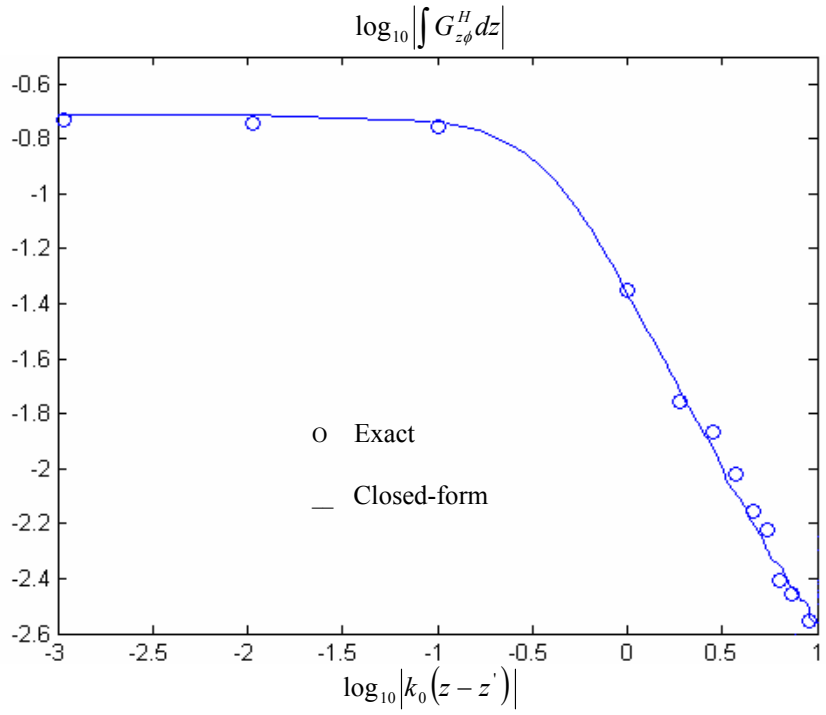

Figure III.33. $\log_{10}\left|\int G_{z\phi}^{H} dz\right|$ for a magnetic dipole pointing in ϕ direction, for the geometry shown in Figure III.2, ρ = ρ'=21mm, $\phi - \phi' = 15°$, $\varepsilon_{r_1} = 5$, $f = 10$GHz.

CHAPTER IV

SURFACE WAVE CONTRIBUTION

IV.1 Introduction

As mentioned in Chapter III, the Sommerfeld path contains a certain number of poles and branch-point singularities [37] which are associated with surface and leaky waves launched by the source. Among these, the surface waves play a rather significant role since they are guided along the interface without leaking energy.

In *planar layered medium*, a number of studies have been reported about the contribution of surface waves in the literature.

A. K. Bhattacharyya in his work [38], important characteristics of the surface wave modes in a planar multilayered grounded dielectric substrate are explored. It is shown how these characteristics can be utilized to determine the surface wave fields of an arbitrary shaped source. It is also stated that the study may find application for millimeter-wave printed antennas where the surface wave play an important role in determining the radiation and the impedance characteristics.

In *planar layered medium*, the surface wave pole singularities are located on the real axis of the k_ρ-plane. Even if Sommerfeld integration path is deformed such that it is not too close to the surface wave pole singularities, their presence still affects the value of the integral for small values of k_ρ. Hence, it may be helpful to extract these surface wave pole singularities from the integrand before employing GPOF, since it helps smooth the integrand and makes it easy to approximate by GPOF. It has been shown in [39], [40] that if the surface wave poles are not extracted prior to exponential fitting (GPOF) DCIM approximation seems to deteriorate violently, even for moderate distances from the source. Hence, knowing that the surface wave contribution approaches its theoretical limit ($1/\sqrt{\rho}$), even for moderate distances from the source, it is obvious that for

such cases, if these poles are not extracted and represented interms of complex exponentials, the discrete complex images are not sufficient, since they exhibit exponential decay ($1/\rho$).

I. Aksun and G. Dural in their work [40] give a brief of the development of the closed-form Green's functions for *planarly layered medium*. The closed-form Green's functions which are derived for the vector and scalar potentials using DCIM for planarly layered media are revisited to clarify some issues and misunderstandings on the use of DCIM. Among these issues, it is shown that the deviations of the approximations of the Green's function start at the distances where the spherical wave approximations of the surface wave pole contribution deviate from the exact surface wave contribution. It is also suggested to subtract the surface wave poles from the spectral-domain Green's functions before the approximation (GPOF), and to add their contribution analytically after GPOF.

In *cylindrical layered medium*, A. Y. Svezhentsev and G. A. E. Vandenbosch dealed with the contribution of surface wave poles. In their research [41], they used mixed-potential Green's functions for the printed elements over metal-dielectric cylindrical structure. While trying to calculate directly IFT (Inverse Fourier Transform) of spectral-domain Green's function in their work, they faced with singular behaviours of spectral-domain Green's functions one of which is the surface wave poles. Using Newton-Raphson method they found these surface wave poles which make the spectral domain Green's functions go to infinity and then extracted them before calculating Sommerfeld integral.

A. Y. Svezhentsev in his own work [42] dealing with *cylindrical layered medium*, takes a step further and seeks to recognize the leaky wave contributions in the case when the cylinder is electrically large and the source is widely separated from the observation point, even though stating that this approach has some restrictions. In this work it is stated that at a fixed frequency there is always an infinite number of leaky waves of which have non zero imaginary component in their propagation constants, therefore the leaky waves decay exponentially as the distance between the source and the observation points increases.

IV.2 Surface Wave Poles

The surface wave poles exist symmetrically in the interval $k_z \in (k_0, k_0\sqrt{\varepsilon_{r\max}})$ and $k_z \in (-k_0, -k_0\sqrt{\varepsilon_{r\max}})$ in the positive and negative parts of the real k_z axis, respectively, seen in Figure IV.1 if loss is absent. k_0 is the wave number of free space, k_s is the wave number of the source layer which is selected as k_0 in our analysis.

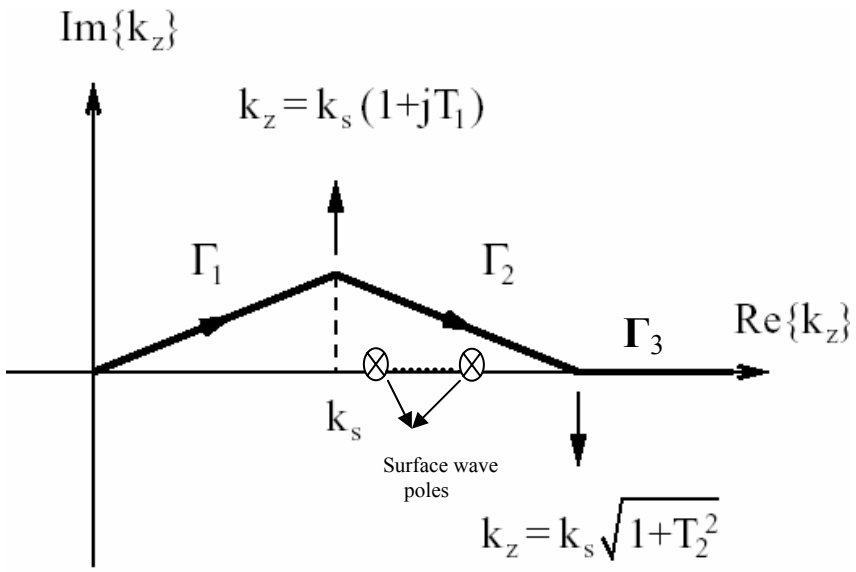

Figure IV.1 Location of the surface wave poles

The number and the location of the surface wave poles is dependent on the radius a_1, the wave number k_0 (frequency of operation), the dielectric constant ε_{r_1} of the dielectric layer, the thickness t_h of the dielectric layer involved.

IV.3 Finding the Location of Surface Wave Poles

The location of the surface wave poles in the spectral domain can be found by finding the roots of the denominator of the spectral domain Green's functions.

To find the roots of a function, two different kinds of methods called bracketing and open are used in the literature which are Newton-Raphson method, Bisection method, Secant method, False-Position Method, Ragula Falsi method.

Methods such as Bisection method, Ragula Falsi method and the False-Position method of finding roots of a nonlinear equation *f(x)=0* require bracketing of the root by two guesses. Such methods are called bracketing methods. These methods are always convergent since they are based on reducing the interval between the two guesses to *zero* on the root.

Perhaps the most widely used root-finding method is the Newton-Raphson method which is also used in our analysis (given in Appendix D). In the Newton-Raphson method, the root is not bracketed. Only one initial guess of the root is needed to get the iterative process started to find the root of an equation. Hence, the method falls in the category of open methods as Secant method.

Although the Newton-Raphson method is often very efficient, its convergence depends on the nature of the function and on the accuracy of the initial guess. The only solution is to have an initial guess that is "sufficiently" close to the root. This is the reason why a *two-stage procedure* is applied to find the roots of the denominator of the spectral domain Green's function $\widetilde{G}$ while using the Newton-Raphson method. Because of the discontinuous behaviour of spectral domain Green's function $\widetilde{G}$, it may not converge if the starting point is not selected as close to a root. That may cause the program to fail or cause too many iterations before exceeding the preset maximum number of iterations. Hence, the *golden search procedure* is used in conjunction with Newton-Raphson method. On the other hand, the golden search procedure is very robust to locate the minima. Therefore, the two-stage procedure can overcome the difficulty of the Newton-Raphson method.

The algorithm of a *two-stage procedure* can be given as follows:

1. For a given interval on the real axis of k_z plane, the golden search procedure is used to minimize $\left|\widetilde{G}\right|$. A local minimum point is then found.
2. This minimum point is then used as the starting point for a Newton-Raphson procedure for finding the roots of $\widetilde{G}$ denominator.

To find all the roots, the interval between the minimum and maximum wave number of all layers $(k_0, k_0\sqrt{\varepsilon_{r\max}})$ is divided uniformly into number of sections. For each section, the golden search procedure is applied first to find the minimum of $|\widetilde{G}|$, which is used as the starting point for the Newton-Raphson method.

When the surface wave poles are found, since they occur in complex conjugate pairs, they can be represented mathematically as [41]

$$\widetilde{G}_{sw} = \sum_{n=0}^{N}\sum_{m=1}^{M_n} \frac{2\,\mathrm{Re}\,s_n^m\, k_{zn}^m}{k^2{}_z - (k_{zn}^m)^2} \tag{IV.3}$$

where k_{zn}^m is the surface wave pole and $\mathrm{Re}\,s_n^m$ is the residue of the spectral-domain Green's function at that pole. N is the maximum number of n (starting from zero) for surface waves exist for given geometrical parameters and frequency. M_n, that starts from 1, is the full number of surface waves which corresponds to the same value of n.

The residue of the spectral Green's function $\widetilde{G}$ at a surface wave pole k_{zn}^m can be found as

$$\mathrm{Re}\,s_n^m = \lim_{k_z \to k_{zn}^m} (\mathrm{k}_z - k_{zn}^m)\,\widetilde{G} \tag{IV.4}$$

The inverse Fourier transform of (IV.3) is calculated using residue theorem.

Residue Theorem [43]: states that if a function f has only a finite number of singular points interior to some simple closed contour *C*, then the value of the integral of f around *C* is 2πj times the sum of the residues associated with those singular points.

Hence, using the residue theorem the spatial-domain of the surface wave contribution is given as

$$G_{sw} = \frac{1}{2\pi}\int dk_z\, e^{-jk_z(z-z')} \sum_{n=0}^{N}\sum_{m=1}^{M_n} \frac{2\,\mathrm{Re}\,s_n^m\, k_{zn}^m}{k^2{}_z - (k_{zn}^m)^2}\,\tau_n \cos(n(\phi-\phi')) \qquad \tau_n = \begin{cases} 1 & n=0 \\ 2 & n\geq 1 \end{cases}$$

$$= \sum_{n=0}^{N}\sum_{m=1}^{M_n} \tau_n \cos(n(\phi-\phi'))\,(\mathrm{j}\ \mathrm{Re}\,s_n^m)\ \ \mathrm{e}^{-\mathrm{j}k_{zn}^m(z-z')} \qquad \text{(IV.5)}$$

IV.4 Numerical Results

In this section, the surface wave contribution in cylindrically stratified media is investigated. In that investigation, the effect of the surface wave poles and the deformed path are studied. The effect of the deformed path is studied by changing the deformed path parameters. Figure IV.2 is a cylindrically multilayered structure used in our calculations. The innermost layer is perfect electric conductor (PEC), the radius of the cylinder is a_1 and the thickness of the dielectric coating is t_h (hence $a_1 = a_0 + t_h$). Both the point electric source and the observation point are located at the air-dielectric interface such that $\rho' = \rho = a_1$. The observations include different frequency f, the cylinder outer radius a_1, the dielectric constant ε_{r_1}.

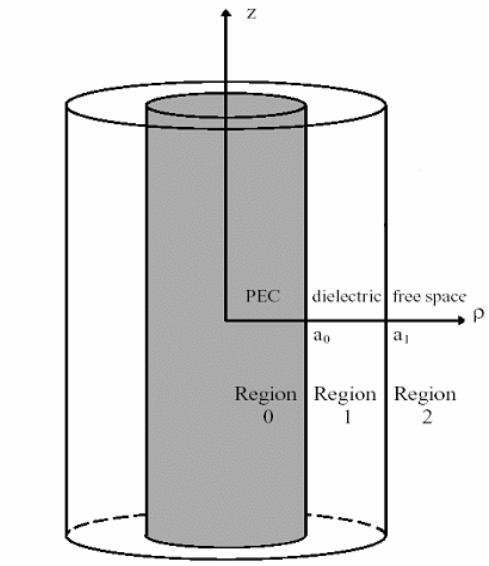

Figure IV.2 Region 0: PEC, Region 1: ε_{r_1}, $\mu_{r_1} = 1$, Region 2: free space, $\rho' = \rho$, ϕ'=0°, ϕ =30°.

Figure IV.3 and Figure IV.4 show the exact and the spatial domain Green's function G_{zz} with and without extraction of surface wave poles when the deformed path parameters are changed such that T_1=0.1, T_2=0.3, T_3=5, when the frequency f=6.8 GHz, the dielectric constant $\varepsilon_{r_1} = 10$, $\rho' = \rho = 0.47\,\lambda_0$, the cylinder outer radius $a_1 = 0.47\,\lambda_0$ and the dielectric thickness $t_h = 0.02\,\lambda_0$ for source and observation point differences $\log_{10}\left|k_0\left(z - z'\right)\right|$ up to 1 and 2.

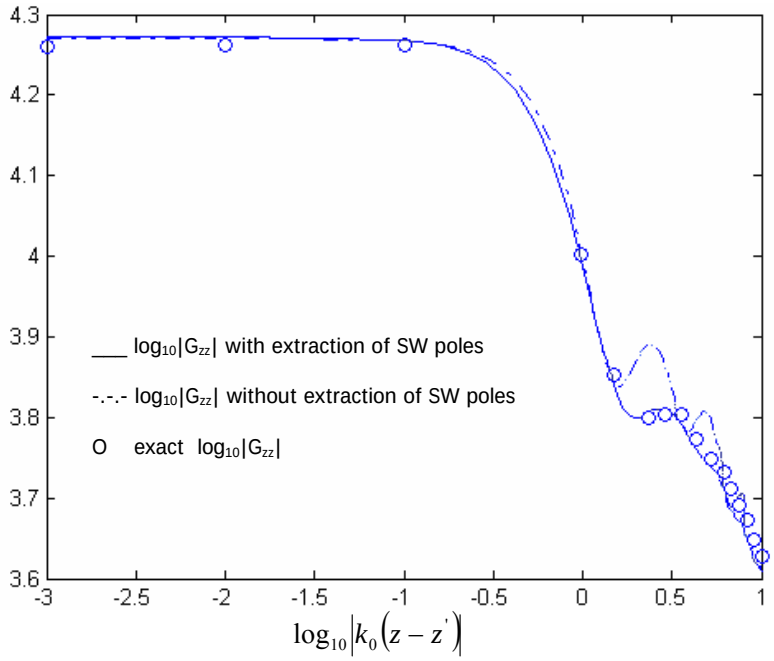

Figure IV.3 The exact and the spatial domain Green's function G_{zz} with and without extraction of surface wave poles for source and observation point difference $\log_{10}\left|k_0\left(z - z'\right)\right|$ up to 1 when the deformed path parameters are changed (T_1=0.1, T_2=0.3, T_3=5), f=6.8GHz, $\varepsilon_{r_1} = 10$, $\rho' = \rho = 0.47\lambda_0$, $a_1 = 0.47\lambda_0$, $t_h = 0.02\lambda_0$.

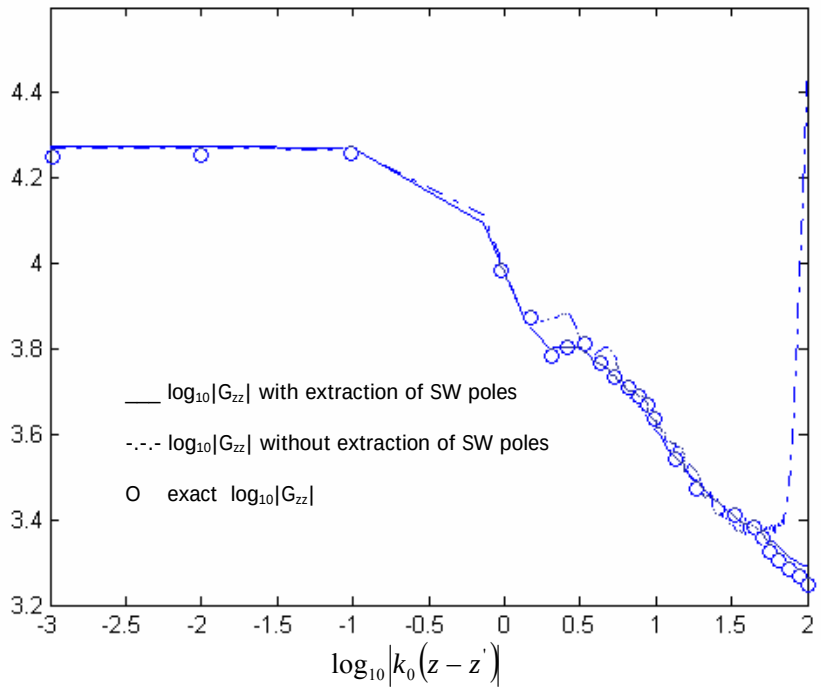

Figure IV.4 The exact and the spatial domain Green's function G_{zz} with and without extraction of surface wave poles for source and observation point difference $\log_{10}|k_0(z-z')|$ up to 2 when the deformed path parameters are changed (T_1=0.1, T_2=0.3, T_3=5), f =6.8GHz, $\varepsilon_{r_1} = 10$, $\rho' = \rho = 0.47\lambda_0$, $a_1 = 0.47\lambda_0$, $t_h = 0.02\lambda_0$.

Figure IV.5 and Figure IV.6 show the spatial domain Green's function G_{zz} with and without extraction of surface wave poles when the deformed path parameters are changed such that T_1=0.1, T_2=0.3, T_3=5, when the frequency f =4.7GHz, the dielectric constant $\varepsilon_{r_1} = 2.3$, $\rho' = \rho = 0.42\ \lambda_0$, the cylinder outer radius $a_1 = 0.42\ \lambda_0$ and the dielectric thickness $t_h = 0.02\ \lambda_0$ for source and observation point differences $\log_{10}|k_0(z-z')|$ up to 1 and 2.

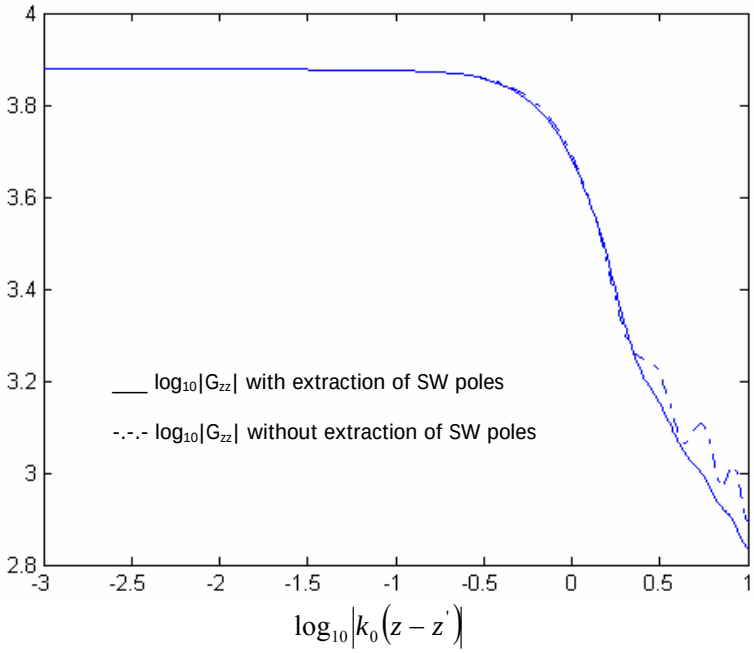

Figure IV.5 The spatial domain Green's function G_{zz} with and without extraction of surface wave poles for source and observation point difference $\log_{10}\left|k_0\left(z-z'\right)\right|$ up to 1 when the deformed path parameters are changed (T_1=0.1, T_2=0.3, T_3=5), f =4.7GHz, $\varepsilon_{r_1}=2.3$, $\rho'=\rho=0.42\lambda_0$, $a_1=0.42\lambda_0$, $t_h=0.02\lambda_0$.

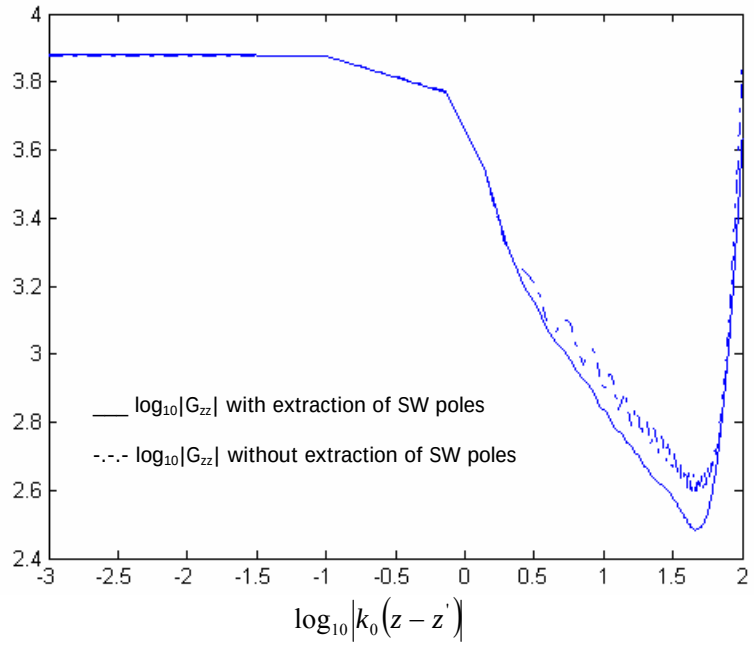

Figure IV.6 The spatial domain Green's function G_{zz} with and without extraction of surface wave poles for source and observation point difference $\log_{10}\left|k_0\left(z-z'\right)\right|$ up to 2 when the deformed path parameters are changed (T_1=0.1, T_2=0.3, T_3=5), f =4.7GHz, $\varepsilon_{r_1}=2.3$, $\rho'=\rho=0.42\lambda_0$, $a_1=0.42\lambda_0$, $t_h=0.02\lambda_0$.

Figure IV.7 and Figure IV.8 show the spatial domain Green's function G_{zz} with and without extraction of surface wave poles when the deformed path parameters are changed such that T_1=0.1, T_2=0.3, T_3=5, when the frequency f =6.8GHz, the dielectric constant $\varepsilon_{r_1} = 10$, $\rho' = \rho = 0.47\ \lambda_0$, the cylinder outer radius a_1= 0.47 λ_0 and the dielectric thickness t_h = 0.02 λ_0 for source and observation point differences $\log_{10}\left|k_0\left(z - z'\right)\right|$ up to 1 and 2.

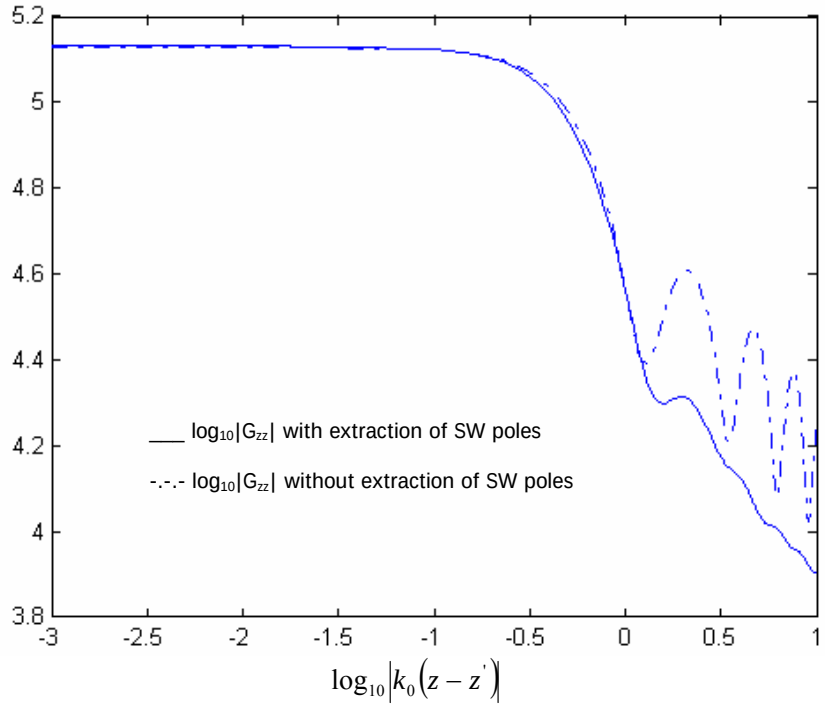

Figure IV.7 The spatial domain Green's function G_{zz} with and without extraction of surface wave poles for source and observation point difference $\log_{10}\left|k_0\left(z - z'\right)\right|$ up to 1 when the deformed path parameters are changed (T_1=0.1, T_2=0.3, T_3=5), f =4.7GHz, $\varepsilon_{r_1} = 10$, $\rho' = \rho$ = 0.24λ_0, a_1= 0.24λ_0, t_h =0.04λ_0.

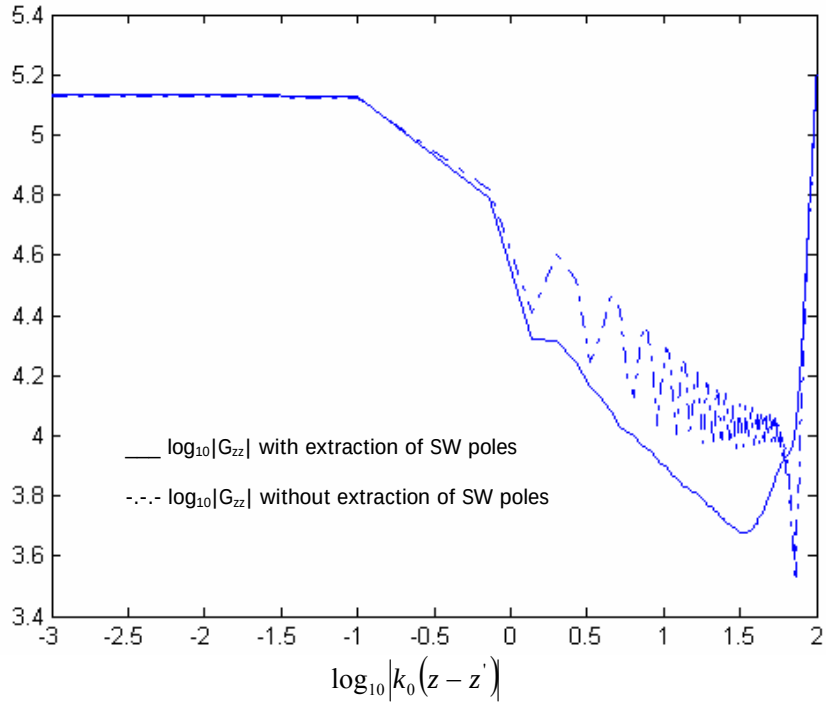

Figure IV.8 The spatial domain Green's function G_{zz} with and without extraction of surface wave poles for source and observation point difference $\log_{10}|k_0(z-z')|$ up to 2 when the deformed path parameters are changed (T_1=0.1, T_2=0.3, T_3=5), f =4.7GHz, $\varepsilon_{r_1} = 10$, $\rho' = \rho$ = $0.24\lambda_0$, $a_1 = 0.24\lambda_0$, $t_h = 0.04\lambda_0$.

When the deformed path parameters are changed such that the deformed path passes close to the surface wave poles, it is observed from the given figures that the spectral Green's functions hence the spatial domain Green's functions deteriorate. This deterioration is overcome by extracting the surface wave poles from the spectral domain Green's functions and adding their contributions in the spatial domain.

Figure IV.9 shows the exact and the spatial domain Green's function G_{zz} without extraction of surface wave poles when the proper deformed path (T_1=0.1, T_2=4.5, T_3=5) is used, when the frequency f =6.8GHz, the dielectric constant $\varepsilon_{r_1} = 10$, $\rho' = \rho$ = 0.47 λ_0, the cylinder outer radius $a_1 = 0.47\ \lambda_0$ and the dielectric thickness $t_h = 0.02\ \lambda_0$ for source and observation point difference $\log_{10}|k_0(z-z')|$ up to 2.

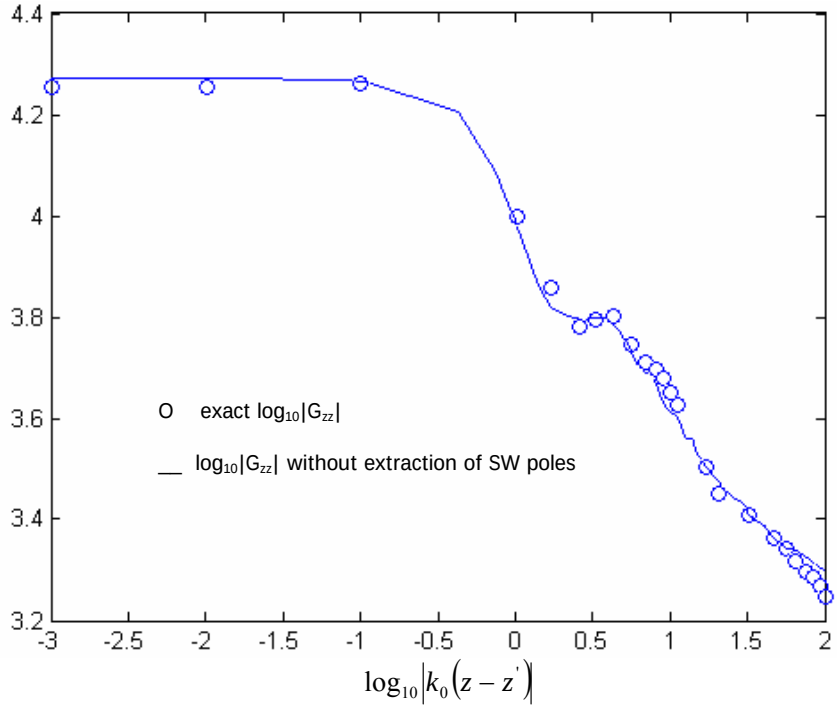

Figure IV.9 The exact and the spatial domain Green's function G_{zz} without extraction of surface wave poles, f=6.8GHz, $\varepsilon_{r_1} = 10$, $\rho' = \rho = 0.47\lambda_0$, $a_1 = 0.47\lambda_0$, $t_h = 0.02\lambda_0$.

Figure IV.10 shows the exact and the spatial-domain Green's function G_{zz} without extraction of surface wave poles when the proper deformed path (T_1=0.1, T_2=3.5, T_3=4) is used, when the frequency f =4.7GHz, the dielectric constant $\varepsilon_{r_1} = 2.3$, $\rho' = \rho = 0.42\ \lambda_0$, the cylinder outer radius $a_1 = 0.42\ \lambda_0$ and the dielectric thickness $t_h = 0.02\ \lambda_0$ for source and observation point difference $\log_{10}\left|k_0(z - z')\right|$ up to 2.

Figure IV.11 shows the exact and the spatial domain Green's function G_{zz} without extraction of surface wave poles when the proper deformed path (T_1=0.1, T_2=3.5, T_3=4) is used, when the frequency f =4.7 GHz, the dielectric constant $\varepsilon_{r_1} = 2.3$, $\rho' = \rho = 0.34\ \lambda_0$, the cylinder outer radius $a_1 = 0.34\ \lambda_0$ and the dielectric thickness $t_h = 0.04\ \lambda_0$ for source and observation point difference $\log_{10}\left|k_0(z - z')\right|$ up to 2.

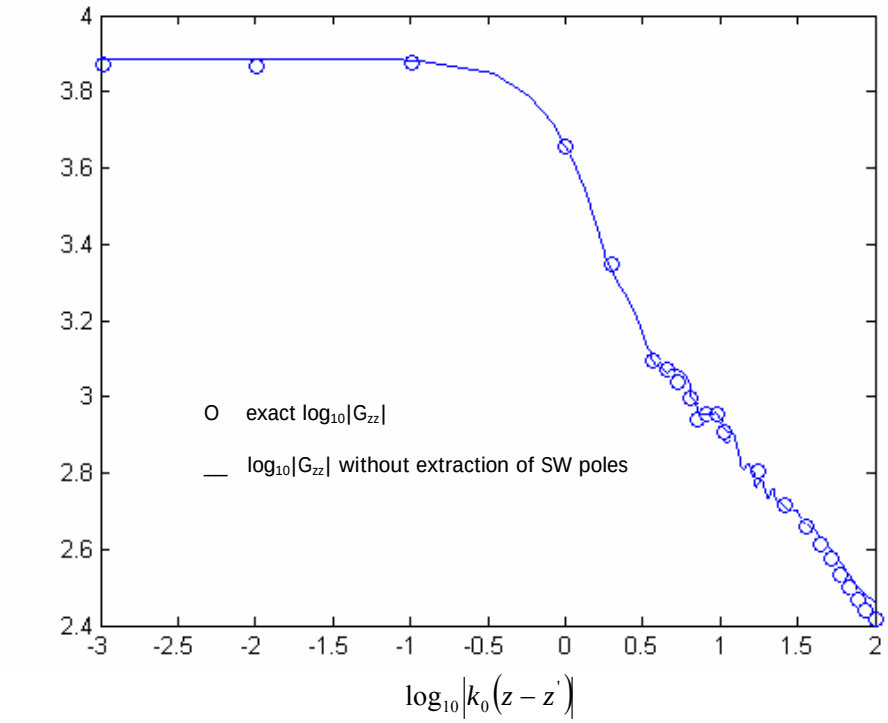

Figure IV.10 The exact and the spatial domain Green's function G_{zz} without extraction of surface wave poles, f=4.7GHz, $\varepsilon_{r_1} = 2.3$, $\rho' = \rho = 0.42\lambda_0$, $a_1 = 0.42\lambda_0$, $t_h = 0.02\lambda_0$.

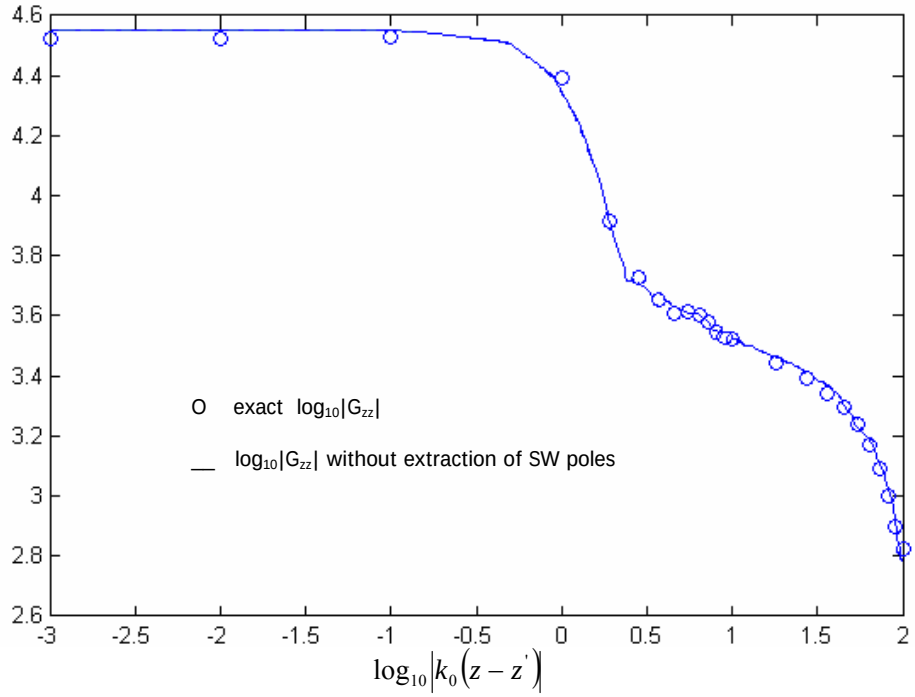

Figure IV.11 The exact and the spatial domain Green's function G_{zz} without extraction of surface wave poles, f=4.7GHz, $\varepsilon_{r_1} = 2.3$, $\rho' = \rho = 0.34\lambda_0$, $a_1 = 0.34\lambda_0$, $t_h = 0.04\lambda_0$.

When a proper deformed path is used in the evaluation of spatial domain Green's functions, it is observed from the given figures that removing the surface wave contributions from spectral domain Green's functions does not give an extra benefit. Hence regarding our research, unlike planar layered medium, it is not a critical issue to remove the surface wave contributions from the spectral domain Green's functions if a proper deformed path is used.

CHAPTER V

MUTUAL COUPLING BETWEEN ELECTRIC/MAGNETIC CURRENT ELEMENTS

In this chapter, the analysis of mutual coupling between two narrow strips and between two narrow slots placed on a cylindrically layered medium using Method of Moments (MoM) incorporation with the closed-form Green's functions is presented. Mutual impedance and mutual coupling coefficient formulations are also provided for both strip and slot example to demonstrate the use of both electric and magnetic type Green's functions in cylindrically layered media. Hence, it is preferred to explain Method of Moments (MoM) briefly, at first.

V.1 The Method of Moments (MoM)

The MoM is a numerical technique that is used to solve the problems stated as:

$$L\{f\} = g \tag{V.1}$$

where L is a linear operator which may be differential, integral (which is in our analysis) and g is the known function.

In order to solve the problem, the unknown function to be determined $f(x)$ is approximated by series of known N basis or expansion functions $f_n(x)$,

$$f(x) = \sum_{n=1}^{N} \alpha_n f_n(x) \tag{V.2}$$

where α_n's are the unknown coefficients that are to be solved. (V.3) is obtained by substituting (V.2) into (V.1),

$$L\left\{\sum_{n=1}^{N} \alpha_n f_n(x)\right\} = g(x) \tag{V.3}$$

Since L is a linear operator, (V.3) can be expressed as,

$$\sum_{n=1}^{N} \alpha_n L\{f_n(x)\} = g(x) \tag{V.4}$$

The remainder function *R(x)* is defined as

$$R(x) = \sum_{n=1}^{N} \alpha_n L\{f_n(x)\} - g(x) \neq 0 \tag{V.5}$$

The remainder function *R(x)* is tested with the weighting (or testing) function w_m in order to have a zero inner product,

$$\langle w_m, R \rangle = 0 \qquad \text{for m} = 1,2,...\text{N} \tag{V.6}$$

Hence (V.6) is obtained as,

$$\left\langle w_m, \sum_{n=1}^{N} \alpha_n L\{f_n(x)\} - g(x) \right\rangle = 0 \tag{V.7}$$

Using the linearity of L, (V.7) can be expressed as

$$\left\langle w_m, \sum_{n=1}^{N} \alpha_n L\{f_n(x)\} \right\rangle = \langle w_m, g(x) \rangle \qquad \text{for m} = 1,2,...\text{N} \tag{V.8}$$

Using the linearity property of the inner product, (V.8) can also be written as

$$\sum_{n=1}^{N} \alpha_n \langle w_m, L\{f_n(x)\} \rangle = \langle w_m, g(x) \rangle \qquad \text{for m} = 1,2,...\text{N} \tag{V.9}$$

This set of equations can be written in the matrix form as

$$[Z_{mn}][\alpha_n] = [V_m] \tag{V.10}$$

where $Z_{mn} = \langle w_m, Lf_n \rangle$ and $V_m = \langle w_m, g \rangle$. Z is called the MoM matrix and V is caled the excitation vector. When the basis and the testing functions are same, the method is called as Galerkin's method (the method used in our analysis of mutual coupling).

V.2 Mutual Coupling Between Two Narrow Strips

For the analysis of the mutual coupling between two narrow strips on a multilayer cylinder, a structure which is given in Figure V.1 is used.

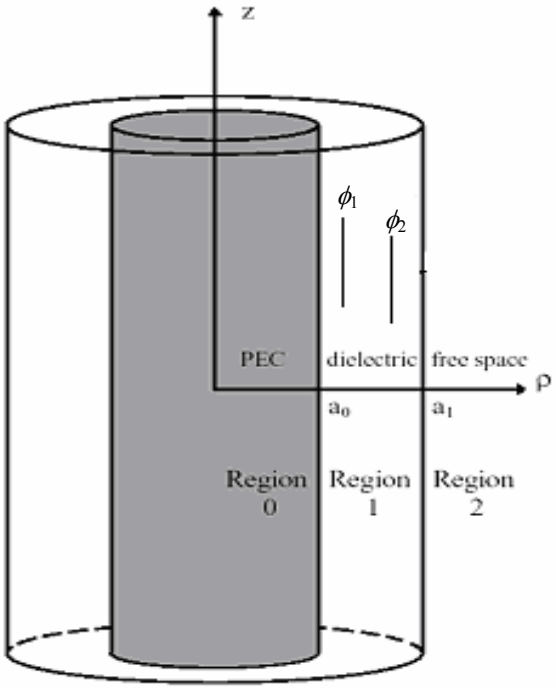

Figure V.1 A 3-layer structure with Region 0: PEC, Region 1: ε_{r_1} =2.3, μ_{r_1} =1, Region 2: free space, the first and second strips on ρ=a_1 are placed at ϕ_1 and ϕ_2, respectively.

According to MoM procedure, one starts with the boundary condition that the total tangential electric field on the conductor is zero,

$$\hat{n} \times \overline{E} = 0 \text{ on a strip.} \tag{V.11}$$

Then the total electric field is, $\overline{E} = \overline{E}^s + \overline{E}^i$, where $\overline{E}^i$ is the field generated by a known probe current density $\overline{J}^i$ and $\overline{E}^s$ is the field generated by an unknown induced current $\overline{J}^s$ that is to be determined.

$$\hat{n} \times (\overline{E}^s + \overline{E}^i) = 0 \tag{V.12}$$

The unit normal to the surface is denoted by $\hat{n}$ which is $\hat{a}_\rho$ for this problem.

Knowing that $\overline{E}^i = \overline{G}^E * \overline{J}^i$ and $\overline{E}^s = \overline{G}^E * \overline{J}^s$, (V.12) can be written as

$$\hat{n} \times (\overline{G}^E * \overline{J}^s) = -\hat{n} \times (\overline{G}^E * \overline{J}^i) \tag{V.13}$$

where $*$ denotes convolution, $\overline{J}^i$ is the known current density and $\overline{J}^s$ is the total surface current density on the narrow strips that is to be determined.

According to MoM, the total surface current density $\overline{J}^s$ can be expressed interms of N subsectional basis functions as

$$\bar{J}^s = \sum_{n1} a_{n1}\bar{J}_{n1} + \sum_{n2} a_{n2}\bar{J}_{n2} \tag{V.14}$$

where J_{n1} is basis function of the first strip, J_{n2} is the basis function of the second strip.

Hence, putting the total surface current density $\bar{J}^s$ in (5.4) into (5.3) gives

$$\sum_{n1} a_{n1}(\bar{G}^E * \bar{J}_{n1}) + \sum_{n2} a_{n2}(\bar{G}^E * \bar{J}_{n2}) = -(\bar{G}^E * \bar{J}^i) \tag{V.15}$$

Testing (V.15) with the testing functions J_{m1} and J_{m2}, gives equations with inner product terms such as

$$\sum_{n1} a_{n1}\left\langle \bar{J}_{m1}, \bar{G}^E * \bar{J}_{n1} \right\rangle + \sum_{n2} a_{n2}\left\langle \bar{J}_{m1}, \bar{G}^E * \bar{J}_{n2} \right\rangle = -\left\langle \bar{J}_{m1}, \bar{G}^E * \bar{J}^i \right\rangle \tag{V.16}$$

$$\sum_{n1} a_{n1}\left\langle \bar{J}_{m2}, \bar{G}^E * \bar{J}_{n1} \right\rangle + \sum_{n2} a_{n2}\left\langle \bar{J}_{m2}, \bar{G}^E * \bar{J}_{n2} \right\rangle = -\left\langle \bar{J}_{m2}, \bar{G}^E * \bar{J}^i \right\rangle \tag{V.17}$$

Since the strips are narrow, the basis and testing functions of each strip J_n and J_m are selected as rooftop functions shown in Figure V.2

$$J_{zn}(z,l) = \begin{Bmatrix} \frac{1}{wh_z}\left[(1-n)h_z + z\right] & (n-1)h_z \le z \le nh_z & ,|l| \le \frac{w}{2} \\ \frac{1}{wh_z}\left[(1-n)h_z + z\right] & nh_z \le z \le (n+1)h_z & ,|l| \le \frac{w}{2} \end{Bmatrix} \tag{V.18}$$

where w is the width of each strip.

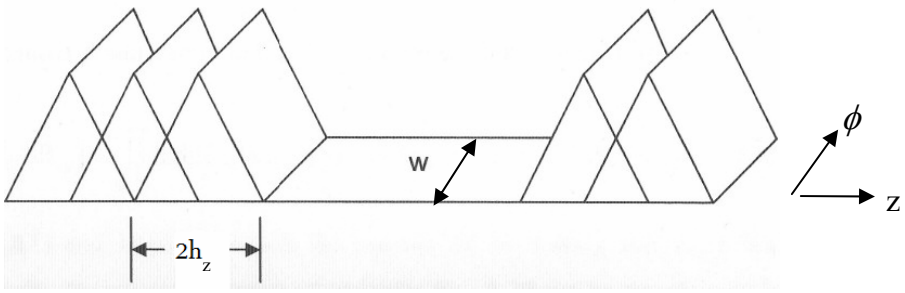

Figure V.2 Rooftop functions

For the spatial domain MoM formulation, the typical matrix equation can be formed by using (V.16) and (V.17)

$$\begin{bmatrix} \left\langle \bar{J}_{m1}, \bar{G}^E * \bar{J}_{n1} \right\rangle & \left\langle \bar{J}_{m1}, \bar{G}^E * \bar{J}_{n2} \right\rangle \\ \left\langle \bar{J}_{m2}, \bar{G}^E * \bar{J}_{n1} \right\rangle & \left\langle \bar{J}_{m2}, \bar{G}^E * \bar{J}_{n2} \right\rangle \end{bmatrix} \begin{bmatrix} a_{n1} \\ a_{n2} \end{bmatrix} = \begin{bmatrix} -\left\langle \bar{J}_{m1}, \bar{G}^E * \bar{J}^i \right\rangle \\ -\left\langle \bar{J}_{m2}, \bar{G}^E * \bar{J}^i \right\rangle \end{bmatrix} \qquad \text{(V.19)}$$

where m_i, n_i =1,...N, i=1,2 , $*$ denotes convolution, $\bar{J}^i$ is taken as a delta gap source, $\bar{J}_{m1}$, $\bar{J}_{n1}$ and $\bar{J}_{m2}$, $\bar{J}_{n2}$ are testing and basis functions of the first strip and the second strip, respectively.

The matrix entries in (V.19) can be written in the following form

$$Z_{mn} = \iint dz dl \; J_{mz}(z,l) \iint dz' dl' \; G_{zz}^E(z-z', l-l') \, J_{nz}(z', l') \qquad \text{(V.20)}$$

where l and l' are the "arc length" variables which are given as $l = a_1 \phi$ and $l' = a_1 \phi'$.

Galerkin's procedure is employed in the mutual coupling analysis with the selection of testing function $\bar{J}_m$ and basis function $\bar{J}_n$ of each strip same. This choice results in a symmetric matrix, hence considerably reduces the computation time of Z_{mn}. Once a proper column or row is calculated, since the matrix entries are the same whenever |m-n|=s, where m is the row and n is the column number, the entire matrix is filled. If N basis functions are employed, even though the dimension of the resulting matrix is NxN, the number of calculated matrix entry is only N.

By changing of variables $u=z-z'$ and $v=l-l'$, (V.20) can be written as

$$Z_{mn} = \iint dz \, dl \iint du dv \; G_{zz}^E(u,v) \; J_{mz}(z,l) \; J_{nz}(z-u, l-v) \qquad \text{(V.21)}$$

Rooftop functions, which are triangular in longitudinal direction and uniform in the transverse direction are suitable for our mutual coupling analysis. Selecting rooftop functions for the testing and the basis functions, reduces the quadruple integrals in (V.21) to two dimensional integrals (u and v integration) by carrying out the convolutional integral over testing and basis functions analytically, therefore this selection also reduces the computational time of Z_{mn} as a consequence of getting rid of numerically integration of two dimensional

convolutional integral. The analytical evaluation of this convolutional integral is given in Appendix C.

Putting the closed-form of G_{zz} [26] given in (V.22) into (V.21), (V.23) is obtained,

$$G_{zz}^{E}(u,v) = \frac{1}{2\pi}\int dk_z \; e^{-jk_z(z-z')} \sum_k G_{zz}^{k}(\rho=\rho',k_z)\, e^{jk(\phi-\phi')} \qquad \text{(V.22)}$$

$$Z_{mn} = \iint dz\, dl \iint du\, dv \left\{ \frac{1}{2\pi}\int dk_z \, e^{-jk_z(z-z')} \left(\sum_k G_{zz}^{k} e^{jk(\phi-\phi')}\right)\right\} J_{mz}(z,l)\, J_{nz}(z-u,l-v) \qquad \text{(V.23)}$$

Expressing the current density J_{mz} by a rooftop function, i.e., a Triangular function in z direction and a Pulse function in ϕ direction, i.e. $J_{mz} = T_{mz}(z)\, \mathrm{P}_{mz}(l)$ and changing the order of integrals, (V.24) is obtained,

$$Z_{mn} = \iint du dv \left\{ \frac{1}{2\pi}\int dk_z \, e^{-jk_z u} \left(\sum_k G_{zz}^{k} e^{jk(\phi-\phi')}\right)\right\} \int dl \;\; \mathrm{P}_{m\phi}(l)\, \mathrm{P}_{n\phi}(l-v) \int dz \; T_{mz}(z)\, T_{nz}(z-u) \qquad \text{(V.24)}$$

While calculating Z_{mn} in (V.24), an integral subroutine in MATLAB® called Gaussian Quadrature is used for the numerical integration.

For the calculation of (V.24), a hybrid method is used, depending on whether ϕ is close to ϕ' or not. If ϕ is not close to ϕ' the closed-form Green's functions are employed. When ϕ is close to ϕ', since the spectral-domain Green's functions do not converge, (ϕ - ϕ') difference term is handled with the convolutional integral in the spectral-domain in the calculation of MoM matrix element Z_{mn}.

To be more explanatory, the last integral in (V.24), which is a convolution integral, is evaluated analytically. For the rest of the calculation of the matrix entry Z_{mn}, a hybrid method is used:

-when ϕ is not close to ϕ', the ϕ integration and the closed-form of G_{zz} are evaluated independently;

-when ϕ is close to ϕ', (V.25) is obtained from (V.24) and used for the calculation for the matrix entry Z_{mn} such as: first, Pulse functions are integrated giving an analytical result interms of v, then the multiplication of this analytical term with e^{jkv} is used as an integrand in v integration, at the last step, the spectral domain k_z integral is calculated in closed-form.

$$Z_{mn}=\int du\left\{\frac{1}{2\pi}\int dk_z\ e^{-jk_z u}\left\{\sum_{\mathrm{k}} G_{zz}^{k}\int dv\ e^{jkv}\left(\int dl\ \mathrm{P}_{m\phi}(l)\mathrm{P}_{n\phi}(l-v)\right)\right\}\right\}\left\{\int dz\ T_{mz}(z)\ T_{nz}(z-u)\right\} \quad \text{(V.25)}$$

V.3 Mutual Coupling Between Two Narrow Slots

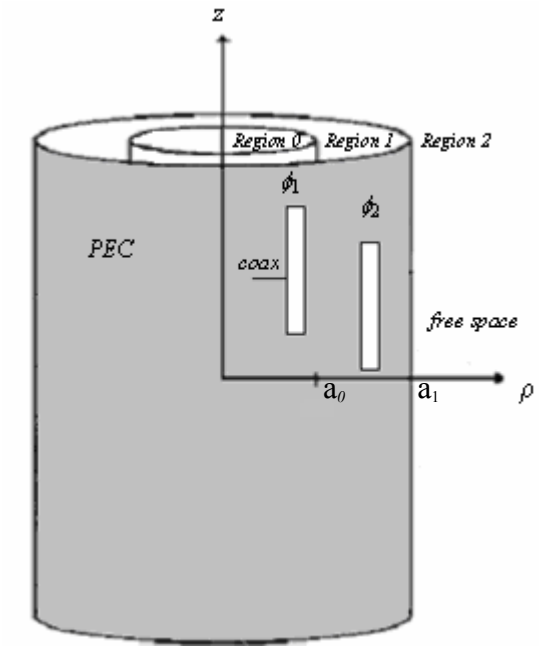

Figure V.3 A 3-layer structure with Region 0: ε_{r_0} =2, μ_{r_0} =1, Region 1: ε_{r_1} = 5, μ_{r_1} =1, Region 2: free space.

Each aperture in Figure V.3 can be closed and then replaced by an equivalent magnetic surface current density $\bar{J}^m$ by using the equivalence principle. When the field in a region of space is interested, there is no need to know the actual sources. Since many source distributions outside a given region can produce the same field inside the region, equivalent sources will serve as well. Figure V.4 represents two figures of which the left problem is the original problem, the right one is the equivalent problem. The original figure represents a source internal to S and free space external to S. The equivalent problem can be set as follows: Let

there exists the null field internal to S and the original field exists external to S. To support this field, there must exist $\bar{J}_s$ and $\bar{M}_s$ on S.

$$\bar{J}_s = \hat{n} \times \bar{H} \qquad \bar{M}_s = \bar{E} \times \hat{n}$$

where $\bar{E}$ and $\bar{H}$ are the original fields over S. From the uniqueness theorem we know that the field calculated will be the originally postulated field.

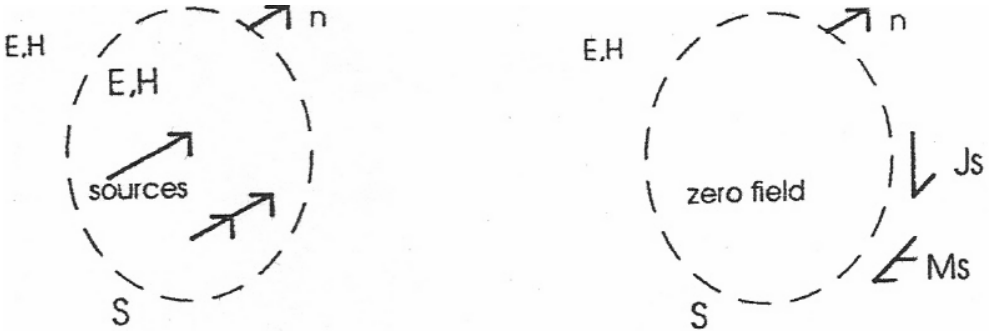

Figure V.4 Equivalence Principle

A cylindrical 3-layer medium with two narrow slots placed on $\rho = a_1$ is given in Figure V.3. For this geometry, the aperture (slot) is closed and represented by an equivalent magnetic-current distribution $\bar{J}^m$ by using the equivalence principle. Since the tangential electric field across the slot can be represented by the equivalent magnetic-current distribution

$$\bar{J}^m = \bar{E} \times \hat{n} = \bar{E} \times \hat{a}_\rho \tag{V.26}$$

The unit normal to the surface is denoted by $\hat{n}$ which is $\hat{a}_\rho$ for this problem. The equivalent magnetic-current distributions inside and outside of PEC can be written as

$$\text{For } \rho > a_1, \quad \bar{J}^m_{out} = \bar{E} \times \hat{a}_\rho = E_\phi \hat{a}_\phi \times \hat{a}_\rho = -E_\phi \hat{a}_z \tag{V.27}$$

$$\text{For } \rho < a_1, \quad \bar{J}^m_{in} = \bar{E} \times (-\hat{a}_\rho) = E_\phi \hat{a}_\phi \times (-\hat{a}_\rho) = E_\phi \hat{a}_z \tag{V.28}$$

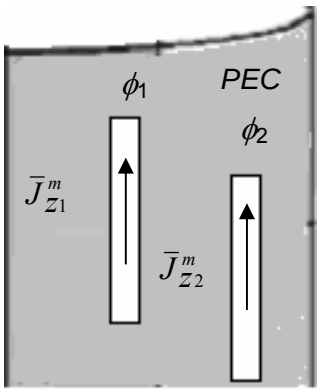

Figure V.5 Equivalent magnetic current distributions on each slot

Using the boundary condition that the tangential magnetic field is continous across the aperture,

$$\bar{H}_z^{in}(\bar{J}_{in}^m) = \bar{H}_z^{out}(\bar{J}_{out}^m) + \bar{J}_s\delta(z-d) \text{ at } \rho = a_1. \tag{V.29}$$

where $\bar{J}_s$ is the known probe current density at z =d.

Knowing that $\bar{H}^{in} = \bar{G}^H * \bar{J}_{in}^m$ and $\bar{H}^{out} = \bar{G}^H * \bar{J}_{out}^m$, (V.29) can be written as

$$(\bar{G}^H_{zz_{in}} * \bar{J}^m_{z_{in}}) = (\bar{G}^H_{zz_{out}} * \bar{J}^m_{z_{out}}) + \bar{J}_s\delta(z-d) \quad \text{at } \rho = a_1. \tag{V.30}$$

Here, $\bar{G}^H_{zz}$ is the magnetic type Green's function in z direction due to z-oriented magnetic current source.

According to MoM, the total surface current density $\bar{J}_z^m$ can be expressed interms of N subsectional basis functions as

$$\bar{J}^m_{z_{in}} = -\bar{J}^m_{z_{out}} = \sum_{n1} a_{n1}\bar{J}_{n1} + \sum_{n2} a_{n2}\bar{J}_{n2} \tag{V.31}$$

where J_{n1} is basis function of the first slot, J_{n2} is the basis function of the second slot.

Since the slots are narrow, the basis and testing functions of each slot J_n and J_m are selected as rooftop functions such that

$$J_{zn}(z,l)=\begin{Bmatrix}\dfrac{1}{wh_z}\left[(1-n)h_z+z\right] & (n-1)h_z\le z\le nh_z & ,|l|\le\dfrac{w}{2}\\ \dfrac{1}{wh_z}\left[(1-n)h_z+z\right] & nh_z\le z\le (n+1)h_z & ,|l|\le\dfrac{w}{2}\end{Bmatrix} \qquad \text{(V.32)}$$

where w is the width of each slot.

Hence, putting the total surface current density $\bar{J}_z^m$ in (V.31) into (V.30) gives

$$\sum_{n1} a_{n1}(\bar{G}^H_{zz_{in}}+\bar{G}^H_{zz_{out}})*\bar{J}_{n1}+\sum_{n2} a_{n2}(\bar{G}^H_{zz_{in}}+\bar{G}^H_{zz_{out}})*\bar{J}_{n2}=\bar{J}_s\delta(z-d) \qquad \text{(V.33)}$$

Testing (V.33) with the testing functions J_{m1} and J_{m2} gives equations with inner product terms such as

$$\sum_{n1} a_{n1}\left\langle \bar{J}_{m1},(\bar{G}^H_{zz_{in}}+\bar{G}^H_{zz_{out}})*\bar{J}_{n1}\right\rangle+\sum_{n2} a_{n2}\left\langle \bar{J}_{m1},(\bar{G}^H_{zz_{in}}+\bar{G}^H_{zz_{out}})*\bar{J}_{n2}\right\rangle=\left\langle \bar{J}_{m1},\bar{J}_s\delta(z-d)\right\rangle \qquad \text{(V.34)}$$

$$\sum_{n1} a_{n1}\left\langle \bar{J}_{m2},(\bar{G}^H_{zz_{in}}+\bar{G}^H_{zz_{out}})*\bar{J}_{n1}\right\rangle+\sum_{n2} a_{n2}\left\langle \bar{J}_{m2},(\bar{G}^H_{zz_{in}}+\bar{G}^H_{zz_{out}})*\bar{J}_{n2}\right\rangle=\left\langle \bar{J}_{m2},\bar{J}_s\delta(z-d)\right\rangle \qquad \text{(V.35)}$$

For the spatial domain MoM formulation, the typical matrix equation can be formed by using (V.34) and (V.35)

$$\begin{bmatrix}\left\langle \bar{J}_{m1},(\bar{G}^H_{zz_{in}}+\bar{G}^H_{zz_{out}})*\bar{J}_{n1}\right\rangle & \left\langle \bar{J}_{m1},(\bar{G}^H_{zz_{in}}+\bar{G}^H_{zz_{out}})*\bar{J}_{n2}\right\rangle\\ \left\langle \bar{J}_{m2},(\bar{G}^H_{zz_{in}}+\bar{G}^H_{zz_{out}})*\bar{J}_{n1}\right\rangle & \left\langle \bar{J}_{m2},(\bar{G}^H_{zz_{in}}+\bar{G}^H_{zz_{out}})*\bar{J}_{n2}\right\rangle\end{bmatrix}\begin{bmatrix}a_{n1}\\ a_{n2}\end{bmatrix}=\begin{bmatrix}\left\langle \bar{J}_{m1},\bar{J}_s\delta(z-d)\right\rangle\\ \left\langle \bar{J}_{m2},\bar{J}_s\delta(z-d)\right\rangle\end{bmatrix} \qquad \text{(V.36)}$$

where m_i,n_i =1,...N, i=1,2, $*$ denotes convolution, $\bar{J}_s$ is taken as a delta gap source, $\bar{J}_{m1}$, $\bar{J}_{n1}$ and $\bar{J}_{m2}$, $\bar{J}_{n2}$ are testing and basis functions of the first slot and the second slot, respectively.

The matrix entries in (V.36) can be written in the following form

$$Z_{mn}=\iint dzdlJ_{mz}(z,l)\iint dz'd\phi' G^H_{zz}(z-z',l-l')J_{nz}(z',l') \qquad \text{(V.37)}$$

In this application, the matrix entries Z_{mn} given in (V.37) are evaluated using the same procedure applied in (V.20)-(V.25).

V.4 Mutual Impedance and Coupling Coefficient of Two Current Elements

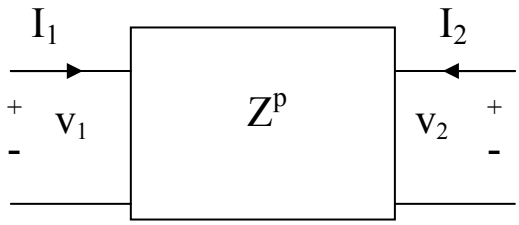

Figure V.6 Definitions of two-port parameters

Based on the two-port configuration given in Figure V.6, we can write [44],

$$\begin{aligned} V_1 &= Z_{11}^p I_1 + Z_{12}^p I_2 \\ V_2 &= Z_{21}^p I_1 + Z_{22}^p I_2 \end{aligned} \tag{V.38}$$

$$\begin{aligned} Z_{11}^p &= \left.\frac{V_1}{I_1}\right|_{I_2=0}, Z_{12}^p = \left.\frac{V_1}{I_2}\right|_{I_1=0} \\ Z_{22}^p &= \left.\frac{V_2}{I_2}\right|_{I_1=0}, Z_{21}^p = \left.\frac{V_2}{I_1}\right|_{I_2=0} \end{aligned} \tag{V.39}$$

Z_{11}^p is the input impedance of element one (element two open-circuited), can be written as

$$Z_{11}^P = \frac{-\int_v \boldsymbol{E}^{(1)} . \boldsymbol{J}_{ip}^{(1)} dv}{(I_{ip})^2} \tag{V.40}$$

where $\boldsymbol{E}^{(1)}$ is the total electric field at port one (port two open) due to impressed current density $\boldsymbol{J}_{ip}^{(1)}$ at port one with a terminal current I_{ip}=1A. Using (V.41) gives (V.42)

$$V_n = -\iint_{S_n} ds_n \bar{J}_n . \bar{E}^i \tag{V.41}$$

$$Z_{11}^{P} = -\sum_{n=1}^{2N} I_n V_n^{(1)} \tag{V.42}$$

where I_n are the expansion mode coefficients found from [Z][I]=[V] equation. $V_n^{(1)}$ are the induced voltages at port one due to current modes J_n in both patches.

The mutual impedance between ports one and two Z_{21}^{P} can be written as

$$Z_{21}^{P} = \frac{-\int_v \boldsymbol{E}^{(1)} . \boldsymbol{J}_{ip}^{(2)} dv}{(I_{ip})^2} \tag{V.43}$$

where $\boldsymbol{E}^{(1)}$ is the total electric field at port two, induced by impressed current density $\boldsymbol{J}_{ip}^{(1)}$ at port one (port two open) and $\boldsymbol{J}_{ip}^{(2)}$ is an impressed current source at port two, with impressed sources have terminal currents I_{ip}=1A. Again, using (V.41) gives

$$Z_{21}^{P} = -\sum_{n=1}^{2N} I_n V_n^{(2)} \tag{V.44}$$

where $V_n^{(2)}$ are the induced voltages at port two due to current modes J_n in both patches.

As a result of reciprocity theorem, $Z_{21}^{P} = Z_{12}^{P}$.

The input impedance for a single strip can be calculated using (V.42) with replacing 2N by N, since the second antenna is not present.

Another way of calculating the mutual impedance is given by [45]

$$Z_{21} = \iint_{S_1} ds_1 \bar{J}_1(\bar{r}_1) . \left(\iint_{S_2} ds_2 \bar{\bar{G}}(\bar{r}_1, \bar{r}_2) \bar{J}_2(\bar{r}_2) \right) \tag{V.45}$$

The coupling coefficient matrix $\bar{S}$ can be defined as [46],[47],[48]

$$\bar{S} = \begin{bmatrix} S_{11} & S_{12} \\ S_{21} & S_{22} \end{bmatrix} = \left(\bar{Z} - \bar{Z}_0 \right) \left(\bar{Z} + \bar{Z}_0 \right)^{-1} \tag{V.46}$$

Hence it can be written as,

$$\bar{S} = \begin{bmatrix} S_{11} & S_{12} \\ S_{21} & S_{22} \end{bmatrix} = \left(\begin{bmatrix} Z_{11} & Z_{12} \\ Z_{21} & Z_{22} \end{bmatrix} - \begin{bmatrix} Z_0 & 0 \\ 0 & Z_0 \end{bmatrix} \right) \left(\begin{bmatrix} Z_{11} & Z_{12} \\ Z_{21} & Z_{22} \end{bmatrix} + \begin{bmatrix} Z_0 & 0 \\ 0 & Z_0 \end{bmatrix} \right)^{-1} \tag{V.47}$$

After some manipulations, the mutual coupling coefficient S_{21} can be found as [49]

$$S_{21} = \frac{2Z_{12}Z_0}{(Z_{11}+Z_0)(Z_{22}+Z_0) - Z_{12}Z_{21}} \tag{V.48}$$

where Z_0 is the characteristic impedance of the feeding coax which is assumed to be 50Ω.

V.5 Numerical Results

In this section, numerical results in the form of mutual coupling between two narrow strips and between two narrow slots placed on a cylindrically layered medium using MoM incorporation with the closed-form Green's functions is presented. The current distributions on each printed element and the mutual impedance and the mutual coupling coefficient results are provided. Mutual impedance and mutual coupling coefficient results are also provided for both strip and slot example to demonstrate the use of both electric and magnetic type Green's functions in cylindrically layered media. Besides, to assess the accuracy of the method developed in this thesis, the obtained results for the mutual coupling between two narrow strips are compared with an eigenfunction solution given by [50].

V.5.1 Mutual Coupling Between Two Narrow Strips

Mutual coupling between two *z*-directed narrow strips placed on a multilayer cylindrical geometry presented in Figure V.7 is evaluated using the procedure discussed in Section V.2. The innermost layer is perfect electric conductor (PEC), the radius of the cylinder is a_1 and the thickness of the dielectric coating is t_h (hence $a_1 = a_0 + t_h$). The first and second narrow strip on $\rho = a_1$ are placed at $\phi = \phi_1$ and $\phi = \phi_2$, respectively. Each narrow strip a length as $L = \lambda_0/2$ and width as $w = 0.025\ \lambda_0$. The excitation is done by a probe on the first strip with different feed locations. Figure V.8 and Figure V.9 show the magnitude of the current

distributions on the first strip and the second strip, respectively, for different feed positions, when (ϕ_1 - ϕ_2)=π/24 radians.

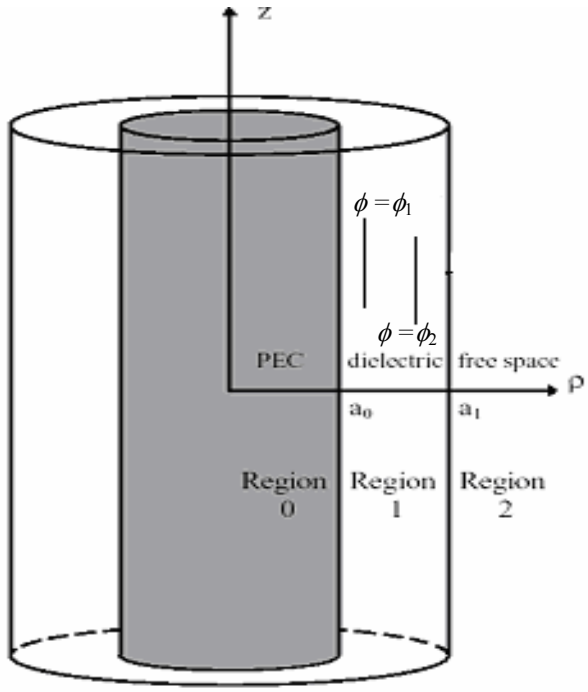

Figure V.7 A 3-layer structure with Region 0: PEC, Region 1: ε_{r_1} =2.3, μ_{r_1} =1, Region 2: free space, a_0= 20mm, a_1= 21mm, f =4.7GHz, the first and second strip on $\rho = a_1$ are placed at $\phi = \phi_1$ and $\phi = \phi_2$, respectively.

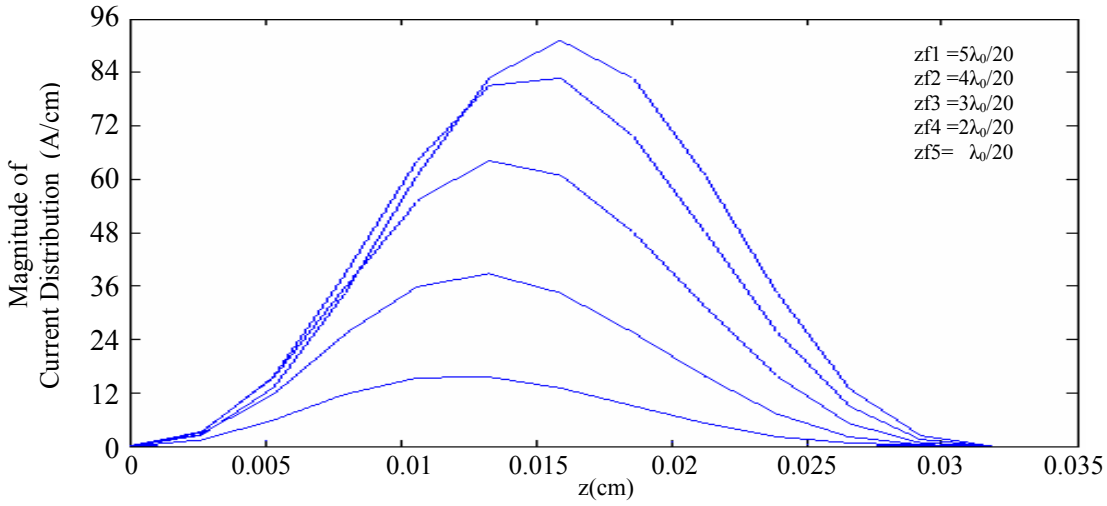

Figure V.8 The magnitude of the electric current distribution on the first strip, L= $\lambda_0/2$, w=0.025 λ_0, (ϕ_1 - ϕ_2)=π/24 radians, for different feed positions, where zfi is the i'th feed location of the first strip.

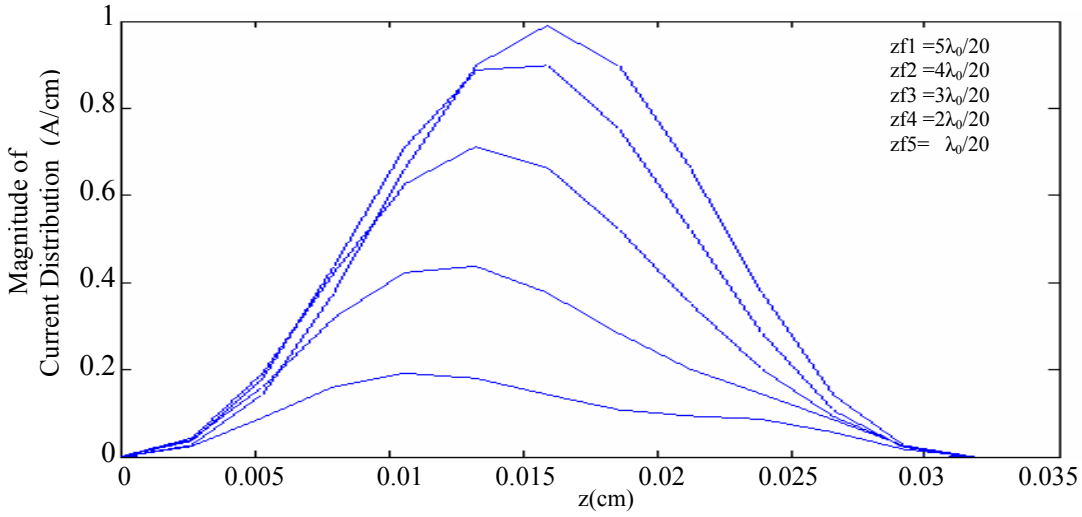

Figure V.9 The magnitude of the electric current distribution on the second strip, L= $\lambda_0/2$, w=0.025 λ_0, (ϕ_1 - ϕ_2)=$\pi/24$ radians, for different feed positions, where zfi is the i'th feed location of the first strip.

For the validity of the proposed method in Section V.2, the results given in [50] which uses eigenfunction solution are reproduced. These results with the proposed ones together are shown in Figure V.10-Figure V.12. The structure given in Figure V.7 is used, each strip having $\lambda_0/2$ length and 0.002 λ_0 width, the dielectric constant ε_{r_1} =2.

The mutual impedance Z_{21} is calculated using the equation given by (V.45)

$$Z_{21} = \iint_{S_1} ds_1 \bar{J}_1(\bar{r}_1).\left(\iint_{S_2} ds_2 \bar{G}(\bar{r}_1,\bar{r}_2)\bar{J}_2(\bar{r}_2)\right)$$

and the mutual coupling coefficient S_{21} is evaluated using (V.48)

$$S_{21} = \frac{2Z_{12}Z_0}{(Z_{11}+Z_0)(Z_{22}+Z_0)-Z_{12}Z_{21}}$$

where Z_0 is the characteristic impedance of the feeding coax which is assumed to be 50Ω.

Figure.V.10 shows the mutual impedance Z_{21} between two z-directed narrow strips versus S_φ when frequency f is 4.7 GHz and the outer cylinder radius a_1 is 0.5 λ_0, dielectric thickness t_h is 0.06 λ_0. S_φ is the angular spacing between two z-directed strips with respect to free-space wavelength λ_0.

Figure V.11 shows the mutual impedance Z_{21} between two z-directed narrow strips versus S_φ when frequency f is 4.7 GHz and the outer cylinder radius a_1 is 0.3 λ_0, dielectric thickness t_h is 0.06 λ_0. Figure V.12 shows the mutual impedance Z_{21} between two z-directed narrow strips versus S_φ when frequency f is 2 GHz and the outer cylinder radius a_1 is 0.5 λ_0, dielectric thickness t_h is 0.06 λ_0. It is clearly seen that the results for eigenfunction solution [50] and the proposed method in this paper are in good agreement with each other.

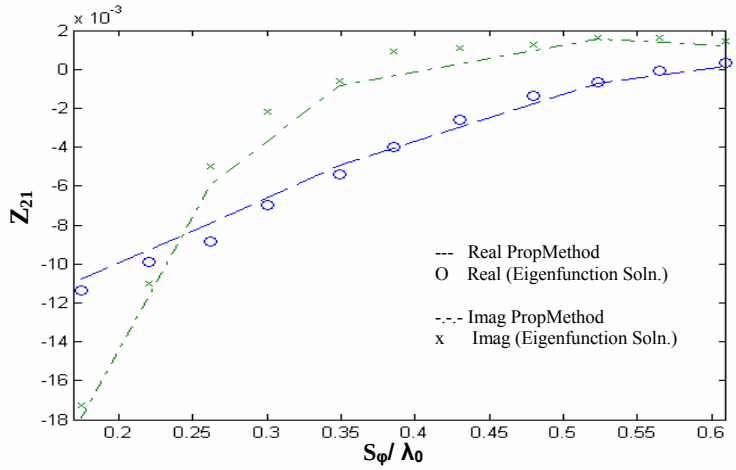

Figure V.10 Real and Imaginary parts of the mutual impedance Z_{21} between two z-directed narrow strips versus separation when f=4.7 GHz, a_1=0.5 λ_0.

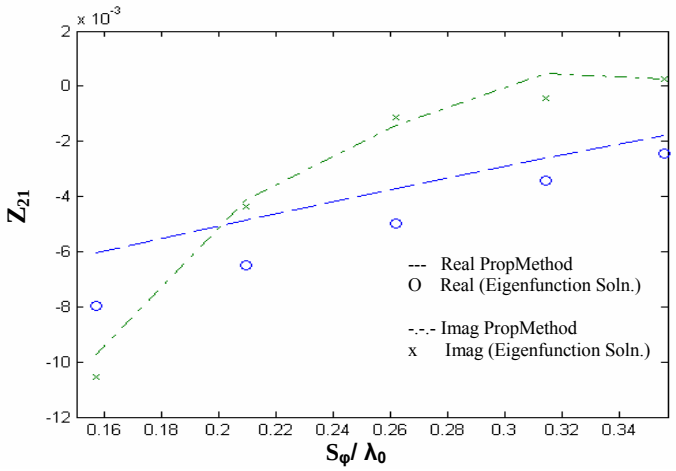

Figure V.11 Real and Imaginary parts of the mutual impedance Z_{21} between two z-directed narrow strips versus separation, when f=4.7 GHz, a_1=0.3 λ_0.

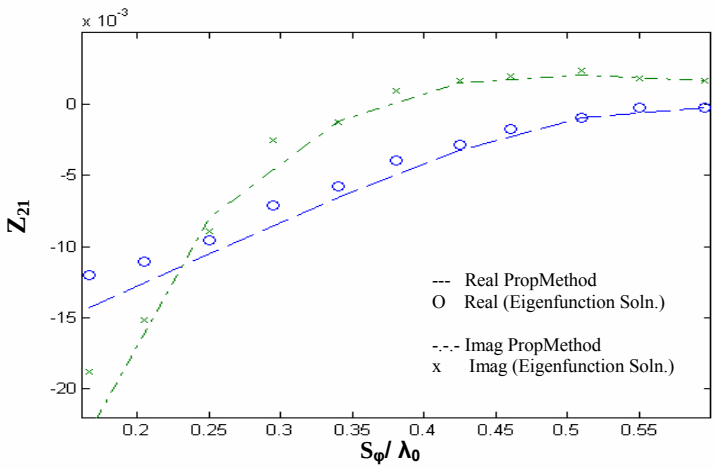

Figure V.12 Real and Imaginary parts of the mutual impedance Z_{12} between two z-directed narrow strips versus separation when f=2 GHz, a_1=0.5 λ_0.

Mutual coupling between two z-directed narrow strips on a cylindrical 3-layer medium given in Figure V.7 is evaluated using the method discussed in Section V.2. The excitation is done by a probe. Each strip has $\lambda_0/2$ length and 0.04 λ_0 width.

Figure V.13 and Figure V.14 show the mutual impedance Z_{21} and the mutual coupling coefficient S_{21} of two z-directed narrow strips versus the angular spacing S_φ when f=4.7 GHz, ε_{r_1}=2.3.

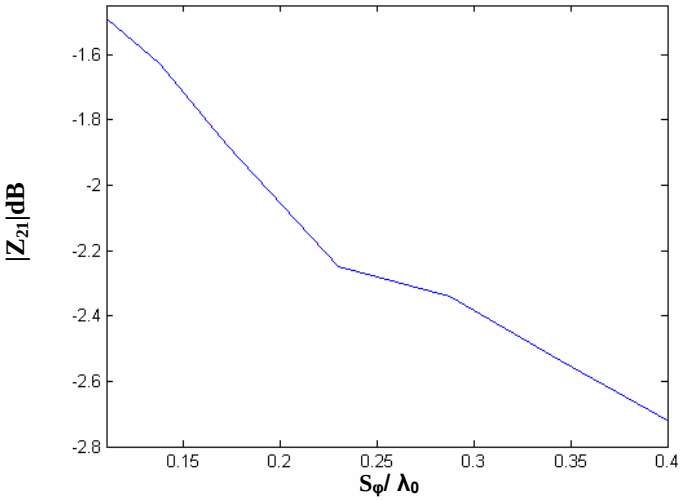

Figure V.13 Mutual impedance Z_{21} for H-plane coupling case of two z-directed narrow strips at f=4.7 GHz, a_0=20mm, a_1=21mm, ε_{r_1}=2.3, L=$\lambda_0/2$.

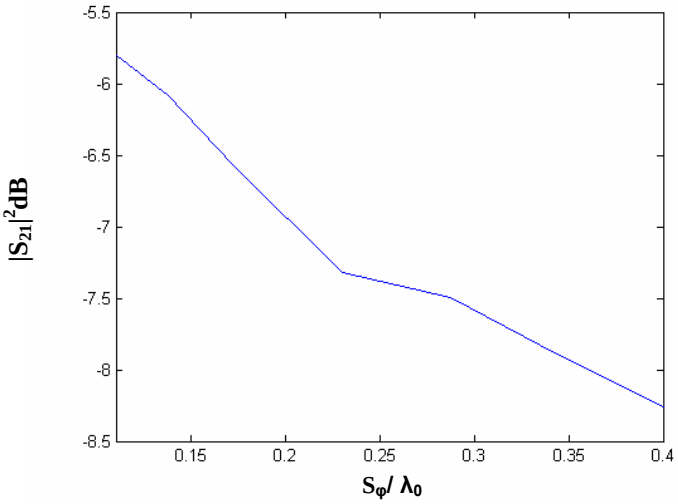

Figure V.14 Mutual coupling coefficient S_{21} for H-plane coupling case of two z-directed narrow strips at f=4.7 GHz, a_0=20mm, a_1=21mm, ε_{r_1} =2.3, L=$\lambda_0/2$.

V.5.2 Mutual Coupling Between Two Narrow Slots

Mutual coupling between two narrow slots placed on a multilayer cylindrical geometry presented in Figure V.15 is evaluated using the procedure discussed in Section V.3.

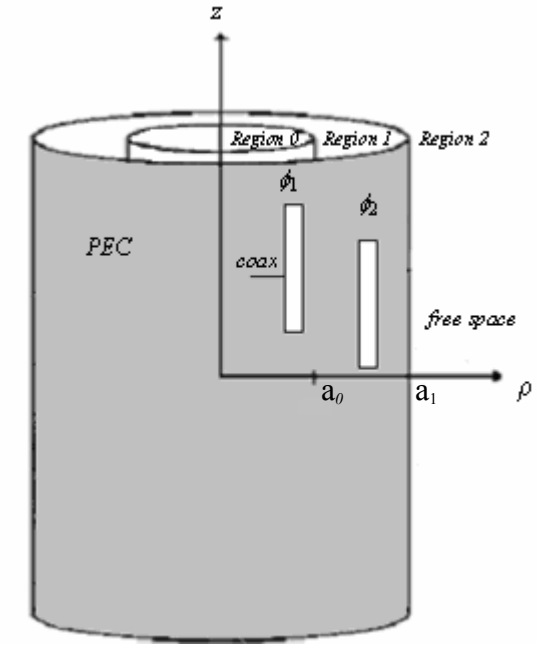

Figure V.15 A 3-layer structure with Region 0: ε_{r_0} =5, μ_{r_0} =1 Region 1: ε_{r_1} =2, μ_{r_1} =1, Region 2: free space, a_0= 20mm, a_1= 21mm, f=2 GHz.

For this application, the first and second narrow slot on $\rho = a_1$ are placed at $\phi = \phi_1$ and $\phi = \phi_2$, respectively. The excitation is done by a coax on the first slot with different feed locations. Each slot has a length as $L=\lambda_0/2$ and width as $w=0.025\ \lambda_0$. Figure V.16 and Figure V.17 show the current distributions on the first slot and the second slot, respectively.

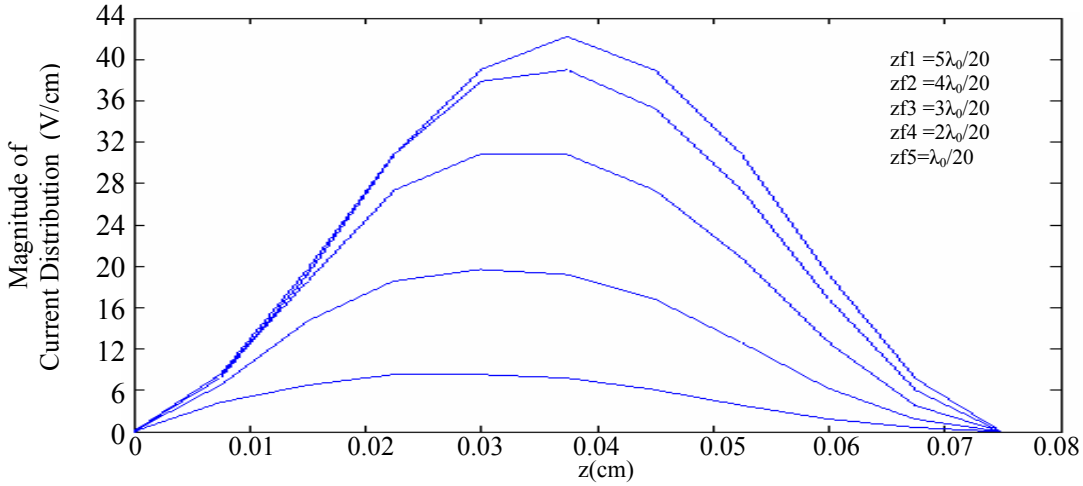

Figure V.16 The magnetic current distribution on the first slot for different feed locations when $(\phi_1 - \phi_2)=\pi/48$, where zfi is the i'th feed location of the first slot.

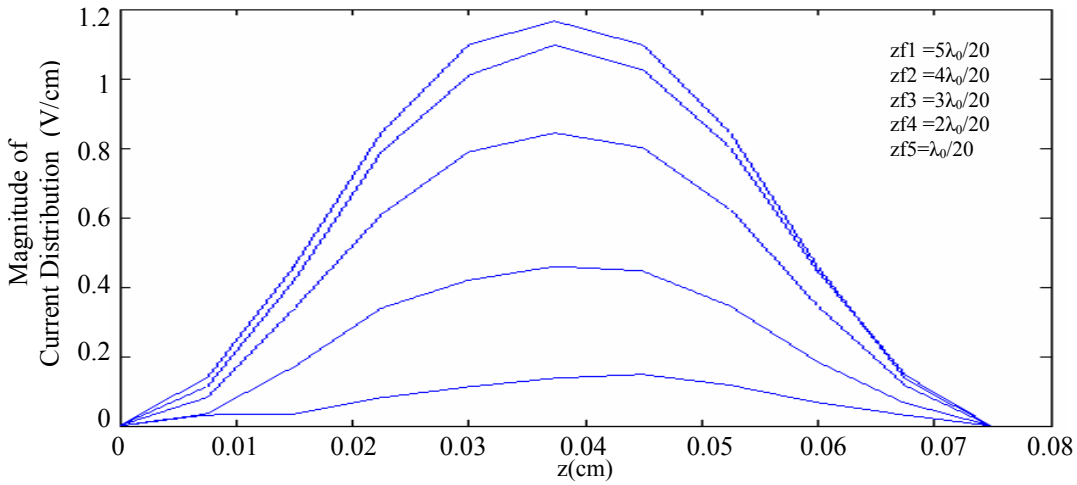

Figure V.17 The magnetic current distribution on the second slot for different feed locations when $(\phi_1 - \phi_2)=\pi/48$, where zfi is the i'th feed location of the first slot.

Mutual coupling between two z-directed narrow slots on a cylindrical statified media given in Figure V.15 is evaluated using the method discussed in Section V.3. The geometry in Figure V.18 is used for the mutual coupling evaluation. The excitation is done by a coax. Each slot has length as $L=\lambda_0/2$ and width as $w=0.04\lambda_0$.

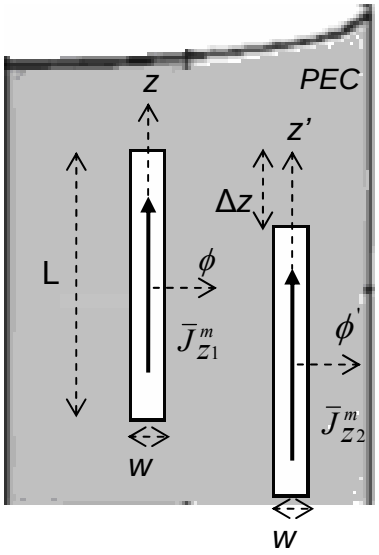

Figure V.18 Geometry used for mutual coupling between two z-directed narrow slots

Figure V.19 and Figure V.20 show the mutual impedance Z_{21} of two *z*-directed narrow slots versus the angular spacing S_φ for $\Delta z=0$ (the slots are parallel in z direction) and $\Delta z=\lambda_0/4$ values when f =2 GHz, ε_{r_0} =2 and ε_{r_1} =5.

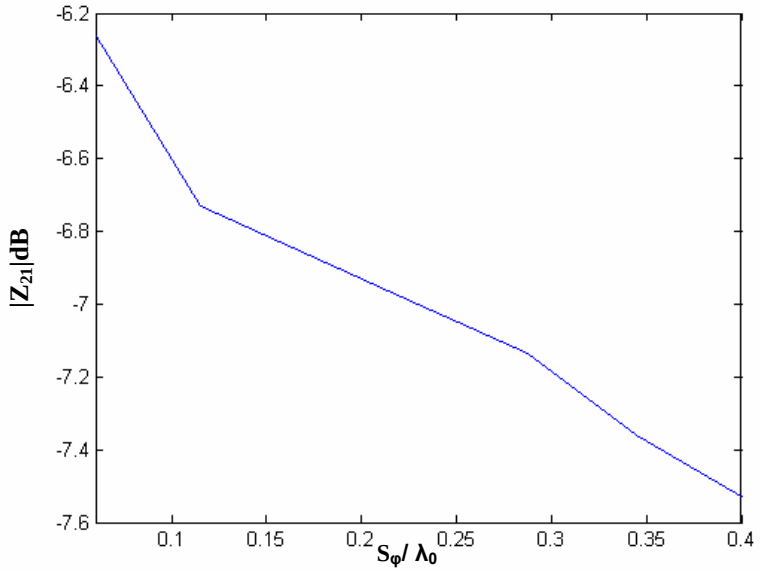

Figure V.19 Mutual impedance Z_{21} for H-plane coupling case of two z-directed narrow slots at f=2 GHz, a_0=20mm, a_1=21mm, $\Delta z = 0$, ε_{r_0} =2, ε_{r_1} =5, L=λ_0/2.

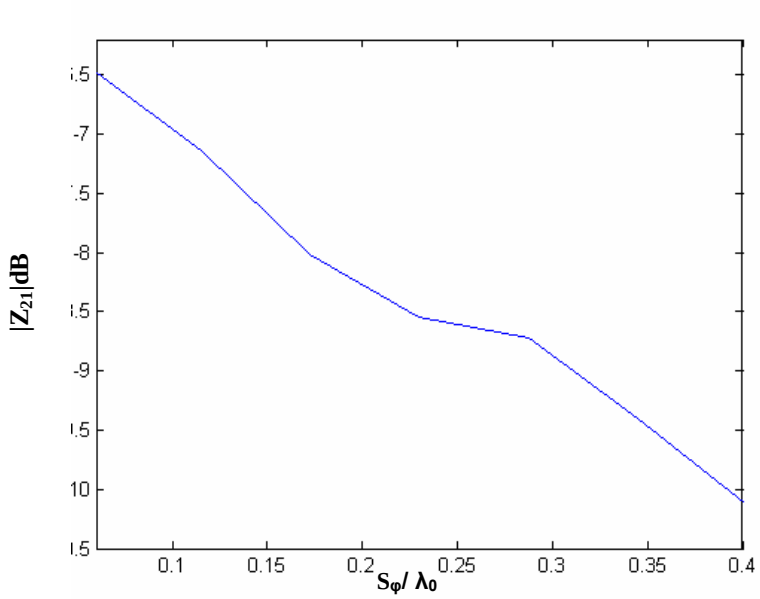

Figure V.20 Mutual impedance Z_{21} for H-plane coupling case of two z-directed narrow slots at f=2 GHz, a_0=20mm, a_1=21mm, $\Delta z = \lambda_0/4$, ε_{r_0} =2, ε_{r_1} =5, L=λ_0/2.

Figure V.21 and Figure V.22 show the mutual coupling coefficient S_{21} of two *z*-directed narrow slots versus the angular spacing S_φ for Δz=0 (the slots are parallel in z direction) and Δz=λ_0/4 values when f =2 GHz, ε_{r_0} =2 and ε_{r_1} =5.

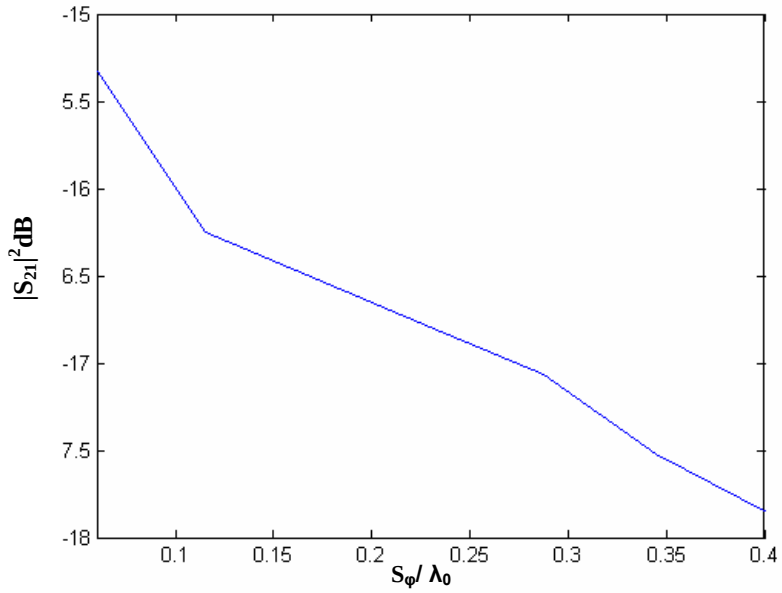

Figure V.21 Mutual coupling coefficient S_{21} for H-plane coupling case of two z-directed narrow slots at f=2 GHz, a_0=20mm, a_1=21mm, $\Delta z = 0$, ε_{r_0} =2, ε_{r_1} =5, L=λ_0/2.

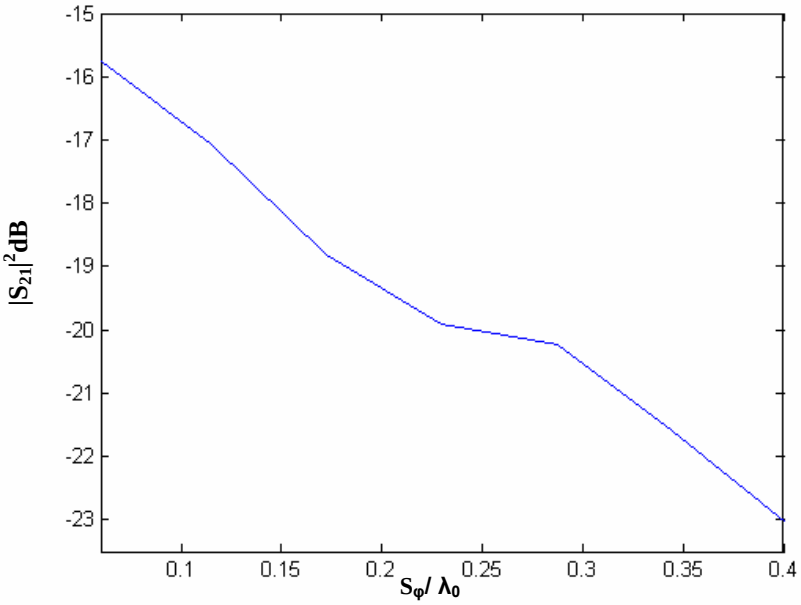

Figure V.22 Mutual coupling coefficient S_{21} for H-plane coupling case of two z-directed narrow slots at f=2 GHz, a_0=20mm, a_1=21mm, $\Delta z = \lambda_0/4$, ε_{r_0} =2, ε_{r_1} =5, L=λ_0/2.

CHAPTER VI

CONCLUSION

Under the scope of this thesis, numerically efficient analysis and design of conformal printed structures in cyindrically layered media using closed-form Green's functions is investigated. For this purpose the spectral domain Green's functions which were reported in the previously published work [26] were derived from the beginning. Then a code is reproduced in MATLAB® to obtain the spatial domain Green's functions of the electric and magnetic fields due to ϕ and z oriented electric and magnetic sources as [26]. The generated code computes the spatial domain closed-forms of $\tilde{G}^E_{zz}, \tilde{G}^H_{zz}, \tilde{G}^E_{\phi z}, \tilde{G}^H_{\phi z}$ for an electric and a magnetic dipole pointing in z direction, the spatial domain closed-forms of $\tilde{G}^E_{z\phi}, \tilde{G}^H_{z\phi}, \tilde{G}^E_{\phi\phi}, \tilde{G}^H_{\phi\phi}$ for an electric and a magnetic dipole pointing in ϕ direction. They are found to be in good agreement with those given in [26]. The remaining spatial domain Green's function components which are not provided in [26], the spatial domain closed-forms of ρ directed spectral domain Green's functions of electric and magnetic fields $\tilde{G}^E_{\rho z}, \tilde{G}^H_{\rho z}$ for an electric and a magnetic dipole pointing in z direction, $\tilde{G}^E_{\rho\phi}, \tilde{G}^H_{\rho\phi}$ for an electric and a magnetic dipole pointing in ϕ direction were also derived analytically and evaluated by the generated code. Therefore for ϕ and z oriented electric and magnetic sources the complete set is obtained.

The remaining spatial domain Green's function components which are not given in [26], the spatial domain closed-forms of z, ϕ and ρ directed spectral domain Green's functions of electric and magnetic fields, $\tilde{G}^E_{z\rho}, \tilde{G}^H_{z\rho}, \tilde{G}^E_{\phi\rho}, \tilde{G}^H_{\phi\rho}, \tilde{G}^E_{\rho\rho}, \tilde{G}^H_{\rho\rho}$ for both electric and magnetic dipole sources pointing in ρ direction were derived analytically and evaluated by the generated code. Therefore, the complete set of spatial domain dyadic Green's function components has been

obtained and is evaluated by the generated code. A new code is generated for the numerical integration to compare the exact and the approximate closed-form Green's functions.

The closed-form Green's functions when $\rho = \rho'$ are calculated using a similar procedure reported in a recently published work [27] and some results are presented for different closed-form Green's functions. To assess the accuracy of the procedure, for small $(\phi - \phi')$ values, the exact and different closed-form spatial-domain Green's function components of electric and magnetic fields due to different oriented electric and magnetic dipole sources are plotted together and it is observed that they are in good agreement.

In addition, a computationally efficient hybrid method is presented in conjunction with method of moments (MoM) technique which analyzes the mutual coupling between electric/magnetic current elements placed on a cylindrically layered medium. The hybrid method depends on the angular distance $(\phi - \phi')$ between the source and the observation point. If ϕ is not close to ϕ' the closed-form Green's functions are directly employed. Otherwise, the angular difference term $(\phi - \phi')$ is handled with the convolutional integral in the spectral-domain in the calculation of MoM matrix element Z_{mn}. Employing Galerkin's procedure and selecting testing and basis functions which allows to carry out the convolutional integral between the current elements analytically reduces the computational time of the matrix element Z_{mn}. Mutual impedance and mutual coupling coefficient results are also provided for printed electric and magnetic current elements to demonstrate the use of both electric and magnetic type Green's functions in cylindrically layered media. Besides, to assess the accuracy of the method developed in this thesis, the results obtained for the mutual coupling between two narrow electric current elements are compared with an eigenfunction solution given by [50]. It is clearly observed that the results for eigenfunction solution [50] and the presented method in this thesis are in good agreement with each other. The analysis and design of microstrip structures mounted on conformal structures that are extensively used in aircraft, spacecraft and mobile communication applications, where low cost, leight

weight and direct integrability with other devices are important, become easier by the hybrid method. Using the proposed hybrid method in conjunction with MoM technique, the analysis of multilayer coupling geometries such as slot-coupled microstrip patch antennas and slot antenna with microstrip feeding can be research topics for further studies.

In the scope of the study of surface wave contribution in cylindrically stratified media, the effect of the surface wave poles and the selection of the deformed path parameters are studied. When the deformed path parameters are selected in such a way that the deformed path passes close to the surface wave poles, it is observed that the spectral Green's functions hence the spatial domain Green's functions deteriorate. This deterioration is overcome by removing the surface wave poles from the spectral domain Green's functions and adding their contributions in the spatial domain. When a proper deformed path is used in evaluation of spatial-domain Green's functions, it is observed that removing the surface wave contributions from spectral-domain Green's functions does not give an extra benefit. Hence regarding our research, unlike planar layered medium, it is not a critical issue to remove the surface wave contributions from the spectral-domain Green's functions if a proper deformed path is used.

As a concluding remark, for future study, developing of the appropriate form of the spectral domain Green's functions which will be well behaved for ($\phi = \phi'$) when $\rho = \rho'$ is recommended. In that case, there may be no need to use the proposed hybrid method. Hence, the calculation of MoM matrix elements will be evaluated in closed-form for all possible $\left|\vec{\rho} - \vec{\rho}'\right|$ values.

BIBLIOGRAPHY

[1] K. R. Carver and J. W. Mink, "Microstrip antenna technology," IEEE Trans. Antennas Propagat., vol. AP-29, pp. 2-24, Jan. 1981.

[2] R. E. Munson, "Conformal microstrip antennas and microstrip phased arrays," IEEE Trans. Antennas Propagat., vol. AP-22, pp. 74-78, Jan. 1974.

[3] H. E. Bussey and J. H. Richmond, "Scattering by a lossy dielectric circular cylindrical multilayer, numerical values," IEEE Trans. Antennas Propogat., vol. AP-23, pp. 723-725, Sept. 1975.

[4] L. C. Kempel and J. L. Volakis, "Scattering by cavity-backed antennas on a circular cylinder" IEEE Trans. Antennas Propagat., vol. AP-42, pp. 1268-1279, Sept. 1994.

[5] L. C. Kempel, J. L. Volakis, and R. J. Sliva, "Radiation by cavity-backed antennas on a circular cylinder," Proc. Inst. Elect. Eng., vol. 142, pp. 233-239, June 1995.

[6] J. Ashkenazy, S. Shtrikman, and D. Treves, "Electric surface current model for the analysis of microstrip antennas on cylindrical bodies," IEEE Trans. Antennas Propagat., vol. AP-33, pp. 295-300, Mar. 1985.

[7] A. Nakatani and N.G. Alexopoulos, N.K. Uzunoglu, P.L.E. Uslenghi, "Accurate Green's Function Computation for Printed Circuit Antennas on Cylindrical Substrates" Electromagnetics 6:243-254, 1986.

[8] N. G. Alexopoulos and A. Nakatani, "Cylindrical substrate microstrip line characterization," IEEE Trans. Microwave Theory Tech., vol. MTT-35, pp.843-849, Sept. 1987.

[9] C. M. Krowne, "Cylindrical-rectangular microstrip antenna," IEEE Trans. Antennas Propagat., vol. AP-31, pp. 194-199, Jan. 1983.

[10] K. M. Luk, K. F. Lee, and J. S. Dahele,"Analysis of cylindrical-rectangular patch antenna," IEEE Trans. Antennas Propagat., vol. AP-37, pp. 143-147, Feb. 1989.

[11] K. M. Luk, K. F. Lee, "Characteristics of the cylindrical-circular patch antenna," IEEE Trans. Antennas Propagat., vol. AP-38, pp. 11194-1123, July. 1990.

[12] W. Y. Tam, A. K. Y. Lai, and K. M. Luk, "Cylindrical rectangular microstrip antennas with coplanar parasitic patches," in Proc. Inst. Elect. Eng., vol. 142, Aug. 1995, pp. 300-306.

[13] J. F. Kiang, "Response properties of cylindrical rectangular patch with composite ground plane," in Proc. Inst. Elect. Eng., vol. 142, Aug. 1995, pp. 307-313.

[14] K.L. Wong, Y. T. Cheng, and J. S. Row, "Resonance in a superstrate-loaded cylindrical-rectangular microstrip structure," IEEE Trans. Microwave Theory Tech., vol. MTT-41, pp. 814-819, May. 1993.

[15] R. B. Tsai and K. L. Wong, "Characterization of cylindrical microstriplines mounted inside a ground cylindrical surface," IEEE Trans. Microwave Theory Tech., vol. MTT-43, pp. 1607-1610, July. 1995.

[16] S. M. Ali, T. M. Habashy, J. F. Kiang, and J. A. Kong, "Resonance in cylindrical-rectangular and wraparound microstrip structures," IEEE Trans. Microwave Theory Tech., vol. 37, pp. 1773-1783, Nov. 1989.

[17] T. M. Habashy, S. M. Ali, and J. A. Kong, "Input impedance and radiation pattern of cylindrical-rectangular and wraparound microstrip antennas," IEEE Trans. Antennas Propagat., vol. 38, pp. 722-731, May. 1990.

[18] S. B. A. Fonseca and A. J. Giarola, "Analysis of microstrip wraparound antennas using dyadic Green's functions," IEEE Trans. Antennas Propagat., vol. AP-31, pp. 248-253, Mar. 1983.

[19] F. C. Silva, S. B. A. Fonseca, A. J. M. Soares, and A. J. Giarola, "Analysis of microstrip antennas on circular-cylindrical substrates with a dielectric overlay," IEEE Trans. Antennas Propagat., vol. 39, pp. 1398-1404, Sept. 1991.

[20] S. B. A. Fonseca and A. J. Giarola, "Dyadic Green's functions and their use in the analysis of microstrip antennas," in Advances in Electronics and Electron Physics, New York: Academic, 1985, vol. 65, pp. 1-90.

[21] Z. Xiang and Y. Lu, "Electromagnetic dyadic Green's function in cylindrically multilayered media," IEEE Trans. Microwave Theory Tech.,vol.44, pp. 614-621, Apr. 1996.

[22] Y. L. Chow, J. J. Yang, D. F. Fang, and G. E. Howard, "A closed-form spatial domain Green's function for the thick microstrip substrate," IEEE Trans. Microwave Theory Tech., vol. 39, pp. 588-592, Mar. 1991.

[23] M. I. Aksun, R. Mittra, "Derivation of closed-form Green's functions for a general microstrip geometry," IEEE Trans. Microwave Theory Tech., vol. 40, pp. 2055-2062, Nov. 1992.

[24] G. Dural, M. I. Aksun, "closed-form Green's functions for general sources and stratified media," IEEE Trans. Microwave Theory Tech., vol. 43, pp. 1545-1552, July 1995.

[25] M. I. Aksun, "A robust approach for the derivation of closed-form Green's functions," IEEE Trans. Antennas Propagat., vol. 44, pp. 651-658, May 1996.

[26] Ç. Tokgöz, "Derivation of closed-form Green's functions for Cylindrically Stratified Media," M.S.thesis, Dept. Elec. Electron. Eng., Middle East Technical Univ., Ankara, Turkey, August 1997.

[27] Jin Sun, Chao-Fu Wang, Le-Wei Li, Mook-Seng Leong, "Further Improvement for Fast Computation of Mixed Potential Green's Functions for Cylindrically Stratified Media" IEEE Trans.Antennas Propagat., vol. 52, No.11, pp. 3026-3036, Nov. 2004.

[28] W. C. Chew, *Waves and Fields in Inhomogeneous Media*, New York: Van Nostrand, 1990.

[29] J. R. Lovell and W. C. Chew, "Response of a point source in a multi-cylindrically layered medium," IEEE Trans. Geosci. Remote Sensing, vol. GRS-25, pp. 850-858, Nov. 1987.

[30] J. R. Wait, *Electromagnetic Propagation from Cylindrical Structures*, New York: Pergamon, 1959.

[31] L. B. Felsen and N. Marcuwitz, *Radiation and Scattering of Waves*. Englewood Cliffs, NJ: Prentice-Hall, 1973.

[32] L. B. Felsen and K. Naishadham, "Ray formulation of waves guided by circular cylindrically stratified dielectrics," Radio Sci., vol. 26, pp. 203-209, 1991.

[33] K. Naishadham and L. B. Felsen, "Dispersion of waves guided along a cylindrical substrate-superstrate layered medium," IEEE Trans. Antennas Propagat., vol. 41, pp. 304-313, Mar. 1993.

[34] L. W. Pearson, "A construction of the fields radiated by z-directed point sources of current in the presence of a cylindrically layered obstacle," Radio Sci., vol. 21, pp. 559-569, 1986.

[35] J. A. Kong, *Electromagnetic Wave Theory*, New York: Wiley, 1990.

[36] Y. Hua and T. K. Sarkar, " Generalized pencil-of-function method for extracting poles of an EM system from its transient response," IEEE Trans. Antennas Propagat., vol. 37, pp. 229-234, Feb. 1989.

[37] W. C. Chew, "The singularities of a Fourier-type integral in a multicylindrical layer problem," IEEE Trans. Antennas Propagat., Vol. 31, pp. 653-655, July. 1983.

[38] A. K. Bhattacharyya, "Characterisitics of Space and surface waves in a multilayered structure", IEEE Transactions on Antennas and Prop., Vol.38 No.8 August 1990.

[39] N. V. Shuley, R. R. Boix, F. Medina and M. Horno, "On the fast approximation of Green's functions in MPIE formulations for planarly layered media," IEEE Trans. Microw. Theory Tech., vol. 50, no. 9, pp. 2185-2192, Sep. 2002.

[40] I. Aksun and G. Dural, "Clarification of the Issues on the Closed-Form Green's Functions in Stratified Media", IEEE Transactions on Antennas and Prop., Vol.53 No.11 November 2005.

[41] A.Y. Svezhentsev and G.A.E. Vandenbosch, "Mixed-Potential Green's Functions for Sheet Electric Current Over Metal-Dielectric Cylindrical Structure", J. of Electromagn. Waves and Appl., Vol. 16, No. 6, 813-835, 2002.

[42] A.Y. Svezhentsev, "Space and Leaky Wave Contributions to Green's Function of a Dielectric-Coated Circular Cylinder", pp. 772-774, URSI EMTS, 2004.

[43] Ruel V. Churchill, James W. Brown, Roger F.Verhey, *Complex Variables and Applications*, Mc Graw-Hill, Third Edition, 1974.

[44] D.M. Pozar, "Input impedance and mutual coupling of rectangular microstrip antennas," IEEE Trans. Antennas Propagat., vol. AP-30, pp.1191-1196, Nov.1982.

[45] R.G. Rojas and C. Demirdağ, "Mutual coupling calculations on a dielectric coated PEC cylinder using a UTD-based Green's Function" IEEE Trans. On Antennas and Propagation, pp. 1525-1528, 1997.

[46] V.B. Ertürk, R.G.Rojas, "Efficient Analysis of Input Impedance and Mutual Coupling of Microstrip Antennas Mounted on Large Coated Cylinders", IEEE Trans. On Antennas and Propagation, Vol.51, No.4, April 2003.

[47] Silvia Raffaelli, "Analysis of Conformal Antennas and Periodic Structures", Technical Report, Department of Electromagnetics Chalmers University of Technology S-412 96 Gothenburg, June 2001.

[48] Silvia Raffaelli, Zvonimir Sipus, Per-Simon Kildal, "Analysis and Measurements of Conformal Patch Array Antennas on Multilayer Circular Cylinder", IEEE Trans. Antennas Propagat., vol. 53, No. 3, pp.1105-1113, March 2005.

[49] C.-Y. Huang and Y.-T. Chang,"Curvature effects on the Mutual Coupling of Cylindrical-rectangular microstrip antennas," Electron. Lett.,vol.33, pp. 1108-1109, June 1997.

[50] M. Marin, P.H. Pathak, "Calculation of the Surface Fields Created by a Current Distribution on a Coated Circular Cylinder", Technical Report 721565-1, April 1989, The Ohio State University Electroscience Laboratory.

[51] M.L. Van Blaricum and R. Mittra, "A technique for extracting the poles and residues of a system directly from its transient response", IEEE Transactions on Antennas and Prop., Vol. AP-23, pp. 777-781, November 1975.

[52] M.L. Van Blaricum and R. Mittra, "Problem and solutions associated with prony's method for processing transient data", IEEE Transactions on Antennas and Prop., Vol. AP-26, pp. 174-182, January 1978.

[53] V.K. Jain T.K. Sarkar and D.D. Veiner, "Rational modeling pencil-of function method", IEEE Transactions on Accoust., Speech, Signal Processing, Vol. ASSP-31, pp. 564-573, June 1983.

[54] Acar, R.C. and G. Dural, "Comments on 'A Complete Set of Spatial Domain Dyadic Green's Function Components for Cylindrically Stratified Media in Fast Computational Form'," J. of Electromagn. Waves and Appl., Vol. 18, No. 10, 1389-1394, 2004.

APPENDIX A

GENERALIZED PENCIL OF FUNCTION METHOD

The generalized pencil of function method (GPOF) [36] is used to approximate the spectral domain Green's functions with complex exponentials. Since this method is an important step in approximating the spectral domain Green's functions, it is given in this appendix.

The Prony Method and its variants can be used to extract the poles [51],[52] of a EM system. The pencil of function (POF) method [53] is an alternative method to the Prony method to find the system poles. In POF, the poles are found from the solution of a generalized eigenvalue problem, whereas the Prony method contains two step process where the first step involves the solution of a matrix equation and the second step involves finding roots of a polynomial. The generalized pencil of function method is a generalization to the POF method and it is used to estimate the poles of EM system from its transient response [36]. The GPOF method is more robust and less noise sensitive compared to the Prony method.

An EM transient signal with the samples y_k can be approximated as

$$y_k = \sum_{i=1}^{M} b_i e^{s_i \delta t k} = \sum_{i=1}^{M} b_i z_i^k \qquad k = 0,1,....., N-1 \qquad \text{(A.1)}$$

where b_i are the complex residues, s_i are the complex poles and δt is the sampling interval. The method can be given as follows

1. The following matrices are constructed,

$$\bar{Y}_1 = [\bar{y}_0, \bar{y}_1, ... \bar{y}_{L-1}] \qquad \text{(A.2)}$$

$$\bar{Y}_2 = [\bar{y}_1, \bar{y}_2, ... \bar{y}_L] \qquad \text{(A.3)}$$

where

$$\bar{y}_i = [\bar{y}_i, \bar{y}_{i+1}, ,.....\bar{y}_{i+N-L-1}]^T \quad \text{(A.4)}$$

L is the pencil parameter and its optimal choice is around L=N/2 [36].

2. Find a $\bar{Z}$ matrix as

$$\bar{V}\bar{D}^{-1}\bar{U}^H = SVD(\bar{Y}_1) \quad \text{(A.5)}$$

where $\bar{V}$, $\bar{D}^{-1}$ and $\bar{U}^H$ are (N-L)x(N-L), (N-L)xL and LxL matrices. $SVD(.)$ is the singular value decomposition process and the subscript H is the complex conjugate transpose of a matrix. The $\bar{Z}$ matrix is

$$\bar{Z} = \bar{D}^{-1}\bar{U}^H\bar{Y}_2\bar{V} \quad \text{(A.6)}$$

3. The poles of the system are obtained as

$$s_i = \frac{\log z_i}{\delta t} \quad i=1,2,.....M \quad \text{(A.7)}$$

where z_i's are the eigenvalues of the $\bar{Z}$ matrix.

4. The residues are found from the least-squares solution of the following system.

$$\begin{bmatrix} 1 & 1 & ... & 1 \\ z_1 & z_2 & \dots & z_M \\ . & . & ... & . \\ . & . & ... & . \\ . & . & ... & . \\ z_1^{N-1} & z_2^{N-1} & \dots & z_M^{N-1} \end{bmatrix} \begin{bmatrix} b_1 \\ b_2 \\ . \\ . \\ . \\ b_M \end{bmatrix} = \begin{bmatrix} y_0 \\ y_1 \\ . \\ . \\ . \\ y_{N-1} \end{bmatrix} \quad \text{(A.8)}$$

or

$$\bar{A}\bar{B} = \bar{Y} \quad \text{(A.9)}$$

so the b_i's are found by using the pseudo-inverse of the $\bar{A}$ matrix as $\bar{B} = \bar{A}^+\bar{Y}$.

APPENDIX B

SPECTRAL-DOMAIN GREEN'S FUNCTION COMPONENTS

For the sake of completeness, the complete-set of spectral-domain Green's functions are given as a reference. Among the spectral-domain Green's functions listed below, (B.1)-(B.4), (B.7)-(B.10), (B.19)-(B.22), (B.25)-(B.28) are given in [26]. The remaining spectral-domain Green's functions (B.11)-(B.18), (B.23), (B.24), (B.29)-(B.33), (B.36) are given in [54] as corrections.

***z*-oriented electric dipole :**

$$\tilde{\tilde{G}}_{zz}^{E_n} = \frac{k_{\rho_j}^2}{\varepsilon_j} f_{11} \tag{B.1}$$

$$\tilde{\tilde{G}}_{zz}^{H_n} = \frac{k_{\rho_j}^2}{\varepsilon_j} f_{21} \tag{B.2}$$

$$\tilde{\tilde{G}}_{\phi z}^{E_n} = \frac{k_{\rho_j}^2}{\varepsilon_j}\left(\frac{nk_z}{k_{\rho_i}^2\rho} f_{11} + \frac{j\omega\mu_i}{k_{\rho_i}^2}\frac{\partial f_{21}}{\partial\rho}\right) \tag{B.3}$$

$$\tilde{\tilde{G}}_{\phi z}^{H_n} = \frac{k_{\rho_j}^2}{\varepsilon_j}\left(-\frac{j\omega\varepsilon_i}{k_{\rho_i}^2}\frac{\partial f_{11}}{\partial\rho} + \frac{nk_z}{k_{\rho_i}^2\rho} f_{21}\right) \tag{B.4}$$

$$\tilde{\tilde{G}}_{\rho z}^{E_n} = \frac{k_{\rho_j}^2}{\varepsilon_j}\left(-\frac{jk_z}{k_{\rho_i}^2}\frac{\partial f_{11}}{\partial\rho} + \frac{\omega\mu_i n}{k_{\rho_i}^2\rho} f_{21}\right) \tag{B.5}$$

$$\tilde{\tilde{G}}_{\rho z}^{H_n} = \frac{k_{\rho_j}^2}{\varepsilon_j}\left(-\frac{\omega\varepsilon_i n}{k_{\rho_i}^2}\frac{f_{11}}{\rho} - j\frac{k_z}{k_{\rho_i}^2}\frac{\partial f_{21}}{\partial\rho}\right) \tag{B.6}$$

ϕ-oriented electric dipole :

$$\tilde{G}_{z\phi}^{E_n} = \frac{nk_z}{\varepsilon_j \rho'} f_{11} - j\omega \frac{\partial f_{12}}{\partial \rho'} \tag{B.7}$$

$$\tilde{G}_{z\phi}^{H_n} = \frac{nk_z}{\varepsilon_j \rho'} f_{21} - j\omega \frac{\partial f_{22}}{\partial \rho'} \tag{B.8}$$

$$\tilde{G}_{\phi\phi}^{E_n} = \frac{nk_z}{\varepsilon_j \rho'} \left(\frac{nk_z}{k_{\rho_i}^2 \rho} f_{11} + \frac{j\omega\mu_i}{k_{\rho_i}^2} \frac{\partial f_{21}}{\partial \rho} \right) - j\omega \frac{\partial}{\partial \rho'} \left(\frac{nk_z}{k_{\rho_i}^2 \rho} f_{12} + \frac{j\omega\mu_i}{k_{\rho_i}^2} \frac{\partial f_{22}}{\partial \rho} \right) \tag{B.9}$$

$$\tilde{G}_{\phi\phi}^{H_n} = \frac{nk_z}{\varepsilon_j \rho'} \left(-\frac{j\omega\varepsilon_i}{k_{\rho_i}^2} \frac{\partial f_{11}}{\partial \rho} + \frac{nk_z}{k_{\rho_i}^2 \rho} f_{21} \right) - j\omega \frac{\partial}{\partial \rho'} \left(-\frac{j\omega\varepsilon_i}{k_{\rho_i}^2} \frac{\partial f_{12}}{\partial \rho} + \frac{nk_z}{k_{\rho_i}^2 \rho} f_{22} \right) \tag{B.10}$$

$$\tilde{G}_{\rho\phi}^{E_n} = \frac{nk_z}{\varepsilon_j \rho'} \left(-\frac{jk_z}{k_{\rho_i}^2} \frac{\partial f_{11}}{\partial \rho} + \frac{\omega\mu_i n}{k_{\rho_i}^2 \rho} f_{21} \right) - j\omega \frac{\partial}{\partial \rho'} \left(-\frac{jk_z}{k_{\rho_i}^2} \frac{\partial f_{12}}{\partial \rho} + \frac{\omega\mu_i n}{k_{\rho_i}^2 \rho} f_{22} \right) \tag{B.11}$$

$$\tilde{G}_{\rho\phi}^{H_n} = \frac{nk_z}{\varepsilon_j \rho'} \left(-\frac{\omega\varepsilon_i n}{k_{\rho_i}^2 \rho} f_{11} - \frac{jk_z}{k_{\rho_i}^2} \frac{\partial f_{21}}{\partial \rho} \right) - j\omega \frac{\partial}{\partial \rho'} \left(-\frac{\omega\varepsilon_i n}{k_{\rho_i}^2 \rho} f_{12} - \frac{jk_z}{k_{\rho_i}^2} \frac{\partial f_{22}}{\partial \rho} \right) \tag{B.12}$$

ρ -oriented electric dipole :

$$\tilde{G}_{z\rho}^{E_n} = \left(\frac{jk_z}{\varepsilon_j} \frac{\partial f_{11}}{\partial \rho'} + \frac{n\omega}{\rho'} f_{12} \right) \tag{B.13}$$

$$\tilde{G}_{\phi\rho}^{E_n} = \frac{1}{k_{\rho_i}^2} \left(\frac{k_z n}{\rho} \left(\frac{jk_z}{\varepsilon_j} \frac{\partial f_{11}}{\partial \rho'} + \frac{n\omega}{\rho'} f_{12} \right) + j\omega\mu_i \frac{\partial}{\partial \rho} \left(\frac{jk_z}{\varepsilon_j} \frac{\partial f_{21}}{\partial \rho'} + \frac{n\omega}{\rho'} f_{22} \right) \right) \tag{B.14}$$

$$\tilde{G}_{\rho\rho}^{E_n} = \frac{1}{k_{\rho_i}^2} \left(-jk_z \frac{\partial}{\partial \rho} \left(\frac{jk_z}{\varepsilon_j} \frac{\partial f_{11}}{\partial \rho'} + \frac{n\omega}{\rho'} f_{12} \right) + \frac{\omega n\mu_i}{\rho} \left(\frac{jk_z}{\varepsilon_j} \frac{\partial f_{21}}{\partial \rho'} + \frac{n\omega}{\rho'} f_{22} \right) \right) \tag{B.15}$$

$$\tilde{G}_{z\rho}^{H_n} = \frac{jk_z}{\varepsilon_j} \frac{\partial f_{21}}{\partial \rho'} + \frac{n\omega}{\rho'} f_{22} \tag{B.16}$$

$$\tilde{G}_{\phi\rho}^{H_n} = \frac{1}{k_{\rho_i}^2} \left[-j\omega\varepsilon_i \frac{\partial}{\partial \rho} \left(\frac{jk_z}{\varepsilon_j} \frac{\partial f_{11}}{\partial \rho'} + \frac{n\omega}{\rho'} f_{12} \right) + \frac{k_z n}{\rho} \left(\frac{jk_z}{\varepsilon_j} \frac{\partial f_{21}}{\partial \rho'} + \frac{n\omega}{\rho'} f_{22} \right) \right] \tag{B.17}$$

$$\tilde{G}_{\rho\rho}^{H_n} = \frac{1}{k_{\rho_i}^2} \left(-\frac{n\omega\varepsilon_i}{\rho} \left(\frac{jk_z}{\varepsilon_j} \frac{\partial f_{11}}{\partial \rho'} + \frac{n\omega}{\rho'} f_{12} \right) - jk_z \frac{\partial}{\partial \rho} \left(\frac{jk_z}{\varepsilon_j} \frac{\partial f_{21}}{\partial \rho'} + \frac{n\omega}{\rho'} f_{22} \right) \right) \tag{B.18}$$

z-oriented magnetic dipole :

$$\tilde{\tilde{G}}_{zz}^{E_n} = \frac{k_{\rho_j}^2}{\mu_j} f_{12} \qquad (B.19)$$

$$\tilde{\tilde{G}}_{zz}^{H_n} = \frac{k_{\rho_j}^2}{\mu_j} f_{22} \qquad (B.20)$$

$$\tilde{\tilde{G}}_{\phi z}^{E_n} = \frac{k_{\rho_j}^2}{\mu_j}\left(\frac{nk_z}{k_{\rho_i}^2\rho} f_{12} + \frac{j\omega\mu_i}{k_{\rho_i}^2}\frac{\partial f_{22}}{\partial\rho}\right) \qquad (B.21)$$

$$\tilde{\tilde{G}}_{\phi z}^{H_n} = \frac{k_{\rho_j}^2}{\mu_j}\left(-\frac{j\omega\varepsilon_i}{k_{\rho_i}^2}\frac{\partial f_{12}}{\partial\rho} + \frac{nk_z}{k_{\rho_i}^2\rho} f_{22}\right) \qquad (B.22)$$

$$\tilde{\tilde{G}}_{\rho z}^{E_n} = \frac{k_{\rho_j}^2}{\mu_j}\left(-\frac{jk_z}{k_{\rho_i}^2}\frac{\partial f_{12}}{\partial\rho} + \frac{\omega\mu_i n}{\rho k_{\rho_i}^2} f_{22}\right) \qquad (B.23)$$

$$\tilde{\tilde{G}}_{\rho z}^{H_n} = \frac{k_{\rho_j}^2}{\mu_j}\left(\frac{-\omega\varepsilon_i n}{k_{\rho_i}^2\rho} f_{12} - \frac{jk_z}{k_{\rho_i}^2}\frac{\partial f_{22}}{\partial\rho}\right) \qquad (B.24)$$

ϕ-oriented magnetic dipole :

$$\tilde{G}_{z\phi}^{E_n} = j\omega\frac{\partial f_{11}}{\partial\rho'} + \frac{nk_z}{\mu_j\rho'} f_{12} \qquad (B.25)$$

$$\tilde{G}_{z\phi}^{H_n} = j\omega\frac{\partial f_{21}}{\partial\rho'} + \frac{nk_z}{\mu_j\rho'} f_{22} \qquad (B.26)$$

$$\tilde{G}_{\phi\phi}^{E_n} = j\omega\frac{\partial}{\partial\rho'}\left(\frac{nk_z}{k_{\rho_i}^2\rho} f_{11} + \frac{j\omega\mu_i}{k_{\rho_i}^2}\frac{\partial f_{21}}{\partial\rho}\right) + \frac{nk_z}{\mu_j\rho'}\left(\frac{nk_z}{k_{\rho_i}^2\rho} f_{12} + \frac{j\omega\mu_i}{k_{\rho_i}^2}\frac{\partial f_{22}}{\partial\rho}\right) \qquad (B.27)$$

$$\tilde{G}_{\phi\phi}^{H_n} = j\omega\frac{\partial}{\partial\rho'}\left(-\frac{j\omega\varepsilon_i}{k_{\rho_i}^2}\frac{\partial f_{11}}{\partial\rho} + \frac{nk_z}{k_{\rho_i}^2\rho} f_{21}\right) + \frac{nk_z}{\mu_j\rho'}\left(-\frac{j\omega\varepsilon_i}{k_{\rho_i}^2}\frac{\partial f_{12}}{\partial\rho} + \frac{nk_z}{k_{\rho_i}^2\rho} f_{22}\right) \qquad (B.28)$$

$$\tilde{G}_{\rho\phi}^{E_n} = j\omega\frac{\partial}{\partial\rho'}\left(-\frac{jk_z}{k_{\rho_i}^2}\frac{\partial f_{11}}{\partial\rho} + \frac{\omega\mu_i n}{k_{\rho_i}^2\rho} f_{21}\right) + \frac{nk_z}{\mu_j\rho'}\left(-\frac{jk_z}{k_{\rho_i}^2}\frac{\partial f_{12}}{\partial\rho} + \frac{\omega\mu_i n}{k_{\rho_i}^2\rho} f_{22}\right) \qquad (B.29)$$

$$\tilde{G}_{\rho\phi}^{H_n} = j\omega\frac{\partial}{\partial\rho'}\left(\frac{\omega\varepsilon_i n}{k_{\rho_i}^2\rho} f_{11} - \frac{jk_z}{k_{\rho_i}^2}\frac{\partial f_{21}}{\partial\rho}\right) + \frac{nk_z}{\mu_j\rho'}\left(-\frac{\omega\varepsilon_i n}{k_{\rho_i}^2\rho} f_{12} - \frac{jk_z}{k_{\rho_i}^2}\frac{\partial f_{22}}{\partial\rho}\right) \qquad (B.30)$$

ρ -oriented magnetic dipole :

$$\tilde{G}_{z\rho}^{E_n} = (-\frac{n\omega}{\rho'} f_{11} + \frac{jk_z}{\mu_j}\frac{\partial f_{12}}{\partial \rho'}) \quad (B.31)$$

$$\tilde{G}_{\phi\rho}^{E_n} = \frac{1}{k_{\rho_i}^2}(\frac{k_z n}{\rho}(-\frac{n\omega}{\rho'} f_{11} + \frac{jk_z}{\mu_j}\frac{\partial f_{12}}{\partial \rho'}) + j\omega\mu_i \frac{\partial}{\partial \rho}(-\frac{n\omega}{\rho'} f_{21} + \frac{jk_z}{\mu_j}\frac{\partial f_{22}}{\partial \rho'})) \quad (B.32)$$

$$\tilde{G}_{\rho\rho}^{E_n} = \frac{1}{k_{\rho_i}^2}(-jk_z \frac{\partial}{\partial \rho}(-\frac{n\omega}{\rho'} f_{11} + \frac{jk_z}{\mu_j}\frac{\partial f_{12}}{\partial \rho'}) + \frac{\omega\mu_i n}{\rho}(-\frac{n\omega}{\rho'} f_{21} + \frac{jk_z}{\mu_j}\frac{\partial f_{22}}{\partial \rho'})) \quad (B.33)$$

$$\tilde{G}_{z\rho}^{H_n} = (-\frac{n\omega}{\rho'} f_{21} + \frac{jk_z}{\mu_j}\frac{\partial f_{22}}{\partial \rho'}) \quad (B.34)$$

$$\tilde{G}_{\phi\rho}^{H_n} = \frac{1}{k_{\rho_i}^2}(-j\omega\varepsilon_i \frac{\partial}{\partial \rho}(-\frac{n\omega}{\rho'} f_{11} + \frac{jk_z}{\mu_j}\frac{\partial f_{12}}{\partial \rho'}) + \frac{k_z n}{\rho}(-\frac{n\omega}{\rho'} f_{21} + \frac{jk_z}{\mu_j}\frac{\partial f_{22}}{\partial \rho'})) \quad (B.35)$$

$$\tilde{G}_{\rho\rho}^{H_n} = \frac{1}{k_{\rho_i}^2}(-\frac{n\omega\varepsilon_i}{\rho}(-\frac{n\omega}{\rho'} f_{11} + \frac{jk_z}{\mu_j}\frac{\partial f_{12}}{\partial \rho'}) - jk_z \frac{\partial}{\partial \rho}(-\frac{n\omega}{\rho'} f_{21} + \frac{jk_z}{\mu_j}\frac{\partial f_{22}}{\partial \rho'})) \quad (B.36)$$

APPENDIX C

CONVOLUTION OF TESTING AND BASIS FUNCTIONS

The basis and testing functions of each current element J_n and J_m are selected as rooftop functions

$$J_{zn}(z,l)=\begin{Bmatrix}\dfrac{1}{wh_z}\left[(1-n)h_z+z\right] & (n-1)h_z\le z\le nh_z & ,|l|\le\dfrac{w}{2}\\ \dfrac{1}{wh_z}\left[(1-n)h_z+z\right] & nh_z\le z\le (n+1)h_z & ,|l|\le\dfrac{w}{2}\end{Bmatrix}$$

where w is the width of each current element.

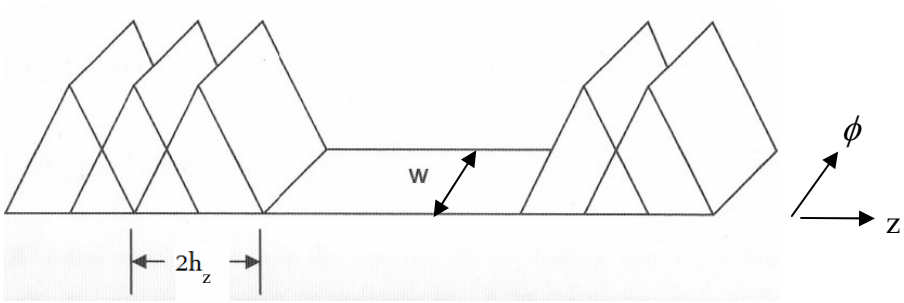

Figure C.1 Rooftop functions

- The convolution C_1 of the first testing function and the first basis function is calculated as

$$C_1=\bar{J}_{m1}*\bar{J}_{n1}$$

$T_{1L}=(m-1)h_z+u$	$B_{1L}=(n-1)h_z$
$T_{1C}=m\,h_z+u$	$B_{1C}=n\,h_z$
$T_{1U}=(m+1)h_z+u$	$B_{1U}=(n+1)h_z$

T_1L indicates the left part of the first testing function,

T_1R indicates the right part of the first testing function,

B_1L indicates the left part of the first basis function,

B_1R indicates the right part of the first basis function.

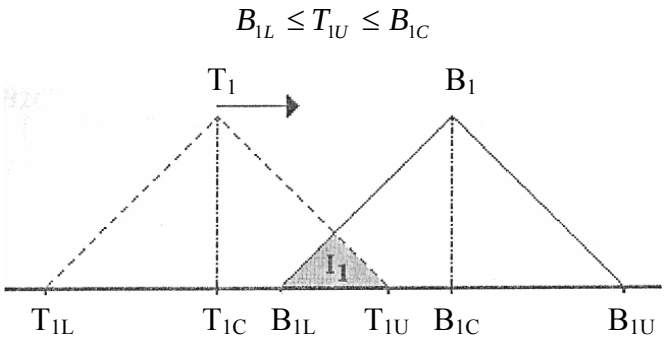

Figure C.2 Evaluation of C_{11}

$$C_{11} = I_1 = \int_{B_{1L}}^{T_{1U}} T_1R \,.\, B_1L \, dz \qquad \text{(C.1)}$$

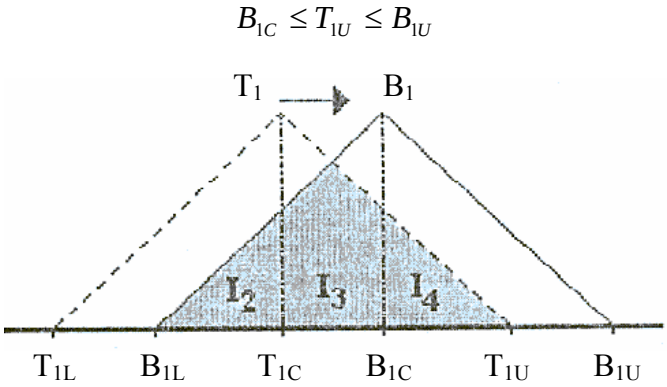

Figure C.3 Evaluation of C_{12}

$$C_{12} = I_2 + I_3 + I_4 = \int_{B_{1L}}^{T_{1C}} T_1L \,.\, B_1L \, dz + \int_{T_{1C}}^{B_{1C}} T_1R \,.\, B_1L \, dz + \int_{B_{1C}}^{T_{1U}} T_1R \,.\, B_1R \, dz \qquad \text{(C.2)}$$

$$T_{1U} > B_{1U} \quad \text{AND} \quad T_{1C} \le B_{1U}$$

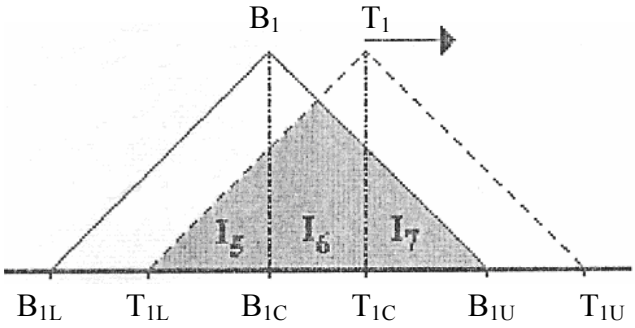

Figure C.4 Evaluation of C_{13}

$$C_{13} = I_5 + I_6 + I_7 = \int_{T_{1L}}^{B_{1C}} T_1L \,.\, B_1L \, dz + \int_{B_{1C}}^{T_{1C}} T_1L \,.\, B_1R \, dz + \int_{T_{1C}}^{B_{1U}} T_1R \,.\, B_1R \, dz \qquad \text{(C.3)}$$

$$T_{1C} > B_{1U}$$

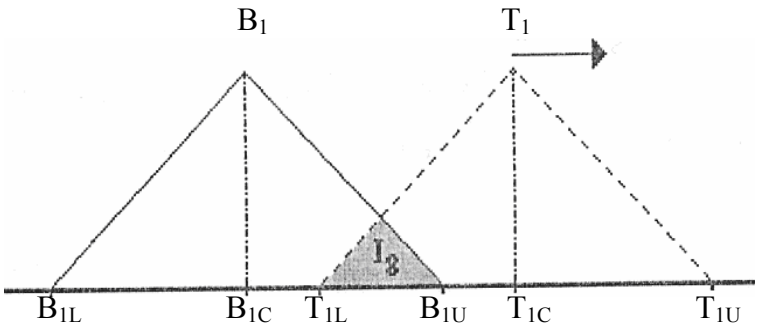

Figure C.5 Evaluation of C_{14}

$$C_{14} = I_8 = \int_{T_{1L}}^{B_{1U}} T_1L \,.\, B_1R \, dz \qquad \text{(C.4)}$$

The convolution $C_1 = \bar{J}_{m1} * \bar{J}_{n1}$ is the sum of the integrals evaluated in four regions, therefore

$$C_1 = C_{11} + C_{12} + C_{13} + C_{14}$$

The results of each type of integrals are given as follows

$$\int_{z_1}^{z_2} T_1R.B_1L\ dz=\frac{1}{(wh_z)^2}\left\{-\frac{z_2^3-z_1^3}{3}+\frac{z_2^2-z_1^2}{2}[u+(m+n)h_z]+(z_2-z_1)[u+(1+m)h_z][(1-n)h_z]\right\}$$

$$\int_{z_1}^{z_2} T_1L.B_1L\ dz=\frac{1}{(wh_z)^2}\left\{\frac{z_2^3-z_1^3}{3}+\frac{z_2^2-z_1^2}{2}[-u+(2-m-n)h_z]+(z_2-z_1)[-u+(1-m)h_z][(1-n)h_z]\right\}$$

$$\int_{z_1}^{z_2} T_1R.B_1R\ dz=\frac{1}{(wh_z)^2}\left\{\frac{z_2^3-z_1^3}{3}-\frac{z_2^2-z_1^2}{2}[u+(2+m+n)h_z]+(z_2-z_1)[u+(1+m)h_z][(1+n)h_z]\right\}$$

$$\int_{z_1}^{z_2} T_1L.B_1R\ dz=\frac{1}{(wh_z)^2}\left\{-\frac{z_2^3-z_1^3}{3}+\frac{z_2^2-z_1^2}{2}[u+(m+n)h_z]+(z_2-z_1)[-u+(1-m)h_z][(1+n)h_z]\right\}$$

(C.5)

- The convolution C_2 of the first testing function and the second basis function is calculated as C_1, therefore only the results are given.

$$C_2 = \bar{J}_{m1} * \bar{J}_{n2}$$

$T_{1L}=(m-1)h_z+u$	$B_{2L}=(n-1)\ h_z+\Delta z$
$T_{1C}=m\ h_z+u$	$B_{2C}=n\ h_z+\Delta z$
$T_{1U}=(m+1)\ h_z+u$	$B_{2U}=(n+1)\ h_z+\Delta z$

The convolution $C_2 = \bar{J}_{m1} * \bar{J}_{n2}$ is the sum of the integrals evaluated in four regions. The results of each type of integrals are given as follows,

$$\int_{z_1}^{z_2} T_1R.B_2L\ dz=\frac{1}{(wh_z)^2}$$
$$\left\{-\frac{z_2^3-z_1^3}{3}+\frac{z_2^2-z_1^2}{2}[u+\Delta z+(m+n)h_z]+(z_2-z_1)[u+(1+m)h_z][-\Delta z+(1-n)h_z]\right\}$$

$$\int_{z_1}^{z_2} T_1L \,.\, B_2L \; dz = \frac{1}{(wh_z)^2}$$
$$\left\{ \frac{z_2^3 - z_1^3}{3} + \frac{z_2^2 - z_1^2}{2}[-u - \Delta z + (2 - m - n)h_z] + (z_2 - z_1)[-u + (1 - m)h_z][-\Delta z + (1 - n)h_z] \right\}$$

$$\int_{z_1}^{z_2} T_1R \,.\, B_2R \; dz = \frac{1}{(wh_z)^2}$$
$$\left\{ \frac{z_2^3 - z_1^3}{3} - \frac{z_2^2 - z_1^2}{2}[u + \Delta z + (2 + m + n)h_z] + (z_2 - z_1)[u + (1 + m)h_z][\Delta z + (1 + n)h_z] \right\}$$

$$\int_{z_1}^{z_2} T_1L \,.\, B_2R \; dz = \frac{1}{(wh_z)^2}$$
$$\left\{ -\frac{z_2^3 - z_1^3}{3} + \frac{z_2^2 - z_1^2}{2}[u + \Delta z + (m + n)h_z] + (z_2 - z_1)[-u + (1 - m)h_z][\Delta z + (1 + n)h_z] \right\}$$

(C.6)

- The convolution C_3 of the second testing function and the first basis function is calculated as C_1, therefore only the results are given.

$$C_3 = \bar{J}_{m2} * \bar{J}_{n1}$$

$T_{2L}=(m-1)h_z+u+\Delta z$	$B_{1L}=(n-1)h_z$
$T_{2C}=m\,h_z+u+\Delta z$	$B_{1C}=n\,h_z$
$T_{2U}=(m+1)h_z+u+\Delta z$	$B_{1U}=(n+1)h_z$

The convolution $C_3 = \bar{J}_{m2} * \bar{J}_{n1}$ is the sum of the integrals evaluated in four regions. The results of each type of integrals are given as follows,

$$\int_{z_1}^{z_2} T_2 R \,.\, B_1 L \; dz = \frac{1}{(wh_z)^2}$$
$$\left\{ -\frac{z_2^3 - z_1^3}{3} + \frac{z_2^2 - z_1^2}{2}[u + \Delta z + (m+n)h_z] + (z_2 - z_1)[u + \Delta z + (1+m)h_z][(1-n)h_z] \right\}$$

$$\int_{z_1}^{z_2} T_2 L \,.\, B_1 L \; dz = \frac{1}{(wh_z)^2}$$
$$\left\{ \frac{z_2^3 - z_1^3}{3} + \frac{z_2^2 - z_1^2}{2}[-u + \Delta z + (2-m-n)h_z] + (z_2 - z_1)[-u - \Delta z + (1-m)h_z][(1-n)h_z] \right\}$$

$$\int_{z_1}^{z_2} T_2 R \,.\, B_1 R \, dz = \frac{1}{(wh_z)^2}$$
$$\left\{ \frac{z_2^3 - z_1^3}{3} - \frac{z_2^2 - z_1^2}{2}[u + \Delta z + (m+n+2)h_z] + (z_2 - z_1)[u + \Delta z + (1+m)h_z][(1+n)h_z] \right\}$$

$$\int_{z_1}^{z_2} T_2 L \,.\, B_1 R \, dz = \frac{1}{(wh_z)^2}$$
$$\left\{ -\frac{z_2^3 - z_1^3}{3} + \frac{z_2^2 - z_1^2}{2}[u + \Delta z + (m+n)h_z] + (z_2 - z_1)[-u - \Delta z + (1-m)h_z][(1+n)h_z] \right\}$$

(C.7)

- The convolution C_4 of the second testing function and the second basis function is calculated as C_1, therefore only the results are given.

$$C_4 = \bar{J}_{m2} * \bar{J}_{n2}$$

$T_{2L}=(m-1)h_z+u+\Delta z$	$B_{2L}=(n-1)h_z+\Delta z$
$T_{2C}=m\,h_z+u+\Delta z$	$B_{2C}=n\,h_z+\Delta z$
$T_{2U}=(m+1)h_z+u+\Delta z$	$B_{2U}=(n+1)h_z+\Delta z$

The convolution $C_4 = \bar{J}_{m2} * \bar{J}_{n2}$ is the sum of the integrals evaluated in four regions. The results of each type of integrals are given as follows,

$$\int_{z_1}^{z_2} T_2R.B_2L\ dz = \frac{1}{(wh_z)^2}$$
$$\left\{-\frac{z_2^3-z_1^3}{3}+\frac{z_2^2-z_1^2}{2}[u+2\Delta z+(m+n)h_z]+(z_2-z_1)[u+\Delta z+(1+m)h_z][-\Delta z+(1-n)h_z]\right\}$$

$$\int_{z_1}^{z_2} T_2L.B_2L\ dz = \frac{1}{(wh_z)^2}$$
$$\left\{\frac{z_2^3-z_1^3}{3}+\frac{z_2^2-z_1^2}{2}[-u-2\Delta z+(2-m-n)h_z]+(z_2-z_1)[-u-\Delta z+(1-m)h_z][-\Delta z+(1-n)h_z]\right\}$$

$$\int_{z_1}^{z_2} T_2R.B_2R\ dz = \frac{1}{(wh_z)^2}$$
$$\left\{\frac{z_2^3-z_1^3}{3}-\frac{z_2^2-z_1^2}{2}[u+2\Delta z+(m+n+2)h_z]+(z_2-z_1)[u+\Delta z+(1+m)h_z][\Delta z+(1+n)h_z]\right\}$$

$$\int_{z_1}^{z_2} T_2L.B_2R\ dz = \frac{1}{(wh_z)^2}$$
$$\left\{-\frac{z_2^3-z_1^3}{3}+\frac{z_2^2-z_1^2}{2}[u+2\Delta z+(m+n)h_z]+(z_2-z_1)[-u-\Delta z+(1-m)h_z][\Delta z+(1+n)h_z]\right\}$$

(C.8)

APPENDIX D

NEWTON-RAPHSON METHOD

Newton-Raphson method is based on the principle that if the initial guess of the root of $f(x)=0$ is at x_i, then if one draws the tangent to the curve at $f(x_i)$, the point x_{i+1} where the tangent crosses the x-axis is an improved estimate of the root (Figure D.1).

Using the definition of the slope of a function, at $x = x_i$

$$f'(x_i) = = \frac{f(x_i) - 0}{x_i - x_{i+1}} \tag{D.1}$$

which gives

$$x_{i+1} = x_i - \frac{f(x_i)}{f'(x_i)} \tag{D.2}$$

Equation (D.2) is called the Newton-Raphson formula for solving nonlinear equations of the form $f(x) = 0$. So starting with an initial guess, x_i, one can find the next guess, x_{i+1}, by using equation (D.2). One can repeat this process until one finds the root within a desirable tolerance. An algorithm can be given to find the root of an equation with Newton_Raphson method.

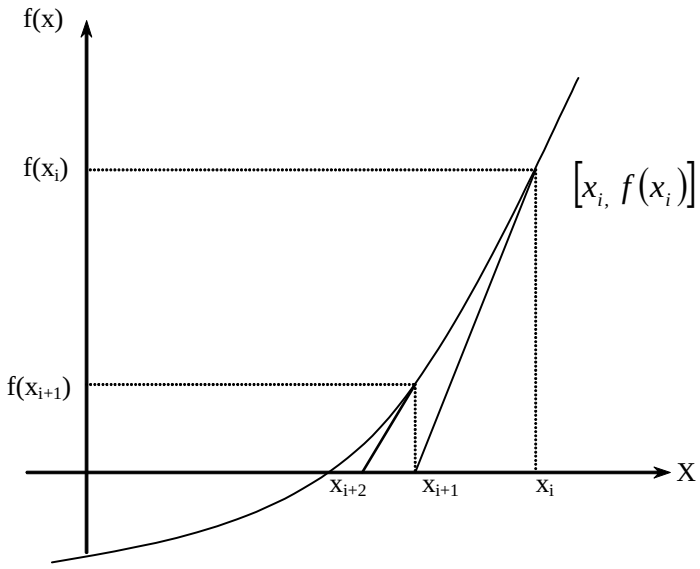

Figure D.1 Geometrical illustration of the Newton-Raphson method

Algorithm of Newton-Raphson method

The steps to apply Newton-Raphson method to find the root of an equation $f(x) = 0$ are :

1. Use an initial guess of the root, x_i, to estimate the new value of the root x_{i+1} as

$$x_{i+1} = x_i - \frac{f(x_i)}{f'(x_i)}$$

2. Find the absolute relative approximate error, $|\in_a|$ as

$$|\in_a| = \left|\frac{x_{i+1} - x_i}{x_{i+1}}\right| x\, 100$$

3. Compare the absolute relative approximate error, $|\in_a|$ with the pre-specified relative error tolerance, $\in_s$. If $|\in_a| > \in_s$, then go to step 1, else stop the algorithm. Also, check if the number of iterations has exceeded the maximum number of iterations.

CURRICULUM VITAE

PERSONAL INFORMATION

Surname, Name: Acar R. Cüneyt
Nationality: Turkish (TC)
Date and Place of Birth: 29 October 1974, Ankara
Marital Status: Single
Email: e110237@metu.edu.tr

EDUCATION

Degree	Institution	Year of Graduation
MS	METU Elec. and Electronics Eng.	1999
BS	HU Elec. and Electronics Eng.	1996
High School	Yükseliş College High School, Ankara	1992

WORK EXPERIENCE

Year	Place	Enrollment
1996-Present	Aselsan Electronics Inc.	Senior Expert RF Research Engineer
1994 August	Aselsan Electronics Inc.	Intern Engineering Student
1994 July	Aselsan Electronics Inc.	Intern Engineering Student

FOREIGN LANGUAGES

Advanced English, Fluent German, Beginner French

PUBLICATIONS

1. Acar, R.C. and G. Dural, "Comments on 'A Complete Set of Spatial Domain Dyadic Green's Function Components for Cylindrically Stratified Media in Fast Computational Form'," J. of Electromagn. Waves and Appl., Vol. 18, No. 10, 1389-1394, 2004.

2. Acar, R.C. and G. Dural, "Mutual Coupling of Printed Elements On A Cylindrically Layered Structure Using Closed-form Green's Functions" PIER, Vol. 78, 103-127, 2008.

3. Acar, R.C. and G. Dural, "Study of Surface Wave Contribution On A Cylindrically Layered Structure Using Closed-form Green's Functions" is under construction.